NOVEL NONLINEAR FREQUENCY CONVERSION SOURCES IN THE MID-INFRARED

JUNXIONG WEI

ICFO – INSTITUTE DE CIÈNCIES FOTÒNIQUES

UNIVERSITAT POLITÈCNICA DE CATALUNYA

BARCELONA, 2018

Novel nonlinear frequency conversion sources in the mid-infrared

Doctorate Program: **Photonics**

Duration: **2014-2018**

Thesis advisor

Prof. Majid Ebrahim-Zadeh

Thesis co-advisor

Dr. Chaitanya Kumar Suddapalli

Thesis submitted in partial fulfillment of the requirements for the degree of Doctor of Philosophy of the Universitat Politecnica de Catalunya

September 2018

To my family

Declaration

I hereby declare that the matter embodied and presented in the thesis entitled, “**Novel nonlinear frequency conversion sources in the mid-infrared**” is the result of investigations carried out by me at the ICFO-Institute of Photonic Sciences, Castelldefels, Barcelona, Spain under the supervision of Prof. Majid Ebrahim-Zadeh, and that it has not been submitted elsewhere for the award of any degree or diploma. In keeping with the general practice in reporting scientific observations, due acknowledgment has been made whenever the work described is based on the findings of other investigators.

Junxiong Wei

Certificate

I hereby certify that the matter embodied and presented in this thesis entitled, "**Novel nonlinear frequency conversion sources in the mid-infrared**" has been carried out by Mr Junxiong Wei at the ICFO-Institute of Photonic Sciences, Castelldefels, Barcelona, Spain, under my supervision, and that it has not been submitted elsewhere for the award of any degree or diploma.

Prof. Majid Ebrahim-Zadeh
(ICFO, Research Supervisor)

Acknowledgements

The work in this dissertation would not have been possible without the support of many people.

First and foremost, I would like to express my sincere gratitude to my research advisor, Professor Majid Ebrahim-Zadeh, for giving me the opportunity of being part of this wonderful institute and wonderful group, allows me to make my PhD a great personal experience. He was always there when a problem in the lab needed to be discussed and was a never-ending source of knowledge and ideas. It is primarily due to the breadth and depth of Majid scientific understanding, and his incredible ability to convey that understanding to others, that I have been able to find success in research. Majid has given me the freedom to pursue many projects, and it is with the help of his guidance, ideas, and insightful appraisal of any new results that I have been able to converge on sensible solutions to experimental problems. I am indebted to him more than he knows.

I am also extremely grateful for Dr. Chaitanya Kumar Suddapalli, my co-advisor, for rendering his continuous support in the lab and always providing me a helping hand. The discussions and collaborations with Chaitanya have been fruitful during the last years.

I would also like acknowledge to all of the other members of the Optical Parametric Oscillators group, Josep, Callum, Hanyu, Shahrzad, Anuja, and Kavita, for creating such a friendly and effective environment for research. The various discussions among the group have been very helpful and inculcated in me intellectual skills such as critical thinking, consistency, research design and problem solving.

I want to express my gratitude to Prof. Luis Torner, Director of the ICFO Institute of Photonic Sciences, and his management team for making ICFO such a marvelous place not only for research but also a place with the opportunity to meet many talented people from different countries and continents. Thanks to all of my friends at ICFO who made my times in and outside ICFO memorable. I would also like to thank the different units at ICFO such as administration, KTT, mechanical, electronic, IT and logistics for their help and organized coordination.

Last but not least, my everlasting gratitude goes to my family, especially to my parents, for their unconditional love, persistent support, affection and the importance of educational diligence at an early age. They are a constant source of inspiration and motivation for me. In addition, I wish to thank my wife, Jing Fu, who has enriched my life in every aspect in the last two years. I thank her for all the love, endless support and encouragement. It is to them, I wish to dedicate this thesis.

Abstract

The goal of this thesis has been the development of a new class of advanced solid-state photonic sources for the mid-infrared (mid-IR) spectral regions, where there exists a severe shortage of practical coherent laser sources, and many scientific and technological applications can benefit. The strategy has been to exploit nonlinear optical techniques based on difference frequency generation (DFG), parametric generation and oscillation, in the latest class of mid-IR nonlinear materials, in combination with the most advanced lasers pump sources based on fiber laser technology, to realize novel, high-power coherent source with broad tunability in the mid-IR. This thesis presents optical parametric oscillation (OPO) devices in novel designs, based on quasi-phase-matching (QPM) and using new concepts to facilitate the wavelength accessibility from 1 μm in the near-IR region to the mid-IR region.

Accordingly, we demonstrate an angle-tuned MgO:PPLN picosecond OPO, synchronously pumped by a Yb-fiber laser, for the first time to the best of our knowledge. The OPO is tunable from 1413-1900 nm in the signal togerther with idler tunability across 2418-4307 nm providing a total tunability of 2376 nm in the near-to-mid-IR region, simply by angular interrogation of the MgO:PPLN crystal at room temperature. Using a 10% output coupler, we were able to extract up to 2.4 W of signal at 1664 nm together with an idler power of 1.7 W at 2950 nm, corresponding to an overall extraction efficiency of ~45% with good beam pointing stability of better than 30 μrad and 14 μrad for the signal and idler, respectively. These results indicate the potential for rapid and wide tunability of high-power OPOs as compared to the temperature tuned devices.

In addition, we have demonstrated a novel device based on a tandem configuration, for an injection-seeded pulsed OPO system. Using a 38-mm-long PPLN crystal, we have produced ~0.94 W of average power with 9.7% slope efficiency at 1677 nm, for a pump power of 10 W at 80 kHz repetition rate. The measured optical bandwidth of signal is less than 20 MHz, and the seeding operation is achieved over signal wavelengths ranging from 1510 to 1677 nm, providing a total seeding range of 167 nm in the near-IR region. From a more general viewpoint, the method shown

here will also work at other wavelength range of OPO as well, opening a new path towards injection-seeding or injection-locking of pulse OPOs with full tuning range and high spectral purity.

Finally, we present detailed characterization of optical properties of the recently developed nonlinear material, orientation-patterned gallium phosphide (OP-GaP), by performing DFG experiments in the 2492-2782 nm wavelength range in the mid-IR. Detrimental issues such as thermal effects and residual absorption have been studied and confirmed by performing relevant measurements. Temperature and spectral acceptance bandwidths for DFG in the 40-mm-long OP-GaP crystal have been measured to be 18 ºC and 4 nm, respectively, at 1766 nm. Further, we have measured the damage threshold of the OP-GaP crystal to be 0.8 J/cm^2 at 1064 nm, for the first time. The polarization dependence of the input beams on the DFG power has also been systematically investigated. To our knowledge, this is the first report on tunable DFG in OP-GaP, as well as the first nanosecond DFG source based on this new nonlinear material.

Resumen

El objetivo de esta tesis era el desarrollo de una nueva clase de fuentes fotónicas de estado sólido para las regiones espectrales del infrarrojo medio (mid-IR), donde existe una gran escasez de fuentes láser coherentes, que pueden ser utilizadas para muchas aplicaciones científicas y tecnológicas. La estrategia consistió en explotar técnicas de óptica no lineal basadas en la generación de frecuencias diferencia (DFG), la generación paramétrica y la oscilación óptica paramétrica, usando la nuevos materiales no lineales para el mid-IR, en combinación con las fuentes de bombeo láser más avanzadas basadas en la tecnología láser de fibra, para realizar nuevas fuentes coherentes de alta potencia y amplia sintonía en el mid-IR. Esta tesis presenta dispositivos de oscilación óptica paramétrica (OPO) usando novedosos diseños, basados en materiales de quasi-phase-matching (QPM) y utilizando nuevos conceptos para facilitar la accesibilidad a la longitud de onda desde 1 µm en la región cercana al infrarrojo cercano hasta la región del mid-IR.

En consecuencia, demostramos un OPO de picosegundo con sintonización por ángulo del cristal MgO:PPLN, bombeando sincrónicamente por un láser de fibra de Yb, por primera vez según nuestro conocimiento. El OPO es sintonizable de 1413-1900 nm en el signal juntamente con la sintonización del idler a través de 2418-4307 nm que proporciona una sintonización total de 2376 nm en la región del infrarojo-cercano y mid-IR, simplemente por la interrogación angular del cristal de MgO:PPLN en temperatura ambiente. Utilizando un acoplador de salida del 10%, pudimos extraer hasta 2,4 W de señal a 1664 nm junto con una potencia de idler de 1,7 W a 2950 nm, lo que corresponde a una eficiencia total de extracción de ~45% con una buena estabilidad de apuntamiento del haz mejor que 30 µrad y 14 µrad para el signal y el idler, respectivamente. Estos resultados indican el potencial para una rápida y amplia sintonización de OPOs de alta potencia en comparación con los dispositivos sintonizados por temperatura.

Además, demostramos un novedoso dispositivo basado en una configuración en tándem, para un sistema OPO pulsado con un sistema "injection-seeded". Utilizando un cristal PPLN de 38 mm de longitud, hemos producido ~0,94 W de potencia media con una eficiencia de pendiente del 9,7%

a 1677 nm, para una potencia de bombeo de 10 W a una tasa de repetición de 80 kHz. La anchura de banda óptica de la señal medida es inferior a 20 MHz, y la operación de "seeding" se realiza en longitudes de onda de la señal que oscilan entre 1510 y 1677 nm, lo que proporciona una gama total de "seeding" de 167 nm en la región cercana al infrarrojo-cercano. Desde un punto de vista más general, el método mostrado aquí también funcionará en otros rangos de longitud de onda de OPO, abriendo un nuevo camino hacia el "seeding" por inyección o el bloqueo por inyección de OPOs de pulso con rango de sintonía completo y alta pureza espectral.

Por último, presentamos una caracterización detallada de las propiedades ópticas del material no lineal recientemente desarrollado, el orientation-patterned gallium phosphide (OP-GaP), mediante la realización de experimentos de DFG en el rango de longitud de onda de 2492-2782 nm en el rango de infrarrojos medio. Se han estudiado y confirmado cuestiones perjudiciales como los efectos térmicos y la absorción residual mediante la realización de las mediciones pertinentes. La temperatura y las anchuras de banda de aceptación espectral para DFG en el cristal OP-GaP de 40 mm de longitud han sido medidas obteniendo 18 ºC y 4 nm, respectivamente, a 1766 nm. Además, por primera vez hemos medido el umbral de daño del cristal OP-GaP siendo de 0,8 J/cm2 a 1064 nm. También se ha investigado sistemáticamente la dependencia de la polarización de los haces de entrada con respecto a la potencia de la DFG. Hasta donde sabemos, este es el primer informe sobre DFG sintonizable en OP-GaP, así como la primera fuente de nanosegundos DFG basada en este nuevo material no lineal.

Journal publications

1. **Junxiong Wei**, S. Chaitanya Kumar, and M. Ebrahim-Zadeh, *" Broadly tunable, intracavity seeded pulsed optical parametric oscillator,"* Opt. Lett , to be submit (2018)
2. **Junxiong Wei**, S. Chaitanya Kumar, Hanyu Ye, P. G. Schunemann, and M. Ebrahim-Zadeh, *"Performance characterization of mid-infrared difference-frequency-generation in orientation-patterned gallium phosphide,"* Opt. Mater. Express 8, 555-567 (2018) (Highlighted as an Editor's Pick)
3. **Junxiong Wei**, S. Chaitanya Kumar, Hanyu Ye, Kavita Devi, Peter G. Schunemann, and M. Ebrahim-Zadeh, *"Nanosecond difference-frequency generation in orientation-patterned gallium phosphide,"* Opt. Lett. 42, 2193-2196 (2017)
4. Hanyu Ye, S. Chaitanya Kumar, **Junxiong Wei**, P. G. Schunemann, and M. Ebrahim-Zadeh, *"Optical parametric generation in orientation-patterned gallium phosphide,"* Opt. Lett. 42, 3694-3697 (2017)
5. Hanyu Ye, S. Chaitanya Kumar, **Junxiong Wei**, P. G. Schunemann, and M. Ebrahim-Zadeh, "*Singly-resonant pulsed optical parametric oscillator based on orientation-patterned gallium phosphide*," Opt. Lett. 43, 2454-2457 (2018)
6. S. Chaitanya Kumar, **Junxiong Wei**, J. Debray, V. Kemlin, B. Boulanger, H. Ishizuki, T. Taira, and M. Ebrahim-Zadeh, *"High-power, widely tunable, room-temperature picosecond optical parametric oscillator based on cylindrical 5%MgO:PPLN,"* Opt. Lett. 40, 3897-3900 (2015)
7. S. Chaitanya Kumar, J. Canals Casals, **Junxiong Wei**, and M. Ebrahim-Zadeh, "*High-power, high-repetition-rate performance characteristics of β-BaB_2O_4 for single-pass picosecond ultraviolet generation at 266 nm*," Opt. Express 23, 28091-28103 (2015)

Proceeding publications

Junxiong Wei, S. Chaitanya Kumar, Hanyu Ye, P. G. Schunemann, M. Ebrahim-Zadeh, "Performance characterization of mid-infrared difference frequency generation in orientation-patterned gallium phosphide," Proc. SPIE 105160V, San Francisco, California, United States (2018)

Conference publications

1. **J. Wei**, S. Chaitanya Kumar, H. Ye, P. G. Schunemann, M. Ebrahim-Zadeh, Performance characterization of mid-infrared difference frequency generation in orientation-patterned gallium phosphide, Photonics West, San Francisco, California, United States, January 2018 (Paper:10516-30)
2. **J. Wei**, S. Chaitanya Kumar, H. Ye, K. Devi, P. G. Schunemann, M. Ebrahim-Zadeh, Mid-infrared difference-frequency-generation in orientation-patterned gallium phosphide, The 24th Congress of the International Commission for Optics, Tokyo, Japan, August 2017 (Paper: Tu1D-05)
3. H. Ye, S. Chaitanya Kumar, **J. Wei**, P. G. Schunemann, M. Ebrahim-Zadeh, Optical parametric generator based on orientation-patterned gallium phosphide,CLEO/Europe-EQEC, Munich, Germany, June 2017 (Paper: CD-10.3)
4. S. Chaitanya Kumar, **J. Wei**, A. J. Debray, V. Kemlin, B. Boulanger, H. Ishizuki, T. Taira, M. Ebrahim-Zadeh, Picosecond mid-infrared optical parametric oscillator based on cylindrical MgO: PPLN, CLEO, San Jose, USA, June 2016 (Paper: STh1P.2)
5. S. Chaitanya Kumar, J. C. Casals, **J. Wei**, K. Devi, M. Ebrahim-Zadeh, 2.9 W picosecond ultraviolet source at 266 nm based on walk-off compensated single-pass fourth harmonic generation in β-BaB_2O_4, CLEO, San Jose, USA, June 2016 (Paper: SW4Q.2)

6. S. Chaitanya Kumar, **J. Wei**, A. Jérôme Debray, V. Kemlin, B. Boulanger, H. Ishizuki, T. Taira, M. Ebrahim-Zadeh, Angle-tuned quasi-phase-matched mid-infrared optical parametric oscillator, Mid-Infrared Coherent Sources (MICS) 2016, Long Beach, California, USA (Paper: MS3C.4)
7. S. Chaitanya Kumar, **J. Wei**, A. J. Debray, V. Kemlin, B. Boulanger, H. Ishizuki, T. Taira, M. Ebrahim-Zadeh, High-power, Widely tunable, room-temperture, picosecond optical parametric oscillator based on cylindrical MgO:PPLN, Advanced Solid State Lasers 2015, Berlin Germany (Paper: AM3A.8)

Contents

List of Tables

List of Figures

List of Abbreviations and Symbols

The following abbreviations and symbols are used throughout the thesis.

mid-IR	Mid-infrared (2-12 μm wavelength)
UV	Ultraviolet
BBO	Beta barium borate (β-BaB_2O_4)
LBO	Lithium triborate (LiB_3O_5)
PPKTP	Periodically poled potassium titanyl phosphate
PPLN	Periodically poled lithium niobate
PPLT	Periodic poled lithium tantalate
ZGP	Zinc germanium phosphide ($ZnGeP_2$)
OP-GaAs	Orientation patterned gallium arsenide
CSP	Cadmium silicon phosphide ($CdSiP_2$)
OP-GaP	Orientation patterned gallium phosphide
QCL	Quantum cascade lasers
CW	Continuous Wave
SHG	Second harmonic generation
SFG	Sum frequency generation
DFG	Difference frequency generation
OPA	Optical parametric amplification
OPG	Optical parametric generation
OPO	Optical parametric oscillation/-er

QPM	Quasi-phase-matching
BPM	Birefringent phase-matching
$\chi^{(m)}$	mth order susceptibility response tensor
P	Material polarization
E	Electric field
c	Speed of light in vacuum
ω	Angular frequency
FWHM	Full width at half maximum
n	Refractive index
t	Time
$r = \boldsymbol{x}\overrightarrow{\boldsymbol{e_x}} + \boldsymbol{y}\overrightarrow{\boldsymbol{e_y}} + \boldsymbol{z}\overrightarrow{\boldsymbol{e_z}}$	Spatial coordinate
Λ	Grating period
d_{eff}	Effective nonlinear coefficient
k_i	Wave vector
Δk	Wave vector mismatch
Γ	Gain factor
δ	Degeneracy factor
L	Interaction length
n_e	Extraordinary refractive index
n_o	Ordinary refractive index
L_{eff}	Effective crystal length
CPM	Critical phase-matching
NCPM	Noncritical phase-matching
FOM	Figure-of-merit

Chapter 1

Introduction

1.1 Overview and motivations

Coherent mid-infrared (mid-IR) laser sources have come of age and are increasingly being used in spectroscopy [1-3], trace gas monitoring [4], remote sensing [5], frequency metrology [6], telecommunications [7], ophthalmology, and skin disease diagnosis [8,9]. Remarkable progress has been achieved in the last decade in the development of nonlinear frequency conversion technology, specifically in the mid-IR spectral region between 2-10 µm. The driving force for this progress has been the rapidly developing application fields in environmental, biological, engineering, and chemical sciences. From the fundamental point of view, as many gas molecules have their strongest absorption features in the mid-IR region, thus the detection sensitivity can be optimized in spectroscopy [10].

After half-a-century since the invention of laser, due to the unavailability of suitable gain media, vast spectral regions in the mid-IR still remain inaccessible to conventional lasers, in practically all time scales, from *continuous-wave* (CW) to femtosecond regime. Figure 1(a) shows examples of some of the available tunable lasers. Among of all Ti:sapphire laser is the most prominent and widely used tunable laser. It has a broad gain bandwidth, which is also advantageous for ultrashort pulse generation. The maximum tunability of the Ti:sapphire laser is, however, limited to at best 300-400 nm. On the other hand, nonlinear optics, and in particular nonlinear frequency conversion based on second-order nonlinear processes (three-wave interactions) in non-centrosymmetric bulk crystals, has provided an important alterative, leading to the development of tunable coherent light sources. In particular, parametric sources have enabled access to spectral regions that are unavailable to conventional lasers across the optical spectrum extending from the ultraviolet (UV) to the mid-IR [12], as depicted in Fig.1(b).

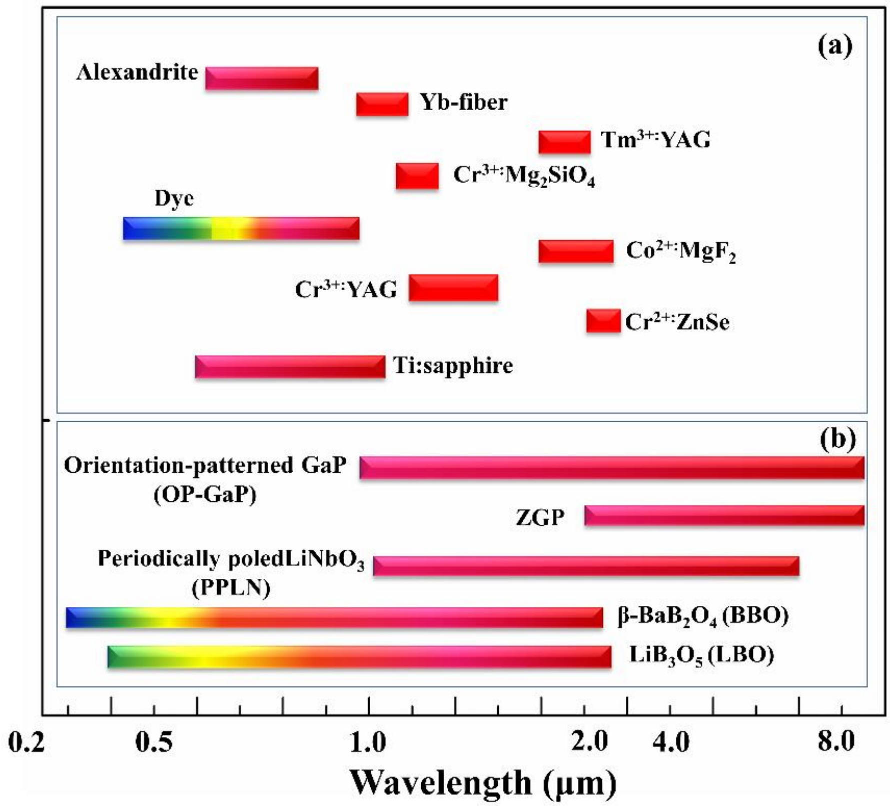

Figure 1: Comparison of the spectral coverage of (a) prominent conventional tunable lasers and (b) a number of optical parametric devices developed to date [11].

Further, they offer practical output powers with high efficiency and can be operated in all temporal regimes, from CW and pulsed nanosecond to ultrafast picosecond and femtosecond time-scales. Such devices are of great interest for variety of application in spectroscopy [2], remote sensing [6] and environmental monitoring [7].

In general, nonlinear frequency conversion processes can be configured with two pump lasers in single-pass arrangement, such as *difference-frequency-generation* (DFG), or configured with a single pump laser in a cavity, such as an *optical parametric oscillator* (OPO). In the case of DFG, the narrow emission spectra of the pump and signal are convolved during the frequency conversion process, and hence translate into a similarly narrow spectrum of the output idler wave. Many DFG-based mid-IR sources are now routinely deployed in a variety of applications including spectroscopy, optical microscopy, environmental trace gas detection and monitoring [13]. However, CW DFG devices still have some practical problems in terms of providing high output power and efficiency. On the other hand, OPOs have the ability to cover broad spectral regions, offering a compact solid-state design, while providing practical output powers at high efficiencies, and in all time-scales from the CW to ultrafast sub-20 fs time-scales [14-15]. To date, generation of tunable laser radiation relies heavily on frequency conversion techniques in nonlinear crystals, and OPOs are the leading device candidate.

Since the operation of an OPO is critically dependent on the spectral and spatial quality of the pump laser and also on the properties of the nonlinear optical materials, development of the practical OPOs was for many years hampered by several obstacles, most notably a lack of suitable nonlinear materials. The first experimental device based on an OPO was reported by Giordmaine and Miller in 1965 [16]. After this demonstration, it initiated an intense surge of research interest in parametric devices and prompted an extensive studies for nonlinear materials and laser pump sources. For nearly two decades thereafter, progress was made in the development of the foundations for the field of parametric frequency conversion and established many of the fundamental principles and practical benchmarks for this area. However, there was little or no progress in the practical development of OPO devices, until to 1980s, the advent of new nonlinear materials, such as β-BaB_2O_4 (BBO) [17], LiB_3O_5 (LBO) [18], and $KTiOPO_4$ (KTP) [19], once again prompted a major resurgence of interest in parametric devices.

High-power all-solid-state sources especially operated in the CW regime with wide tunability are of great importance for many applications. Although, for this purpose, Ti:sapphire laser and the dye laser were the most widely established laser sources for many years, CW OPOs as potential alternatives can provide widely tunable CW radiation in a much simpler and cost-effective design. However, practical OPOs operating in the CW regime has been traditionally the most challenging class of devices, since the substantially lower nonlinear gains available under CW pumping necessitate the use of high-power CW pump laser or the deployment of multiple-resonant cavities to reach operation threshold. In 1993, Yang et al. developed [20] the first CW SRO by using birefringent KTP crystal. In the mid-1990s, with the emergence of ferroelectric *quasi-phase-matched* (QPM) nonlinear crystals, particularly periodically poled $LiNbO_3$ (PPLN) [21] and

$LiTaO_3$ (PPLT) [22], combined with the progress in solid-state and fiber pump lasers, stimulated new impetus for the advancement of CW OPO devices. In 1996, Bosenberg at al. [23] demonstrated the first CW OPO based on PPLN. Since then, the development of new QPM materials and improved pump laser sources had led to parametric devices from laboratory concepts to practical viable tunable sources for many applications. In the years to follow, tremendous progress was achieved in the development of OPOs based on new design concepts, phase-matching geometries and novel pumping schemes, which have led to the realization of practical devices with much improved performance characteristics. In the current state of technology, OPOs based on the continued advances in high-power fiber lasers and amplifiers have provided versatile class of CW laser sources for the mid-IR with the advantages of simplicity, compact design, portability, improved functionality, and high output power and efficiency.

To date, the vast majority of CW OPOs have been developed in *single-resonate oscillator* (SRO) scheme based on PPLN, providing spectral coverage from 1.3 μm up to the absorption edge of the material near ~ 4.5 μm [24, 25]. For wavelength generation beyond ~4.5 μm, the use of PPLN is generally precluded by the onset of multi-phonon absorption in the material. As such, the development of practical CW OPOs for deep-IR has remained difficult, particularly in high-power SRO configuration. Over the years, there have also been many attempts to generate tunable radiation in the 4-10 μm wavelength range by different techniques. Each system has its advantages, but also its drawbacks. CO_2 gas lasers, one of the earliest lasers to be developed, offer high output power and a large emission wavelength bands (9.2-10.8 μm) [26, 27]. However, the tunability is not continuous, since the emission spectrum coincides with the CO_2 emission lines. Based on inter-sub-band transitions in semiconductor heterostructures, quantum cascade lasers (QCL) can be tailored to emit over a wide range of mid-IR wavelengths [28, 29]. Typically, however, the tuning range of a single device is limited to a few cm^{-1}. In lead-salt diode lasers, depending on their composition, the wavelength range can be selected throughout the mid-IR region between 3 and 30 μm. However, mode-hop-free tuning is limited to1-2 cm^{-1}. In addition, these devices require cryogenic cooling for CW operation, and the output power is very low, typically around 0.1 mW. Because of these limitations, at present, the most promising approach to develop tunable mid-to-deep-IR light sources is using nonlinear frequency conversion techniques, such as DFG [30], OPO [31], or cascaded OPOs [32], primarily pumped by the well-established Nd:YAG or Yb-fiber lasers at 1064 nm. At the same time, suitable materials with the required linear and nonlinear optical properties, in addition to the long-wavelength transparency cut-off, are key factors for making practical and efficient frequency conversion devices. Several material parameters, including effective nonlinear coefficient (d_{eff}), type of interaction and the polarizations of the incident fields, as well as temperature and spectral phase-matching properties, are critical factors for efficient frequency conversion processes. At present, the most suitable candidate nonlinear materials that can be used for deep infrared generation are zinc germanium phosphide (ZGP, $ZnGeP_2$), orientation patterned gallium arsenide (OP-GaAs), cadmium silicon phosphide ($CdSiP_2$) and the new QPM semiconductor, orientation patterned gallium phosphide (OP-GaP). With the exploitation of fiber lasers technology and novel nonlinear materials, OPOs will continue to serve as versatile tunable sources for spectral regions from the near- and mid-IR to the THz, and delivering watt-level output powers at exceptional efficiencies with excellent output characteristics.

1.2 Motivations and methods

The work presented in this thesis deals with both CW and ultrafast picosecond OPO in SRO configuration and pulsed nanosecond DFG in single pass configuration. The picosecond OPO is based on MgO:PPLN and is pumped at 1 μm, generating high-power mid-IR radiation in the 1.4-4.3 μm spectral range. The pulsed nanosecond DFG source is also pumped at 1 μm and, combined with a near-IR signal 1.72-1.82 μm, generates nanosecond mid-IR pulses in the 2-3 μm wavelength range, using the new QPM nonlinear material, OP-GaP. Moreover, the devices presented here are based on fiber laser technology, making them compact, practical and robust. In addition, a novel design for efficient tunable injection-seeding based on a CW SRO is proposed as an alternative method for tunable seeding applications.

The thesis is organized into 7 chapters. Chapter 2 provides introduction to nonlinear optical phenomena including SHG, SFG, DFG and OPO, together with the necessary theoretical work frame. As the successful operation of an OPO device necessitates proper cavity design, in chapter 3, we discuss some of the important designed issues.

MgO:PPLN-based OPOs have now been established as important practical tunable coherent light sources to provide 2-4 μm laser radiation. In the effort of this direction, in chapter 4, we demonstrate a new concept of angle-tuned MgO:PPLN OPO, for the first time. The OPO is tunable across the near-IR signal wavelength range of 1413-1900 nm together with the mid-IR idler range of 2418-4307 nm by angle tuning the cylindrical MgO:PPLN crystal at room temperature. The OPO simultaneously provides as much as 2.4 W of signal at 1664 nm using a 10% output coupler and 1.7 W of idler power at an overall extraction efficiency of ~45% with good beam pointing stability.

OP-GaP, one of the most recent QPM optical semiconductor, offers promising linear and nonlinear properties for deep mid-IR generation. It overcomes several limitations of the established nonlinear materials such as $ZnGeP_2$, OP-GaAs, which require pumping laser at wavelengths longer than 2 μm [24]. OP-GaP exhibits higher thermal conductivity, noncritical phase-matching, high nonlinearity and a larger band gap, which enable deep mid-IR generation using established pump laser technology at ~1 μm. However, during this early stage in the development of this crystal, several growth parameters are yet to be established to achieve the expected performance out of this crystal. Hence, it is imperative to perform detailed characterization of the linear and nonlinear optical properties to investigate the viability of this material for nonlinear frequency conversion in different time-scales. In the chapter 5, we have studied the full performance characterization of a tunable single-pass nanosecond DFG source based on OP-GaP by mixing the output of a Q-switched Nd:YAG laser at 1.064 μm and the signal from a pulsed MgO:PPLN OPO pumped by the same laser . Using the longest OP-GaP crystal (40 mm) deployed to date, the DFG source provides up to ~14 mW of average output power at 2719 nm at 80 kHz repetition rate, with >6 mW across 2690-2793 nm, in TEM_{00} spatial profile. Detrimental issues such as thermal effects and residual absorption have been studied and confirmed by performing relevant measurements. Temperature and spectral acceptance bandwidths for DFG in the 40-mm-long OP-GaP crystal have been measured to be 18 ºC and 17 nm, respectively, at 1766 nm. Further, we have measured the damage threshold of the OP-GaP crystal to be 0.8 J/cm^2 at 1064 nm, for the first time. The polarization dependence of the input beams on the DFG power has also been systematically investigated. To our knowledge, this is the first report on tunable DFG in OP-GaP, as well as the first nanosecond DFG source based on this new nonlinear material.

In the chapter 6, we have demonstrated a compact, highly efficient seeded nanosecond OPO device with wide seeding range. Compared to the relatively complex conventional injection-seeding methods, with limited tunability, here we used a CW SRO as an intracavity seed laser for the nanosecond pulsed OPO. Using a 38-mm-long MgO:PPLN crystal, we have generated ~0.94 W of average power with 9.7% slope efficiency at 1677 nm with pulse duration of 29.4 ns for a pump power of 10 W at 80 kHz repetition rate, by parametrically seeding with a narrow linewidth CW OPO internal to the pulses OPO cavity. The bandwidth of generated pulsed signal is as narrow as 5.6-MHz, and the seeding operation is achieved from 1510 nm to 1677 nm by temperature tuning of the MgO:PPLN crystal. The output spectrum, beam quality, and the confirmation of seeded operation is also presented in this chapter. Finally, in chapter 7 the thesis is concluded with some of our ongoing efforts and future outlook in the field.

Chapter 2

Basic Principles of Frequency Conversion

This chapter provides an overview of the theory and essential dynamical equations of waves mixing of nonlinear optics relevant to this thesis. More detailed and comprehensive treatment of nonlinear three-wave processes and devices can be found in several other references [33-35].

2.1 Basics of nonlinear optics

Optics is the study of interaction of light and matter. Generally, light is expressed as an electromagnetic field with spatially and temporally varying electric and magnetic components, ***E*(*r*, t)** and ***B*(r, t)**, respectively. Such a light wave can interact with matter or, more precisely, with the charged particles inside of matter. In most situations of practical interest in nonlinear optics, the interaction between the magnetic field and matter is much weaker in comparison to the electrical field. Therefore, the magnetic field will be disregarded from now on. Instead, the description is limited to the interaction between the electrical field of a laser beam and a non-magnetic nonlinear medium with free charges and zero currents.

For a laser propagating along ***r***-axis, the electric field can be described by a complex amplitude, ***E***, and an exponential function:

$$\boldsymbol{E}(\boldsymbol{r},t)=\frac{1}{2}\,\{\boldsymbol{E_0}(\boldsymbol{r},\omega)\,exp[i(\omega t-\boldsymbol{kr})]\}+c.c \qquad (2.1-1)$$

Here, $\boldsymbol{E_0}$ **(*r*, ω)** is the space and frequency dependent amplitude, ***k*** is the wave vector, ω is the circular frequency of the rapidly oscillating wave, and c.c. denotes the complex conjugate.

When an electric field is applied to a dielectric medium, a separation of bound charges is induced, resulting in a collection of induced dipole moments. In order to describe the optical response, the polarization of the material in which the frequency conversion is to take place needs to be considered. Since the incident light will induce material polarization, this in turn results in a separation of charges, which gives rise to a dipole moment. The dipole moment per unit volume is called the polarization of the material. The induced polarization, $\boldsymbol{P}$, in its most general form, is given by a power series in the applied electric field as:

$$\boldsymbol{P} = \varepsilon_0\left(\chi^{(1)}\boldsymbol{E} + \chi^{(2)}\boldsymbol{E}^2 + \chi^{(3)}\boldsymbol{E}^3 + \cdots\cdots\right) = \boldsymbol{P}^L + \boldsymbol{P}^{NL} \qquad (2.1-2)$$

where $\boldsymbol{P}^L = \varepsilon_0\, \chi^{(1)}\boldsymbol{E}$ is the linear polarization, and $\boldsymbol{P}^{NL}$ is the nonlinear polarization induced by sufficiently intense light field. $\varepsilon_0 = 8.85\times10^{-12}$ F/m is the electric permittivity in free space. $\chi^{(m)}$ is the susceptibility response tensor of m^{th} order and becomes a scalar quantity in an isotropic medium.

2.2 Second-order nonlinearity

The second-order nonlinear polarizability, $\boldsymbol{P}^{(2)}$, is used to describe the so-called three-wave mixing processes. Mathematically, it can be represented as:

$$\boldsymbol{P}^{(2)} = \varepsilon_0\chi^{(2)}\!:\boldsymbol{EE} \qquad (2.2-1)$$

Where $\chi^{(2)}$ is the second-order nonlinear susceptibility of the material, which gives rise to familiar nonlinear optical processes such as *second-harmonic generation* (SHG), *sum frequency generation* (SFG), DFG, and most importantly in the context of this thesis, optical parametric generation (OPG) and amplification (OPA), and OPO.

If we assume an applied electric field, $\boldsymbol{E}$, consisting of two monochromatic harmonic waves, $\boldsymbol{E_1}$ and $\boldsymbol{E_2}$, with corresponding frequency components, ω_1 and ω_2, it can be presented in the form:

$$\boldsymbol{E(t)} = \boldsymbol{E_1(t)}\, e^{-i\omega_1 t} + \boldsymbol{E_2(t)} e^{-i\omega_2 t} + c.c \qquad (2.2-2)$$

According to equations (2.2-1) and (2.2-2), we find that the second-order nonlinear polarization created in such a medium is:

$$\boldsymbol{P^{(2)}} = \varepsilon_0 \chi^{(2)} [\boldsymbol{E_1^2} e^{-2i\omega_1 t} + \boldsymbol{E_2^2} e^{-2i\omega_2 t} \qquad (2.2-3)$$

$$+2\boldsymbol{E_1 E_2} e^{-i(\omega_1+\omega_2)t} + \boldsymbol{2E_1 E_2^*}\, e^{-i(\omega_1-\,\omega_2)t} + c.c] \qquad (2.2-4)$$

$$+2\varepsilon_0 \chi^{(2)} [\boldsymbol{E_1 E_1^*} + \boldsymbol{2E_2 E_2^*}] \qquad (2.2-5)$$

From which several familiar second-order processes are associated with the different combinations of ω_1 and ω_2. These include the first two terms of (2.2-3), which represent SHG, the first two terms of (2.2-4) represents the physical processes called SFG, and DFG, the last term (2.2-5) represents *optical rectification* (OR). Here, we do not consider the complex conjugates (c.c.) of the above equation, as they do not lead to any extra processes other than the above mentioned processes.

The physical meaning of the different types of frequency conversion processes are illustrated in Fig. 2.1. In all of the optical processes, energy and momentum of the photons taking part in the frequency conversion have to be conserved. The momentum conservation is also known as the phase-matching condition. In the SFG processes, depicted in Fig. 2.1(b), two input photons (ω_1 and ω_2) traveling through the nonlinear medium, are converted into a single photon at higher frequency ($\omega_1+\omega_2$). In the DFG processes, depicted in Fig. 2.1(c), two photons of the initial beams (ω_1 and ω_2) are converted into a single photon at lower frequency (ω_1 - ω_2). In case of SHG, depicted in Fig. 2.1(a), it can be considered special case of SFG where two photons of the same frequency are converted into a single photon at twice the frequency (2ω). SHG was first demonstrated in 1961 [36] and was the first observed nonlinear optical effect. In the case of optical rectification, it can be considered special case of DFG, where the input beam at frequency, ω, mixes with itself or another beam at the same frequency, resulting in a difference frequency, $\Delta\omega = 0$. This process was first observed by Bass et al in 1962 [37]. In addition, there is the another type of down-conversion process, OPG, where the incoming intense pump light (ω_3) is converted into two beams at different lower frequencies (ω_1 and ω_2), as is showed in Fig. 2.1 (d). In practice, the OPG process is initiated by a single intense pump field,

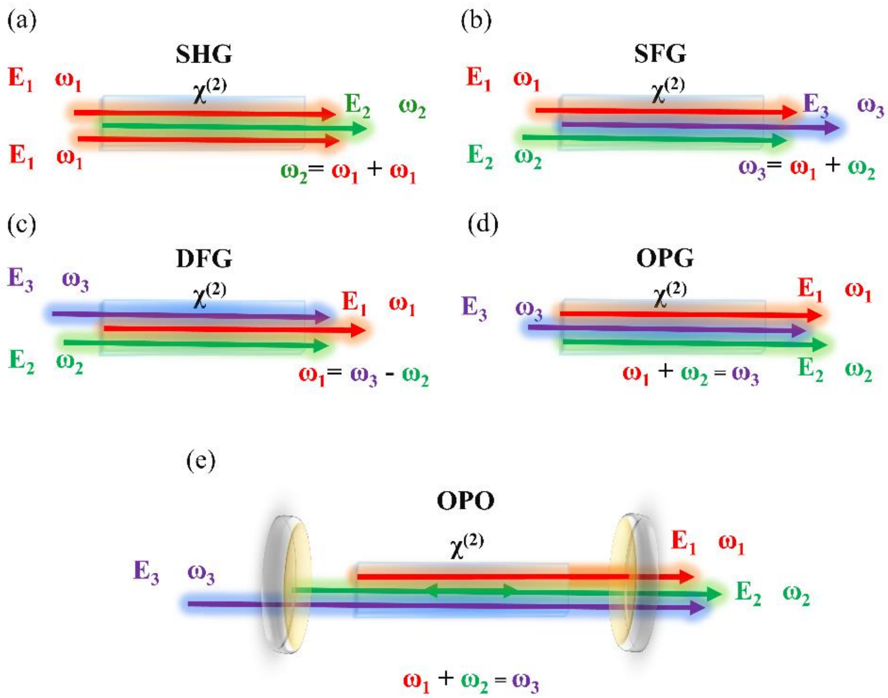

Figure 2.1: Schematic diagram of the second-order nonlinear processes.

ω_3, at the input of nonlinear material, and the pump photons will generate initial signal or idler photons by the breakup of the pump photons through spontaneous parametric emission. This process is also referred to as parametric noise or parametric fluorescence [38-40]. Then, the pump photons in turn mix with a signal field at ω_2, to give rise to an idler field at $\omega_1 = \omega_3 - \omega_2$. The generated idler field in turn mixes back with the pump to produce additional signal photons. The regenerated signal photons remix with the pump photons to produce more idler photons. The process continues in this way until power is gradually transferred from the strong pump to the initially weak signal and idler fields through the nonlinear interaction in the medium. When satisfying the phase-matching condition, as discussed later in this section, the generated signal and idler fields will undergo macroscopic amplification by continually draining power from the input pump field as they propagate through the nonlinear medium. The OPG process is a consequence of parametric fluorescence, and thus always occurs in the nonlinear material. The generated and amplified signal and idler frequencies are determined by the phase-matching condition, where the signal is generally the field with the shorter wavelength. If the OPG process occurs within an optical cavity with resonance frequency ω_2, see Fig. 2.1(e), and the gain exceeds the cavity loss, then oscillation starts, and the device is referred as an OPO. It is possible to make the OPO cavity resonant for the signal or idler, or both, where the OPO is refer to as *singly-resonant oscillator* (SRO) and *doubly-resonant oscillator* (DRO), respectively. The theory of the OPO is developed more fully in chapter 3.

2.3 Nonlinear susceptibility

The second-order nonlinear susceptibility, $\chi^{(2)}$, is a tensor represented by 3 × 3 × 3 elements, and depends on the direction of the electric field of the optical waves involved. In the tensor notation, the second-order nonlinear polarization is:

$$\boldsymbol{P}_{\boldsymbol{i}}^{(\boldsymbol{2})} = \varepsilon_0 \chi_{ijk}^{(2)} \boldsymbol{E}_{\boldsymbol{j}} \boldsymbol{E}_{\boldsymbol{k}} \qquad (2.3-1)$$

Here the first index, *i*, corresponds to the induced polarization, while the second index, *j*, and the third index, *k*, are related to the indices of the incident electric field.

Instead of the susceptibility tensor a more common description of second-order nonlinear processes is to use the *d*-matrix notation [33]:

$$\chi_{ijk}^{(2)} = 2d_{ijk} \qquad (2.3-2)$$

Clearly, *d* is a tensor quantity, and can be described by its tensor elements. Using Kleinman symmetry [41], i.e. all interacting frequencies are far from resonance frequency of the material, the frequencies involved can permute independently of the *ijk* indices. Thus, we can write the *d*-

tensor as a 3×6 matrix, d_{im}. Conventionally, the index, m, is given by the numbering scheme outlined in Table 2.1:

	j=1	j=2	j=3
k=1	m=1	m=6	m=5
k=2	m=6	m=2	m=4
k=3	m=5	m=4	m=3

Table 2.1: Numbering convention for nonlinear optical coefficients, d.

Thus, we can describe the nonlinear polarization in the expression:

$$\begin{pmatrix} P_x(\omega_3) \\ P_y(\omega_3) \\ P_z(\omega_3) \end{pmatrix} = 2\varepsilon_0 K \begin{bmatrix} d_{11} & d_{12} & d_{13} & d_{14} & d_{15} & d_{16} \\ d_{21} & d_{22} & d_{23} & d_{24} & d_{25} & d_{26} \\ d_{31} & d_{32} & d_{33} & d_{34} & d_{35} & d_{36} \end{bmatrix} \cdot \begin{pmatrix} E_x(\omega_1)E_x(\omega_2) \\ E_y(\omega_1)E_y(\omega_2) \\ E_z(\omega_1)E_z(\omega_2) \\ E_y(\omega_1)E_z(\omega_2) + E_z(\omega_1)E_y(\omega_2) \\ E_x(\omega_1)E_z(\omega_2) + E_z(\omega_1)E_x(\omega_2) \\ E_x(\omega_1)E_y(\omega_2) + E_y(\omega_1)E_x(\omega_2) \end{pmatrix} \qquad (2.3-3)$$

Here, the matrix components, d_{im}, are also known as the nonlinear coefficients of the material, where K is the degeneracy factor, which takes the value of 0.5 for SHG and optical rectification, and 1 for the other second-order conversion processes.

A further important consideration in relation to nonlinear frequency conversion processes is the crystal structural or spatial symmetry. For example, for inversion symmetry materials, if we change the sign of the applied electric field $\boldsymbol{E}(\boldsymbol{t})$, then the sign of the induced polarization must also be changed, which means

$$-\boldsymbol{P}^{\boldsymbol{NL}}(\boldsymbol{t}) = \varepsilon_0\chi^{(2)}\big(-\boldsymbol{E}(\boldsymbol{t})\big)^2 \qquad (2.3-4)$$

From equation (2.1-3), we can obtain

$$\boldsymbol{P}^{\boldsymbol{NL}}(t) = \varepsilon_0\chi^{(2)}\big(-\boldsymbol{E}(\boldsymbol{t})\big)^2 \qquad (2.3-5)$$

By comparison of equation (2.3-4) with (2.3-5), we see that $\boldsymbol{P^{NL}(t)}$ must equal to $-\boldsymbol{P^{NL}(t)}$, which is only possible if $\boldsymbol{P^{NL}(t)}$ identically vanishes, resulting in $\chi^{(2)} = 0$. Such materials are called *centrosymmetric materials*. Therefore, all second-order nonlinear optical effects are excluded in centrosymmetric materials and are only possible in non-centrosymmetric materials.

2.4 Coupled-wave equations

If we substitute for $\boldsymbol{P^{(2)}}$ and $\boldsymbol{E}$ in Maxwell's wave equation, the evolution of light through a dielectric medium without free charges and currents can be described by the wave equation:

$$\nabla^2\boldsymbol{E} - \frac{n^2}{c^2}\frac{\partial^2\boldsymbol{E}}{\partial t^2} = \frac{1}{\varepsilon_0 c}\frac{\partial^2\boldsymbol{P}^{(\boldsymbol{NL})}}{\partial t^2} \qquad (2.4-1)$$

where $\boldsymbol{P^{(NL)}}$ is the nonlinear part of the induced polarization from Eq. (2.1-2), c is the speed of light in vacuum, and refractive index n at frequency ω is represented as:

$$n = n(\omega) = \sqrt{\frac{\varepsilon(\omega)}{\varepsilon_0}} \qquad (2.4-2)$$

$\varepsilon(\omega)$ is the permittivity of the medium at frequency ω, and ε_0 is the permittivity of free space. To simplify the discussion, we assume that the applied fields, $\boldsymbol{E_i}$, (i = 1, 2, 3), are infinite uniform plane waves propagating only in the z-direction, and define each field as

$$\boldsymbol{E_i}(z,t) = \frac{1}{2}\{\boldsymbol{A_i}(z,\omega)\, exp[i(\omega t - kz)]\} + c.c \qquad (2.4-3)$$

Since the applied fields depend only on the coordinate *z*, we can replace ∇^2 by d^2/dz^2. Generally, the wave equation holds for all involved frequency components in the mixing process, so we can obtain three separate wave equations at each frequency for wave mixing processes [33]:

$$\frac{d^2A_1}{dz^2} + 2ik_1\frac{dA_1}{dz} = \frac{-4d_{eff}\omega_1^2}{c^2}\, A_3A_2^*e^{-i(k_1+k_2-k_3)z} \qquad (2.4-4a)$$

$$\frac{d^2A_2}{dz^2} + 2ik_2\frac{dA_2}{dz} = \frac{-4d_{eff}\omega_2^2}{c^2}\, A_3A_1^*e^{-i(k_1+k_2-k_3)z} \qquad (2.4-4b)$$

$$\frac{d^2A_3}{dz^2} + 2ik_3\frac{dA_3}{dz} = \frac{-4d_{eff}\omega_3^2}{c^2}\, A_1A_2e^{i(k_1+k_2-k_3)z} \qquad (2.4-4c)$$

For interactions (linear and nonlinear), using the *Slowly Varying Envelope Approximation* (SVEA), where the field amplitudes vary only slowly over distances compared to a wavelength in space and the optical period in time, the wave Equation (2.4-4) can be simplified to the following three coupled amplitude equations:

$$\frac{dA_1}{dz} = \frac{2id_{eff}\omega_1^2}{k_1c^2}\, A_3A_2^*e^{-i\Delta kz} \qquad (2.4-5a)$$

$$\frac{dA_2}{dz} = \frac{2id_{eff}\omega_2^2}{k_2c^2}\, A_3A_1^*e^{-i\Delta kz} \qquad (2.4-5b)$$

$$\frac{dA_3}{dz} = \frac{2id_{eff}\omega_3^2}{k_3c^2}\, A_1A_2e^{i\Delta kz} \qquad (2.4-5c)$$

where $k_j = n_j\omega_j/c$ (*j*=1, 2, 3) is the wave vector, Δk is wave vector mismatch represented as $\Delta k = k_1 + k_2 - k_3$, which will be discussed later in more detail. d_{eff} is the effective nonlinear coefficient. These are the coupled-wave equations governing the parametric interaction in a dielectric medium and apply universally to any three-wave mixing process involving the second-order susceptibility. It is clear that through the effective nonlinear coefficient d_{eff}, the amplitudes of the three fields are coupled to one another. Physically, this coupling provides the mechanism for the exchange of energy among the interacting fields as they propagate through the nonlinear medium. The energy flow direction in a given three-wave mixing process depends on the relative phase and the intensity of the input fields.

2.5 Gain and amplification in parametric interactions

The general solution of the three coupled amplitude equations shown in Eq. (2.4-5), are Jacobi's elliptic functions [42]. However, by using some assumption that one of the incoming wave, termed pump in our analysis, is much stronger than the other two, an analytical solution can be found. In this special simplification, which is known as the undepleted pump approximation, the pump amplitude, A_3, can be considered to be constant along the propagation direction, which means $(dA_3)/dz=0$. In this case, the resulting coupled equation will reduced to a two linear coupled equations with A_3 independent of z, and after some manipulation, we arrive at:

$$\frac{dA_1}{dz} = \frac{2id_{eff}\omega_1^2}{k_1c^2} A_3A_2^*e^{-i\Delta kz} \qquad (2.5-1a)$$

$$\frac{dA_2}{dz} = \frac{2id_{eff}\omega_2^2}{k_2c^2} A_3A_1^*e^{-i\Delta kz} \qquad (2.5-1b)$$

Taking into consideration of the initial condition, zero input idler field, $A_2(z=0)=0$, and non-zero input signal, $A_1(z=0)\neq 0$, the net fractional gain in the signal intensity after propagation through the nonlinear crystal can be derived as [35]:

$$G_1(L) = \frac{I_1(z=L)}{I_1(z=0)} - 1 = \Gamma^2L^2\frac{sinh^2[\Gamma^2L^2-(\Delta kL/2)^2]^{1/2}}{[\Gamma^2L^2-(\Delta kL/2)^2]} \qquad (2.5-2)$$

where L is the interaction length, $I_1 = nc\varepsilon_0 E_1 E_1^*/2$ is the intensity, Δk is the phase-mismatch, and Γ is the gain factor defined as:

$$\Gamma^2 = \frac{8\pi^2 d_{eff}^2}{c\varepsilon_0 n_1 n_2 n_3 \lambda_1 \lambda_2} I_3(0) \qquad (2.5-3)$$

Here, n is the refractive index, λ is the wavelength of the respective waves in vacuum, and $I_3(0)$ is the input pump intensity. In some situations of practical interest, the gain factor is also expressed in the form [35]:

$$\Gamma^2 = \frac{8\pi^2 d_{eff}^2}{c\varepsilon_0 n_0^2 n_3 \lambda_0^2}(1-\delta^2) I_3(0) \qquad (2.5-4)$$

where δ is called the degeneracy factor defined through,

$$1+\delta = \frac{\lambda_0}{\lambda_2}, \qquad 1-\delta = \frac{\lambda_0}{\lambda_1}\ (0 \le \delta \le 1) \qquad (2.5-5)$$

The degenerate wavelength is, λ_0, given by $\lambda_0 = 2\lambda_3$, and n_0 is the refractive index at degeneracy, with $n_0 \sim n_1 \sim n_2$ assumed. It is clear from Eq. (2.5-4) that the parametric gain in an amplification process has a maximum value at degeneracy, where $\delta \sim 0$, and the gain decreases for operation away from degeneracy, as $\delta \rightarrow 1$. Now, we consider the net single-pass signal gain under different pumping conditions. In the high-gain limit, where $\Gamma^2 \gg (\Delta k/2)^2$, the single-pass gain reduces to:

$$G_1(L) = \frac{1}{4} exp(2\Gamma L) \qquad (2.5-6)$$

which corresponds to the case of high-intensity, pulsed, and amplified laser pump sources. Alternatively, pumping by a CW or low-peak-power pulsed laser, this corresponds to the low-gain limit of parametric generation, with $\Gamma^2 < (\Delta k/2)^2$or $\Gamma L < 1$, the single-pass gain approximates to:

$$G_1(L) = \Gamma^2 L^2 sinc^2\left\{L \cdot |[\Gamma^2 - (\Delta k/2)^2]|^{1/2}\right\} \qquad (2.5-7)$$

When $\Gamma^2 \ll (\Delta k/2)^2$, the term of inside *sinc* function will be replaced by ($\Delta kL / 2$). When near phase-matching $\Delta k \approx 0$ and $\Gamma L << 1$, the single-pass power gain will be:

$$G_1(L) = \Gamma^2 L^2 \qquad (2.5-8)$$

Therefore, under the phase-match condition (Δk = 0), the single-pass signal gain has a quadratic dependence on ΓL in the low-gain limit, whereas it increases exponentially with $2\Gamma L$ in the high-gain limit.

2.6 Phase-matching

Momentum conservation, or often-called the phase-matching condition, is a crucial requirement and widespread used concept in many energy-conserving multiphoton processes including SFG, DFG, OPG, and even the extreme nonlinear optical process of high-order harmonic generation. Phase-mismatch originates from material dispersion and causes a lack of momentum conservation between the photons involved in the nonlinear processes. With an appropriate design the material, the phase-matching condition can be achieved and the energy of input wave will transferred to the generated waves. However, if there is phase-mismatch in the nonlinear frequency conversion process, it will prevent microscopic nonlinear sources from combining constructively, resulting in destructive interference and poor generation efficiency. To overcome this limitation and improve the efficiency of frequency conversion, some compensation techniques have been developed including the birefringent phase-matching and widely used quasi-phase-matching. Implementing each technique poses a number of challenges. Other important parameters relevant to phase-matching, such as walk-off, acceptance bandwidth and tuning characteristics will be introduced.

2.6.1 Birefringent phase-matching

From the proceeding discussion, it may be concluded that the efficiency of a nonlinear frequency conversion process mainly depends on the phase-matching condition. Mathematically, the phase-matching term is given by:

$$\Delta \boldsymbol{k} = \boldsymbol{k_1} + \boldsymbol{k_2} - \boldsymbol{k_3} \qquad (2.6-1)$$

where $\boldsymbol{\Delta k}$ is the wave vector mismatch, and $\boldsymbol{k_1}$, $\boldsymbol{k_2}$, and $\boldsymbol{k_3}$ are the wavevectors of the signal, idler and pump beam, respectively. As mentioned in the previous section, the signal is generally the wave with shorter wavelength.

Since the nonlinear medium in general exhibits different refractive indices to the pump, signal and idler waves, the phase-matching condition, $\Delta k = 0$, is often difficult to achieve due to normal dispersion, where the refractive index is an increasing function of frequency. As a result, the condition for perfect phase matching with collinear beams is not possible. However, for optically anisotropic materials, the refractive index depends not only on wavelength, but also on the polarization direction of the light relative to the crystal axes. This optical property also called *birefringence*, thus the phase matching is still achievable by making use of the birefringence properties displayed by certain materials. It should be noted that, not all crystals display birefringence, in particular, crystals belonging to the cubic crystal system are optically isotropic, such as, OP-GaAs, in which it is not possible to achieve phase matching by this method.

Birefringent phase-matching (BPM) is a conventional and important phase-matching technique. In the history of nonlinear optics, an essential step toward efficient frequency conversion, taken in 1962 [36], was the use of BPM in SHG. The basic idea of BPM is that the interaction waves of different frequencies are polarized differently, so that their corresponding phase velocities can be adjusted, and thus their wave vectors can satisfy the phase-matching conditions. Here, two different perpendicular polarizations, *ordinary* (*o*) and *extraordinary* (*e*) polarization are distinguished according to the crystallographic point group of the material. In addition, for uniaxial crystals, two different cases are distinguished: *positive* and *negative* birefringent materials. In the case of a positive uniaxial crystal, the extraordinary refractive index is larger than the ordinary index, represent as $n_e > n_o$. For a negative uniaxial crystal, the opposite is true, which is $n_e < n_o$. Mathematically, the equation of the extraordinary index is given by:

$$n_e(\theta) = \left[\frac{sin^2\theta}{n_e^2} + \frac{cos^2\theta}{n_o^2}\right]^{-1/2} \qquad (2.6-2)$$

Clearly, equation (2.6-2) indicates the dependence of the extraordinary index $n_e(\theta)$ on θ. In practical operation of parametric devices, two different types of phase-matching (type I and type II) are possible. Historically, they originate from SHG experiments [43]. Here, we cite the definition of different types for parametric processes. Assuming the process is $\omega_3 \rightarrow \omega_1 + \omega_2$, then *type I* is defined to be the case in which the two lower-frequency waves have the same polarization, while *type II* is the case where the polarizations are orthogonal. In all cases of three-wave mixing processes, the situation can be summarised as in Table 2.2, where *e* represents the extraordinary polarization and *o* is the ordinary polarization.

	Pump	**Signal**	**Idler**	**Crystal Type**
Type I	*e*	*o*	*o*	Negative birefringent
	o	*e*	*e*	Positive birefringent
Type II	*e*	*e*	*o*	Negative birefringent
	e	*o*	*e*	Negative birefringent
	o	*e*	*o*	Positive birefringent
	o	*o*	*e*	Positive birefringent

Table 2.2: Type I and type II phase-matching configurations for parametric process. *e*: extraordinary polarisation ; *o*: ordinary polarisation.

For example, in a DFG process, using a positive birefringent crystal with *type I* phase matching scheme, the phase-matching condition can be expressed as follows:

$$\frac{n_o(\omega_p)}{\lambda_p} - \frac{1}{\lambda_s}\sqrt{\left(\frac{sin^2\theta_{pm}}{n_e^2(\omega_s)} + \frac{1 - sin^2\theta_{pm}}{n_o^2(\omega_s)}\right)^{-1}} = \frac{1}{\lambda_i}\sqrt{\left(\frac{sin^2\theta_{pm}}{n_e^2(\omega_i)} + \frac{1 - sin^2\theta_{pm}}{n_o^2(\omega_i)}\right)^{-1}} \quad (2.6-3)$$

where θ_{pm} is the phase-matching angle. By choosing a proper angle with respect to the crystal axis, phase-matching can be considerably efficient.

In practice, on the other hand, such conversions suffer from an inherent limitation that is Poynting vector walk-off, where the direction of the beam propagation differs from the phase front direction. The propagation direction is the direction of the energy flow given by the Poynting vector, while the direction of the phase front is given by the *k* vector. The polarization, ***P***, is only parallel to the electric field, ***E***, when it oscillates along the principal axis of crystal, thus the Poynting vector is often pointed at an angle to the direction of wave vector, and then the output beams will be separated. This phenomenon is known as, *spatial walk-off* or *Poynting vector walk-off*. Given the limit length of the nonlinear crystal, walk off leads to a smaller spatial overlap between the interacting beams in the crystal, thus only a limited length of crystal for the parametric waves can be used and, therefore, the conversion efficiency will be reduced. In the presence of walk-off, the effective crystal length is defined as [44]:

$$L_{eff} = \frac{\sqrt{\pi}\omega_o}{\rho} \quad (2.6-4)$$

where ω_0 is the waist radius of the input beam. ρ is the double-refraction angle, which in the case of a uniaxial crystal is expressed as:

$$\tan(\rho) = -\frac{1}{2}|n_e(\theta_{PM})|^2\left(\frac{1}{n_e^2} - \frac{1}{n_o^2}\right)\sin(2\theta_{PM}) \quad (2.6-5)$$

where θ_{PM} is the phase-matching angle. It is clear from Eq. (2.6-5) that the spatial walk-off angle in birefringent phase-matching has a minimum value at $\theta_{PM} = 90^o$ relative to principal axes of the nonlinear crystal, where spatial walk-off will be vanished, this is called *noncritical phase-matching* (NCPM). Otherwise, it is referred to as *critical phase-matching* (CPM). In the NCPM configuration, due to the vanishes of spatial walk-off, the nonlinear crystal length becomes the effective interaction length of the nonlinear optical process.

In the BPM scheme, it is possible to greatly enhance the frequency conversion efficiency by NCPM. However, it needs to be borne in mind that BPM does not allow access to all the coefficients of the second-order nonlinear susceptibility tensor [45]. In particular, in any ferroelectric crystal, the highest coefficient, d_{11}, d_{22}, and d_{33} cannot be purely solicited by BPM because this requires the interacting beams to be in different polarizations, which is not the case with the diagonal matrix elements.

2.6.2 Quasi-phase-matching

In BPM method, many desirable OPO implementations are limited by spatial walk-off, low effective nonlinear coefficient, and inconvenient phase-matching temperatures and angles. Specially, the largest nonlinear coefficient cannot be used in many cases for the frequency conversion process. An example is the well-known negative birefringent material, $LiNbO_3$, d_{33} is the largest nonlinear coefficient, which implies that the polarizations of all three beams are the same. Unfortunately, in BPM, this coefficient cannot be used, as it is neither compatible with *type I*, nor *type II* phase-matching (see Table 2.2 above). In addition, some semiconductor crystals have large nonlinearities, as well as other desirable properties such as availability in good quality and relatively large size, but phase matching is not possible by BPM, thus alternate approaches of compensation of phase-mismatch are desirable.

For a frequency-conversion process, such as OPG or SHG, the phase-mismatch is accumulated with increasing interaction length. After travelling a short distance known as the *coherent length*, given by $L_{coh}=\pi/\Delta k$, the conversion efficiency reduces and energy flows back from the generated waves to the pump. For a crystal length much longer than the coherence length, the efficiency will behave in the way of the Maker fringes [33]. One way to avoid this conflict is to use periodically-poled nonlinear materials and take advantage of the so-called *quasi-phase matching* (QPM). The QPM technique was first proposed by Armstrong and Bloembergen in 1962 [42], prior to the introduction of BPM. However, it was first demonstrated in 1966 [46], after BPM was demonstrated. The basic idea of QPM is to periodically flip the sign of the nonlinear susceptibility with a period twice the coherence length, i.e., the sign of $\chi^{(2)}$ tensor is modulated along the propagation direction of the beams by means of electric field poling, as illustrated in Fig. 2.2. This modulation will introduce extra complexity to the coupled field equations, which provides a net compensation for the phase-mismatch between the interacting waves. Consequently, the conversion efficiency increases quasi-continuously with interaction length.

Mathematically, the periodic inversion of the nonlinear coefficient is described by a Fourier series. In order to be valid for QPM, the coupled amplitude equations, Eq. (2.4-5), need to be slightly adjusted, where the term d_{eff}(z) now shows a *z* dependency. With a periodic change of the sign of the nonlinear coefficient, the d_{eff}(z) term can simply be described by [34]:

$$d_{eff}(z) = d_{eff}\mathrm{sign}[\cos(2\pi z/\Lambda)] \qquad (2.6-6)$$

Using Fourier expansion, the effective nonlinear coefficient, d_{eff}(z), can be written in the following way:

$$d_{eff}(z) = d_{eff}\sum_{m=-\infty}^{\infty} G_m e^{iK_m z} \qquad (2.6-7)$$

where the grating vector, K_m, is given by:

$$K_m = \frac{2\pi m}{\Lambda} \qquad (2.6-8)$$

Here, Λ is the period of the grating, and the Fourier coefficients, G_m, is given by:

$$G_m = \frac{2}{m\pi}\sin(m\pi D) \qquad (2.6-9)$$

where D is the duty cycle, defined by the length of reversibly poled domain divided by the grating period, Λ. Usually, the duty cycle is twice the coherence length, so that D = 0.5, and, therefore, the coefficients G_m are to be given by:

$$G_m = \frac{2}{m\pi}\sin(m\pi/2) \qquad (2.6-10)$$

where m refers to the order of the QPM. For first-order QPM, m=1, with a 50% poling duty cycle, the effective nonlinear coefficient can be simplified as:

$$d_Q = \frac{2}{\pi} d_{eff} \qquad (2.6-11)$$

And now the effective phase-mismatch parameter is the summation of the dispersion phase-mismatch and an artificial phase-mismatch, and can be written as:

$$\Delta k_Q = k_p - k_s - k_i - \frac{2\pi}{\Lambda} \qquad (2.6-12)$$

To achieve efficient QPM, the modulation period can thus be chosen such that Δk_Q= 0, and so phase-matching will be obtained.

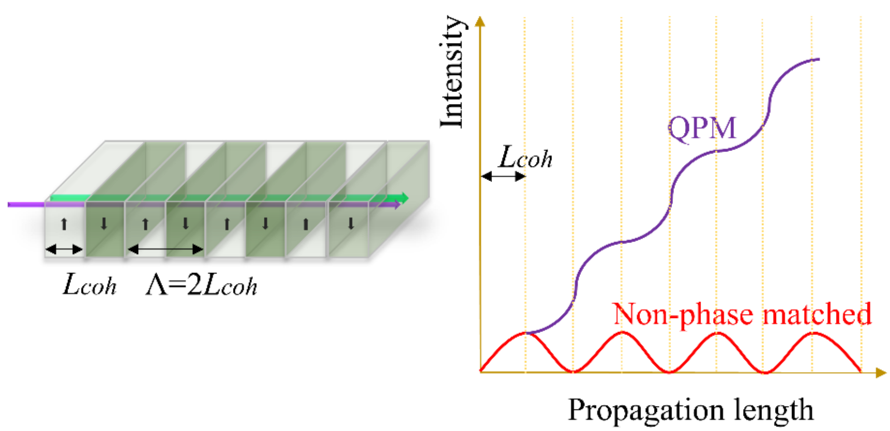

Figure 2.2: Schematic of QPM technique using a stack of uniaxial crystals of alternating *c*-axis directions. Λ: grating period, L_{coh}: coherence length.

For a QPM device, any interaction within the transparency range of the material can be noncritically phase-matched at a specific temperature, even interactions for which BPM is impossible. Another key advantage of this method is that the polarization of interacting waves can be chosen so that coupling occurs through the largest element of the $\chi^{(2)}$ tensor. For example, in an PPLN OPO, one can use the largest nonlinear coefficient (d_{33}) by choosing the pump, signal, and idler waves polarizition parallel to the *z* axis ($e \rightarrow e+e$), yielding a gain enhancement over the birefringently phase-matched process of $(2d_{33}/\pi d_{31})^2 \approx 20$. In addition, the extraordinary polarization experiences lower absorption loss through the transmission window of the material than the corresponding ordinary polarization, which can further reduce the threshold of OPO.

2.7 Acceptance bandwidth

As introduced from the preceding discussion, we know that the parametric interaction process is strongly dependent on the phase-matching term, Δk, where

$$\Delta k = k_p - k_s - k_i \tag{2.7-1}$$

The conversion efficiency reaches maximum at $\Delta k = 0$, and decreases rapidly with increasing wave-vector mismatch when $\Delta k \neq 0$. Thus, it is important to quantify the consequence of variation of Δk from 0, due to variations of wavelength, angle, or temperature.

As the discussed in Eq. (2.5-7), the single-pass gain is a $sinc^2$ function at the low-gain limit of parametric generation. Since $sinc^2$ curve will decrease by a factor of 2 when $\Delta kL/2 = \pm 1.39$, see Fig. 2.3, thus the acceptance bandwidth is the deviation, $\Delta\xi$, of the dispersive parameter, ξ ($\xi = \lambda, \theta, T$), leading to a phase-mismatch variation, Δk, from 0 to $2.78/L$, where L is the crystal length. Solving for the wavelength range, $|\Delta k| < 2.78/L$, that yields the phase-matching bandwidth.

Mathematically, the acceptance bandwidth can be determined by expressing the phase- mismatch term, Δk, as a Taylor series, through first order, as a function of dispersive parameter ξ, and solving for $\Delta\xi$:

$$\Delta k = \frac{\partial(\Delta k)}{\partial \xi} \cdot \delta\xi + \frac{1}{2}\frac{\partial^2(\Delta k)}{\partial \xi^2} \cdot (\delta\xi)^2 + \cdots \tag{2.7-2}$$

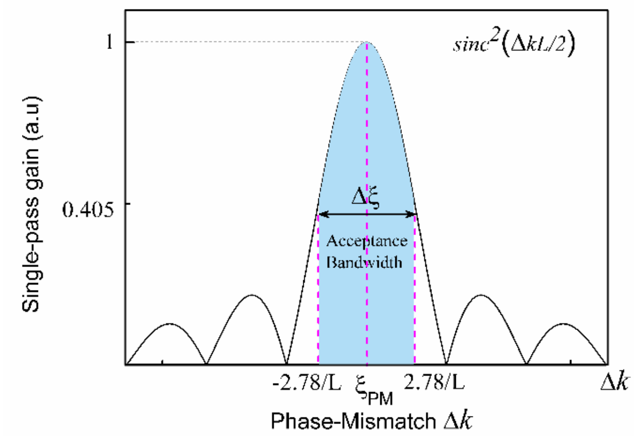

Figure 2.3: Single-pass gain as a function of phase-mismatch Δk. ξ: dispersive parameter of the refractive indices. ξ_{PM} is the value satisfying phase-matching; $\Delta\xi$ is the full-width of the curve at 0.405 of the maximum.

For example, DFG process in a QPM nonlinear material, the phase-mismatch is given by:

$$\Delta k = 2\pi \left[\frac{n(\lambda_P)}{\lambda_P} - \frac{n(\lambda_S)}{\lambda_S} - \frac{n(\lambda_{DFG})}{\lambda_{DFG}} - \frac{1}{\Lambda} \right] \qquad (2.7-3)$$

Assuming the process is phase-matched at signal wavelength λ_s, when the input signal wavelength changes by $\delta\lambda_s$, through the first order in $\delta\lambda_s$, the phase-mismatch is hence described by:

$$\Delta k(\lambda) = \frac{2\pi\delta\lambda_s}{\lambda_s} \left[\left.\frac{n(\lambda_s)}{\lambda_s}\right|_{\lambda_s} - \left.\frac{\partial\big(n(\lambda_s)\big)}{\partial\lambda_s}\right|_{\lambda_s} \right] \qquad (2.7-4)$$

Using the condition of $-2.78\,/\,L < \Delta k < 2.78/L$, we finally obtain the spectral acceptance bandwidth:

$$\delta\lambda_{FWHM} = \frac{0.885\lambda_s/L}{\left[\left.\frac{n(\lambda_s)}{\lambda_s}\right|_{\lambda_s} - \left.\frac{\partial\big(n(\lambda_s)\big)}{\partial\lambda_s}\right|_{\lambda_s} \right]} \qquad (2.7-5)$$

Here, $n(\lambda_S)$ refers to the refractive index at the signal wavelength, L is the length of the nonlinear crystal, respectively. In practice, the phase-matching bandwidth is usually too small, but it can be increased as the crystal gets thinner or the dispersion decreases. Similarly, assuming the process is phase-matched at temperature T_0, and then the temperature acceptance bandwidth can be derived as:

$$\delta T_{FWHM} = \frac{0.885/L}{\left[\frac{1}{\lambda_P}\frac{\partial\left(n(\lambda_p)\right)}{\partial T}\bigg|_{T_0} - \frac{1}{\lambda_s}\frac{\partial\left(n(\lambda_s)\right)}{\partial T}\bigg|_{T_0} - \frac{1}{\lambda_{DFG}}\frac{\partial\left(n(\lambda_{DFG})\right)}{\partial T}\bigg|_{T_0}\right]} \quad (2.7-6)$$

For example, the temperature acceptance bandwidths for a 40-mm-long orientation patterned gallium phosphide, OP-GaP crystal are shown in Fig. 2.4. By using the Sellmeier equations reported in [47], the phase matching temperature and temperature acceptance bandwidth, pumped by 1064 nm and 1766 nm, for 2676 nm of DFG generation, are calculated to be T =113° and ΔT=1 °C, respectively.

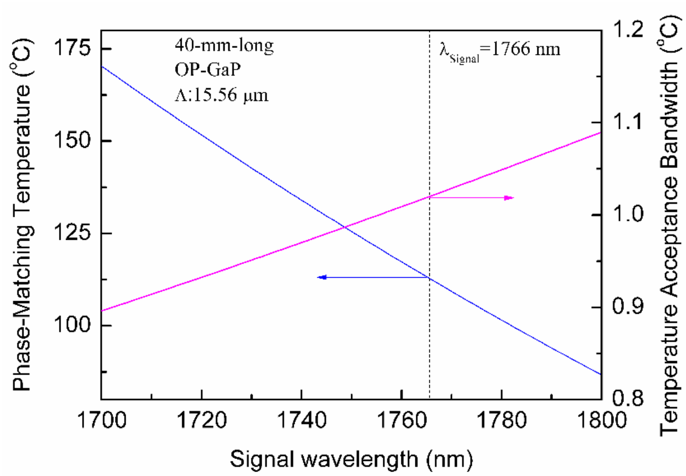

Figure 2.4: Theoretically calculated phase-matching temperature and temperature acceptance bandwidth, for the 40-mm-long OP-GaP crystal.

Chapter 3

Optical Parametric Oscillator

An optical parametric oscillator (OPO) is a device that converts a single input photon, referred as pump with frequency, ω_p, into two lower frequency photons, namely signal ω_s and idler ω_i, respectively. Conventionally, the frequency, ω_s, is larger than ω_i, and these frequencies obey $\omega_p = \omega_s + \omega_i$. Such an OPO can be built by placing a nonlinear crystal into a resonant cavity, which has some similarities with lasers: a gain material is placed in a resonator cavity. Both lasers and OPOs have a threshold of operation and emit coherent radiation. However, there are some essential differences. In the OPO devices, there is no energy stored in the crystal. However, in a laser, it is inevitable that a fraction of the pump energy is not converted to the laser output but, instead, it is absorbed by the material. In addition, in a laser, the phase of the pump is irrelevant to the phase of output laser. However, in an OPO, the phases of the output beams are often directly related to the phase of the pump laser.

To successfully assemble an OPO, it is necessary to attain sufficient gain for the parametric waves to overcome parasitic losses in the cavity. Many more choices need to be made to overcome the losses. From the pump source to the nonlinear material to cavity geometry, many factors determine the overall efficiency for signal and idler wave generation. This section outlines some of the major design choices for an OPO.

3.1 Laser pump source

The selection of the laser source to pump an OPO is mainly determined by the phase-matching requirements to access the wavelength region of interest. Clearly, the wavelength of the laser and all parametric waves should be within the transparency range of the crystal. Furthermore, the laser power plays an important role. However, for high pump intensities, other nonlinear processes such as optical parametric generation (OPG) and optical parametric amplification (OPA) will compete with OPO. Unwanted side effects of such processes such as, an enlarged linewidth of the generated light will appear. A final issue need to be considered is the laser linewidth and spatial coherence. Since the parametric gain is critically dependent on the phase-mismatch parameter, and practical laser sources have finite spectral bandwidth and spatial divergence, despite the use of phase-matching techniques, all the spectral and spatial components of the beam cannot be brought into perfect phase unison simultaneously to realize perfect phase-matching. Hence, the pump laser should have high spectral and spatial coherence, and the required linewidth and beam divergence can be calculated from considerations of the phase-matching condition.

3.2 Nonlinear material

3.2.1 General considerations

The implementation of an OPO requires selecting a pump laser as well as a proper nonlinear medium. Several parameters need to be considered, for example, the selected nonlinear material needs to be transparent for the pump, signal and the idler. The nonlinear coefficient should be as high as possible for high conversion efficiencies, and the material must have a high damage threshold to be able to endure high intensities, especially if high output power is to be achieved. Obviously, the selection of pump laser and the crystal has to be carefully matched. With the advent of new nonlinear crystals, particularly periodically-poled materials, and novel laser sources, many new combinations have become possible. Table 3.1 summarize the most important properties of various nonlinear crystals, which have been used for parametric generation. As described by equation (2.5-7) in the chapter 2, the parametric gain is proportional to $d_{eff}/\sqrt{n_p n_s n_i}$, customarily called it as nonlinear *figure-of-merit*:

$$FOM \equiv d_{eff}/\sqrt{n_p n_s n_i} \qquad (3.2-1)$$

FOM is commonly used factor to evaluate the overall quality of the nonlinear crystal. It is proportional to the effective nonlinearity, and inversely proportional to the square-root of the refractive indices of the material. Since infrared materials, in general, have higher refractive indices, hence it would be expected to have a lower *FOM* in such materials.

It is also desirable for the nonlinear material to display large tolerances to possible deviations in the spectral and spatial quality of the pump laser, since the parametric gain bandwidth of the nonlinear medium is limited by the phase-matching condition. Detailed calculations depend on the type of phase-matching and the dispersion properties of the specific nonlinear material. For a given crystal length, there is an upper limit to the maximum allowable pump linewidth and angular divergence for efficient parametric generation. On the other hand, for a given pump linewidth and angular divergence, there is also an upper limit of the useful crystal length for achieving maximum nonlinear gain. In general, for the attainment of maximum nonlinear gain and a minimum OPO threshold, it is advantageous to use materials with large spectral, angular, and temperature acceptance bandwidths.

For a birefringent anisotropic medium, an important issue need to be considered in selecting the material is the spatial walk-off. As discussed in chapter 2, the spatial walk-off length is linearly proportional to the beam waist radius, thus large spot sizes should be used for long interaction lengths. However, achieving high gain in nonlinear processes in turn requires a high pump intensity, so that small beam radius is needed. Therefore, a good balance between the crystal length and beam radius must be maintained to achieve practical efficiencies. Therefore, in the presence of double-refraction, in addition to the acceptance bandwidth considerations, the spatial walk-off places extra restriction on the maximum crystal length.

Crystal	Transparent (µm)	d_{eff} (pm/V)	Damage-threshold (GW/cm^2)
$AgGaS_2$[48,49]	0.46-13	d_{36}=17.5	0.025
$AgGaSe_2$[48,49]	0.71-19	d_{36}=33	0.025
β-BaB_2O_4 (BBO) [48,49]	0.2-2.6	d_{22}=2.3	9.9[50,51]
KD_2PO_4 (DKDP) [48,49]	0.19-1.6	d_{36}=0.37	0.5[52]
KH_2PO_4 (KDP) [48,49]	0.19-1.3	d_{36}=0.39	8.4[53]
$KTiOPO_4$ (KTP) [48,49]	0.34-3.2	d_{15}=3.6	0.16-3[54,56]
LiB_3O_5 (LBO) [48,49]	0.2-3.2	d_{31}=0.85	18-25[57,58]
$LiNbO_3$ (PPLN) [48,49]	0.35-5.5	d_{15}=-4.3/ d_{33}=-27	0.84-20[59,62]
$ZnGeP_2$ (ZGP) [48,49]	0.74-12	d_{36}=69	0.08-30[63,65]
$CdSiP_2$ (CSP) [66,67]	1-6.5	d_{14}=53/ d_{36}=84.5	4.4[68,69]
OP-GaAs [70,71]	0.9-17	d_{14} =94	0.06 [72]
OP-GaP [47,73]	0.57-12	d_{14} =50	0.041 [74]

Table 3.1: Important properties of different nonlinear crystals commonly used for parametric generation. d_{eff} denotes the nonlinear optical coefficient. The damage threshold is given in GW/cm^2 for nanosecond pulse duration.

3.2.2 Thermal effects and damage limitations

Laser-induced absorption in a linear and nonlinear material is perhaps the ultimate limitation in parametric processes. The most common result of absorption is the thermal effects, which degrade the perfect phase-matching, and hence reduce the conversion efficiency of the device. In addition to thermal effects, absorption will also introduce thermal lensing, which will degrade spatial mode-matching between the pump and the generated waves, and can also lead to laser-induced material damage. Since the absorption is related to the concentration of impurities and native defects, hence, proper care and improvement in the growth techniques are important in reducing the intrinsic absorption of nonlinear materials.

Beside absorption at the pump wavelength leading to low efficiency of the parametric devices, laser-induced damage is another issue for the design and successful operation of parametric devices. Laser-induced damage includes photorefractive damage and physical damage. Physical damage is very much dependent on crystal growth, impurity level and preparation conditions. The *photorefractive damage* is a nonlinear optical effect seen in certain crystals, which is a light-induced index change phenomenon. Photorefractive damage leads to beam distortions, non-uniformities, and instabilities in the output beam. However, unlike physical damage, it is a reversible damage mechanism, and can be alleviated by illuminating the crystal with ultraviolet radiation or by elevating its temperature.

3.3 Oscillator configurations

Unlike in the case of a conventional laser, OPO involves three-wave interaction. Hence, any or all of the three waves can be resonated in the cavity, while partially extracting the desired wave. In order to provide feedback in an OPO, a variety of resonance schemes may be deployed by suitable choice of mirrors forming the optical cavity, which are illustrated in Fig. 3.1. The mirrors may be highly reflecting only for one of the parametric wave (signal or idler), as depicted in Fig. 3.1(a), in this case the device is known as a SRO. This configuration is characterized by the highest CW operation threshold. In order to reduce operation threshold of the OPO with regard to required

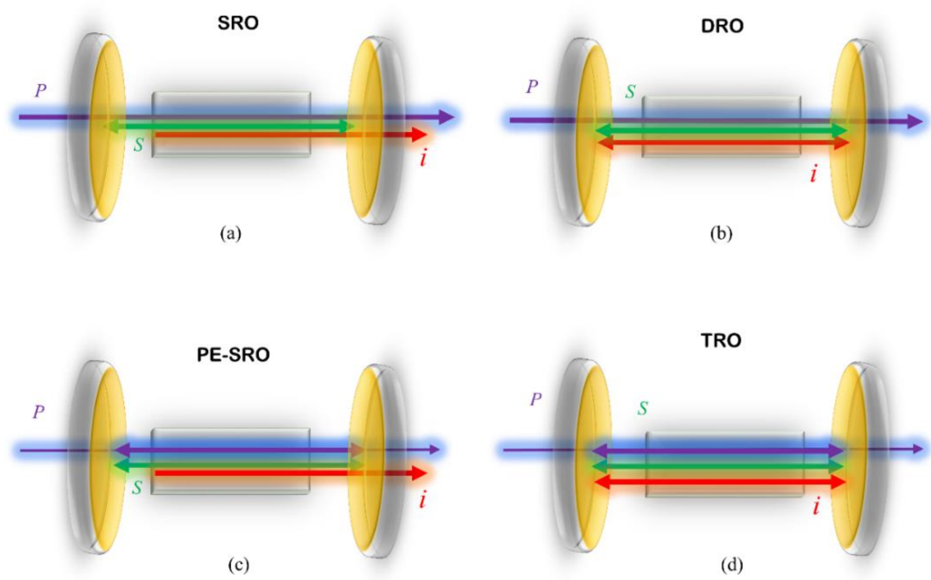

Fig. 3.1: Cavity resonance configurations for CW OPOs. The symbols *p*, *s*, and *i* denote pump, signal, and idler, respectively.

pump power is reduced, alternative resonator schemes can be deployed, where additional optical waves are resonated in the cavity. These include the DRO, as shown in Fig. 3.1(b), where both the signal and idler waves are resonant in the optical cavity, and *pump-enhanced SRO*, as depicted in Fig. 3.1(c), where the pump as well as one of the generated waves (signal or idler) is resonated. In an alternative scheme, shown in Fig. 3.1 (d), the pump can also be resonated together with both parametric waves, in this case the device is known as a *triply-resonant oscillator* (TRO). Such schemes can lead to substantial reductions in threshold from the CW SRO configuration, with the TRO offering the lowest operation threshold.

Compared to other configurations, DROs and TROs have a much lower threshold pump power. This is particularly useful for CW operation, where the threshold pump power is typically high due to the low parametric gain. However, stable operation of the DROs or TROs is a challenging, since each resonant wave of the OPO has to fulfill the resonance conditions, energy conservation and momentum conservation. Despite the highest operation threshold over the other OPO configurations, CW SROs offer the most viable solution for parametric generation of high-power, stable, single-frequency radiation over extended spectral regions. Here, we mainly discuss the CW

SRO, as it is most relevant to the present work. Figure 3.2 illustrates the typical cavity configurations for CW SROs device, among which the linear cavity is the simplest one, consisting of the nonlinear crystal enclosed by two mirrors.

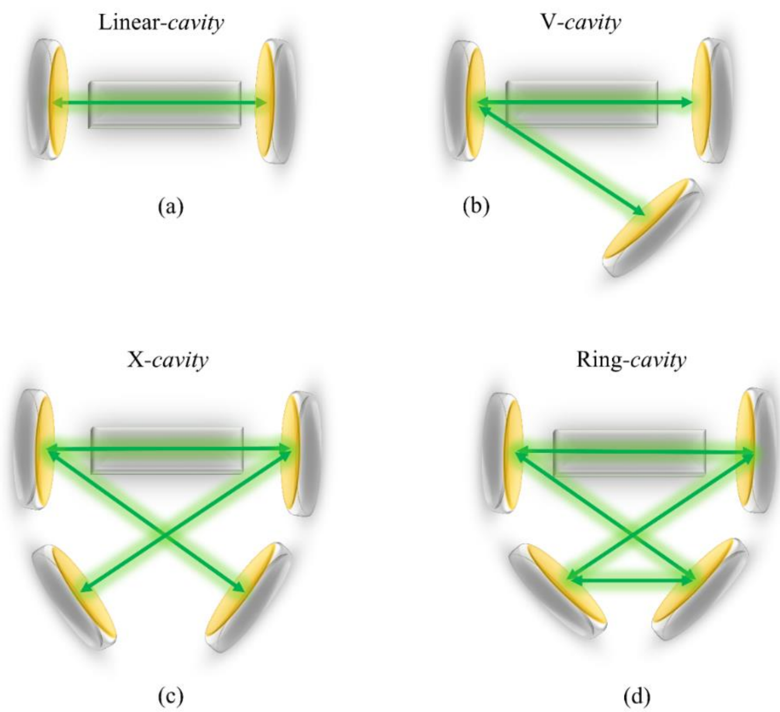

Figure 3.2: Various cavity designs: (a) Linear cavity, (b) V-cavity, (c) X-cavity, (d) Ring cavity.

The pump beam is focused at the center of the nonlinear crystal. The in-coupling mirror has high transmission for the pump and high reflection for the signal, and the output coupler mirror is partially reflecting for the signal and transmits the pump and idler. Two of the mirrors are generally curved to match the resonant modes to the pump mode. Other standing-wave cavities, the V-shaped and X-shaped cavities, shown in Fig. 3.2(b) and Fig. 3.2(c), have more flexibility of introducing additional components. For example, introducing etalons for narrowing linewidth or additional nonlinear crystals for other second-order nonlinear processes in the cavity, without exposing them to the high pump intensity. In addition, double-passing the pump radiation along with the signal is also possible to reduce the SRO threshold. Among all the configurations, the travelling-wave cavity, or ring cavity, is the most difficult configuration, as depicted in Fig. 3.2(d).

In this configuration, no pump radiation will reflect back into the pump laser, and thus there is no need an optical isolator. It also offers the possibility of introducing etalons for frequency selection, as well as controlling the second beam waist of the cavity without changing the cavity stability. Moreover, since there is only single-pass of the resonating wave through the crystal for every round-trip, it reduces the losses due to material absorption and crystal coating, and hence reduces the SRO threshold and minimizes the thermal effects within the nonlinear crystal. In the ultrafast regime, OPOs required synchronous pumping. This means that the cavity length of the OPO has to be precisely synchronized to the pump laser cavity length, so that the signal pulses experience gain due to the presence of the pump pulse in each round-trip. In the calculation of cavity length, the physical length of a standing-wave cavity is half that of the round-trip cavity length and the physical length of a travelling-wave ring cavity is equal to the round-trip cavity length.

3.4 Steady-state CW SRO threshold

In the SROs, only one of the generated waves is resonant in the cavity, and we assume it is to be the signal wave. The non-resonant idler wave grows from zero at that end of the medium to leaves the cavity after a single pass. Since the pump is propagating only in the forward direction through the medium, parametric gain only occurs in this direction. Once the gain exceeds the round-trip losses for the signal, the oscillation threshold is reached and the SRO starts to work. For confocally focused Gaussian beams, the threshold power of a CW SRO is given by [35]:

$$P_{th} = \frac{\epsilon_0 c n_s^2 n_p \lambda_p^2}{\pi^2 d_{eff}^2 h_m(B,\xi) L^2}(T_s + V_s) \qquad (3.4-1)$$

where the parameter T_s is the transmission of mirrors at the signal wave, V_s is all other losses of the signal, and $h_m(B, \xi)$ is the Boyd-Kleinman reduction factor [75]. This factor depends on the crystal properties and the focusing condition, where the lowest threshold is reached when the Boyd-Kleinman reduction factor is equal to 1, $h_m(B, \xi)= 1$.

In the pulsed regime, given the finite duration of the pump pulse, only a limited number of round-trips for the parametric waves can be made available. By using a time-dependent gain analysis, Brosnan and Byer have derived the equations governing the threshold pump energy in nanosecond pulsed SROs [76]:

$$\varepsilon_{th} = \frac{0.6\tau(\omega_p^2 + \omega_s^2)}{\kappa L_{cavity}^2}\left[\frac{25L_{crystal}}{\tau c} + \frac{1}{2}ln\frac{2}{R_s(1-V_s)}\right]^2 \qquad (3.4-2)$$

where τ is the FWHM pulse width, ω_p and ω_s are the mode radius of the pump and signal beam, respectively, L_{cavity} and $L_{crysral}$ is the cavity and crystal length, respectively. *Rs* is the reflectivity of the output coupler and *Vs* denotes all other losses of the signal.

A comparison of Eq. (3.4-1) and Eq. (3.4-2) shows that, in the nanosecond pulsed regime, the threshold depends on the cavity length, L_{cavity}, whereas this is not the case in the CW regime. Therefore, in practice, reducing the operation threshold of nanosecond pulsed SROs can be achieved by minimizing the OPO cavity length to allow maximum number of round-trips over the pump pulse interval.

In addition, for an average pump power of 10 W in optical pulses with FWHM pulse duration of 10 ns, operating at 1 kHz, the pulse peak power is roughly 1 MW. This peak power is much larger than the usual power of a CW pump laser and, consequently, the gain in the pulsed regime is much higher than in CW regime. Thus, in practice, the high gain of pulsed OPOs allows large output coupling percentages, where values >20% are not unusual. However, in CW OPOs, output coupling above 10% is rather unusual, and typically it less than 5% [77]. On the other hand, the large peak powers of pulsed OPOs imply that it easily reaches the damage threshold of the material and thus material damage remained a major limitation to the operation of high-energy nanosecond pulsed devices. Therefore, in practice, the optimum choice of experimental parameters for the attainment of minimum operation threshold in pulsed OPOs is often compromised by material damage threshold.

3.5 Wavelength tuning

One of the main advantages of an OPO is that the phase-matching conditions can be satisfied for different combinations of pump, signal and idler wavelength, which converts the OPO into a tunable laser sources. From the preceding discussion, we may conclude that the wavelengths of the generated signal and idler waves are determined by two relations, energy conservation and momentum conservation. Energy conservation determines which wavelength will be generated, if the crystal temperature T or grating period Λ_{QPM} is appropriately chosen, and thus the phase-matching condition is fulfilled. Figure 3.3 shows a typical wavelength tuning of a PPLN-based OPO by changing the crystal temperature and the domain grating period using the relevant Sellemier equations [78]. The phase-matching condition is achieved by selecting the right grating period of the PPLN crystal or by heating the crystal to the correct temperature. In Fig. 3.3(a), the optimized temperatures for efficient frequency conversion are shown for six different grating periods of the PPLN, ranging from 29µm to 31.5µm in step of 0.5µm. Figure 3.3(b) shows the generated signal and idler wavelength as a function of the grating period for room temperature, T=100^{o} and T=200^{o}.

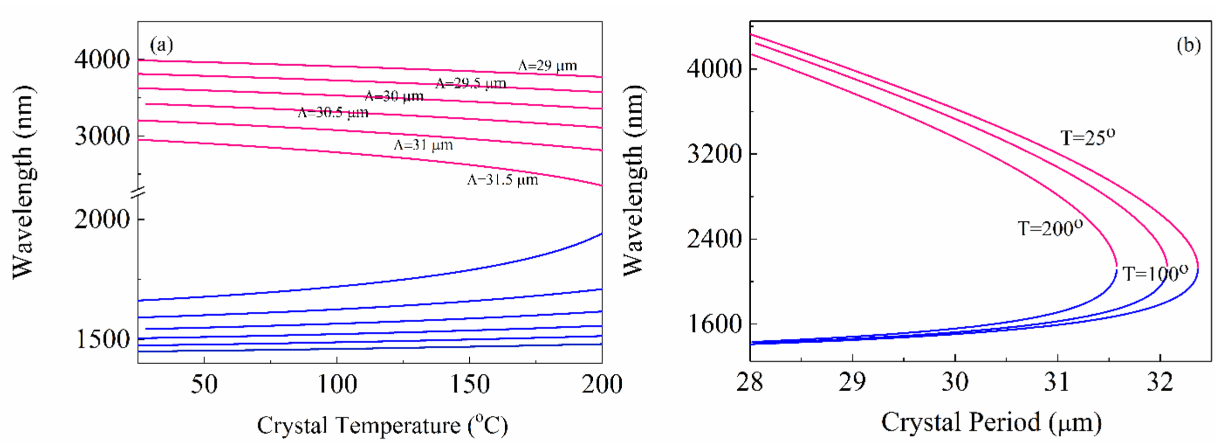

Figure 3.3: Tuning characteristics for different grating periods of the PPLN crystal. (a) Temperature tuning for six different grating periods. (b) Generated wavelength as a function of the grating period for three different temperatures.

3.6 ABCD matrix and cavity design

The performance of an OPO largely depends on the cavity design. The propagation of Gaussian beams through an optical system can be described by the ABCD matrix formalism or ray transfer matrix formalism, where the effect of each optical components on the laser beam is given by a 2 × 2 matrix.

Consider of a Gaussian beam propagating in a straight line along *z*-direction with a minimum beam waist, that is $\omega\,(z=0) = \omega_0$. If the beam waist, $\omega(z)$, and radius of curvature of the wavefront, $R(z)$, is known at a specific location of the Gaussian beam, then the beam waist, $\omega(z)$, and radius of curvature of the beam, $R(z)$, at any position can be estimated using the following equations [79]:

$$R(z) = z\left(1 + \frac{z_0^2}{z^2}\right) \qquad (3.6-1)$$

$$\omega(z) = \omega_0^2\left(1 + \frac{z^2}{z_0^2}\right) \qquad (3.6-2)$$

Here $z_0 = \pi n \omega_0^2/\lambda$ is called the *Rayleigh range*, $b = 2z_0$ is called as *confocal parameter*, n is the refractive index, and λ is the wavelength of the Gaussian beam. The field envelope of this Gaussian beam can be expressed as:

$$\mathrm{U} = \left[\frac{1}{1 - j(zn/z_0)}\right]\exp\left(-j\frac{\pi(x+y)^2}{\lambda q}\right) \qquad (3.6-3)$$

where q is the complex beam parameter of a Gaussian beam, which is related to the beam radius ω and the radius of phase front curvature R, given by:

$$\frac{1}{q} = \frac{1}{R} - j\frac{\lambda}{\pi\omega^2} \qquad (3.6-4)$$

In the paraxial approximation, the propagation of Gaussian beams through an optical system can be described by a 2 × 2 matrix. The general form of the matrix or ABCD matrix is:

$$M = \begin{pmatrix} A & B \\ C & D \end{pmatrix} \qquad (3.6-5)$$

where *A*, *B*, *C* and *D* are the matrix elements. The ABCD matrices determine the *q*-parameter of a Gaussian beam when passing through an optical system.

Assuming a Gaussian beam with parameter, q_0, its *q*-parameter after passing through the optical system, q_1, can be described by [79]:

$$q_1 = \frac{Aq_0 + B}{Cq_0 + D} \qquad (3.6-6)$$

Below is the ABCD transfer matrix of a beam traveling through free space or in a medium of constant refractive index. For example, for the propagation in free space with a length of, *d*, the ABCD matrix is given by:

$$D = \begin{pmatrix} 1 & d \\ 0 & 1 \end{pmatrix} \qquad (3.6-7)$$

Further, the matrices for the ray propagation through a lens with focal length *f* is given by:

$$L = \begin{pmatrix} 1 & 0 \\ -\frac{1}{f} & 1 \end{pmatrix} \qquad (3.6-8)$$

This also give the propagation matrix through a mirror of curvature radius, *R*, by substituting the focal length, *f*, with *R*, knowing that $f = R/2$. Here, it is to be assumed *f* is positive for converging lenses and *R* is positive for concave mirror.

In addition, when a beam propagates through a system of optical elements, it is described by the

ABCD matrix product. For example, for a beam which passes through a lens of focal length, *f*, and then propagates over a distance, *d*, the complete ABCD matrix for the system, *M*, is obtained by:

$$M = \begin{pmatrix} 1 - \frac{d}{f} & d \\ -1/f & 1 \end{pmatrix} = DL = \begin{pmatrix} 1 & d \\ 0 & 1 \end{pmatrix} \begin{pmatrix} 1 & 0 \\ -1/f & 1 \end{pmatrix} \qquad (3.6-8)$$

The general form of the ray matrix operators for several optical elements are shown in the Table 3.2.

After a complete round-trip within an optical resonator, the existence of a confined and stable Gaussian mode solution of the cavity is guaranteed by the following condition [79]:

$$\left| \frac{A + D}{2} \right| < 1 \qquad (3.6-9)$$

This is the general condition for stability of the cavity. Using these transformation matrices and the stable condition of the cavity, we can calculate the beam waist radius along the propagation path, and then design a stable cavity.

As an example, we now calculate the beam waist of a propagating beam at different positions in a ring cavity. Let us assume a 50 mm long MgO:PPLN crystal, and beam waist of pump and signal of ω_p = 63 µm, and ω_s = 78 µm, respectively, corresponding to an optimum focusing parameter, $\xi \approx 1$. The wavelengths of pump and signal are chosen to be λ_p=1064 nm and λ_s=1600 nm, respectively. The refractive index of the crystal is calculated for the pump and signal wavelengths at a crystal temperature of T = 100 ^{o}C. The beam waist of signal at different positions of a stable ring cavity is thus calculated and can be plotted shown in Fig. 3.4.

<table>
<tr><td>Translation matrix:
$$M = \begin{pmatrix} 1 & d \\ 0 & 1 \end{pmatrix}$$</td><td>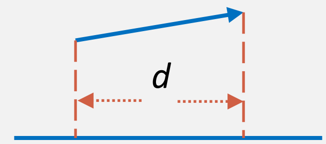
</td></tr>
<tr><td>Refraction matrix, plane interface:
$$M = \begin{pmatrix} 1 & 0 \\ \frac{n_1 - n_2}{R n_2} & \frac{n_1}{n_2} \end{pmatrix}$$</td><td>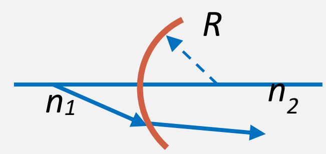

(+R): convex</td></tr>
<tr><td>Thin-lens matrix:
$$M = \begin{pmatrix} 1 & 0 \\ \frac{-1}{f} & 0 \end{pmatrix}$$
$$\frac{1}{f} = \frac{n_2 - n_1}{n_1}\left(\frac{1}{R_1} - \frac{1}{R_2}\right)$$</td><td>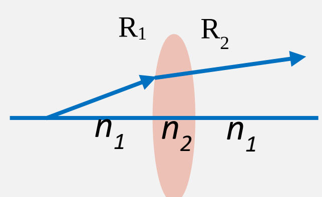

(+*f*): convex</td></tr>
<tr><td>Spherical mirror:
$$M = \begin{pmatrix} 1 & 0 \\ 2/R & 0 \end{pmatrix}$$</td><td>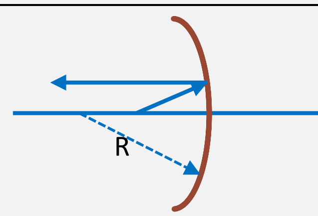

(+R): convex; (-R):concave</td></tr>
</table>

Table 3.2: Summary of some simple ray-transfer matrices

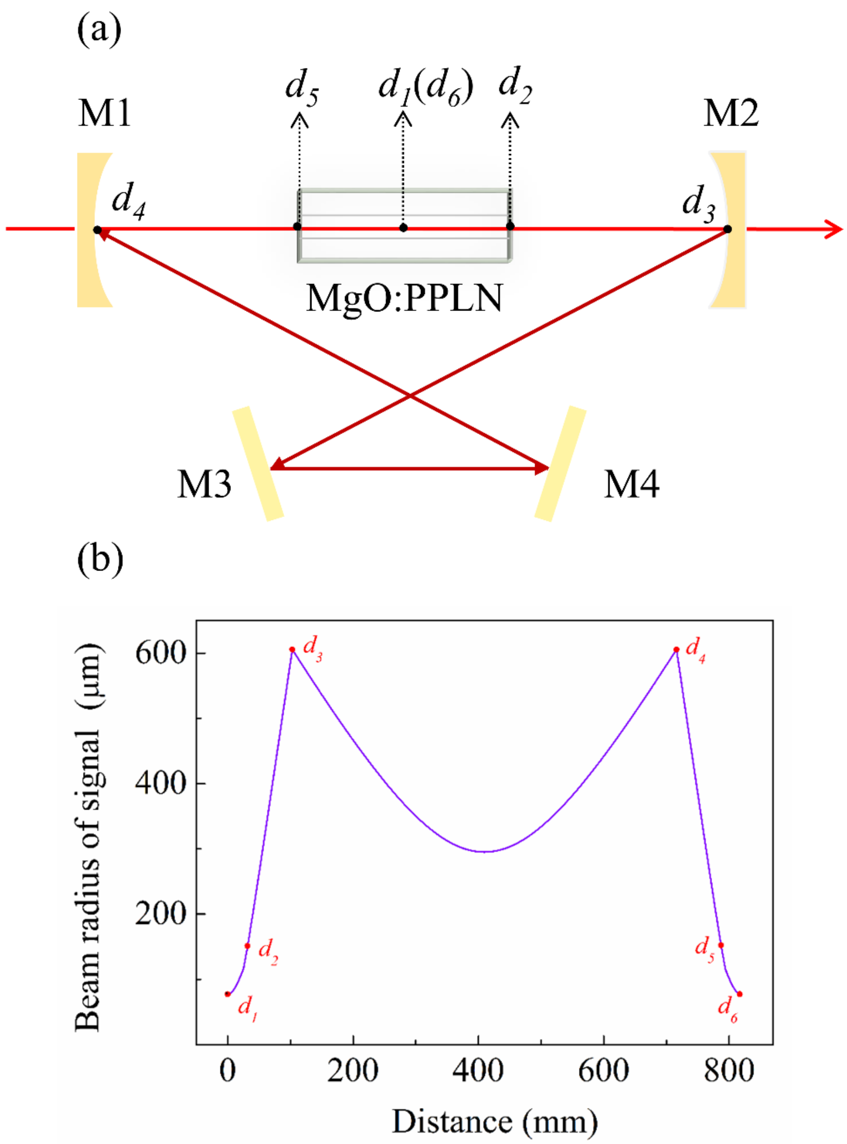

Figure 3.4: (a) Ring cavity with MgO:PPLN crystal. Start point, d_1, and end point, d_6, is at the centre of crystal. Points, d_2, and, d_5, are at output and input of crystal, respectively. d_3: Position of end curve mirror. d_4: Position of input curve mirror. (b) Beam radius of signal along the resonator.

Chapter 4

Angle-tuned MgO:PPLN OPO

This Chapter constitutes the following journal publication:

S. Chaitanya Kumar, **Junxiong Wei**, J. Debray, Vincent Kemlin, B. Boulanger, Hideki Ishizuki, T. Taira, and M. Ebrahim-Zadeh, "High-power, widely tunable, room-temperature picosecond optical parametric oscillator based on cylindrical 5%MgO:PPLN," Opt. Lett. 40, 3897-3900 (2015)

4.1 Motivation

Nonlinear frequency conversion technologies [80] offer an effective way to expand the laser wavelength range from the ultraviolet [81] to the mid-infrared (mid-IR) [77] and terahertz regions [82] based on quasi-phase-matching (QPM) techniques in nonlinear crystals. Since the first demonstration of QPM by periodic poling of the ferroelectric nonlinear materials with electric field, there has been revolutionized progress in the development and applications of parametric devices in various time scales from continuous wave [15] to ultrafast picosecond [14] and femtosecond regimes [83], providing an efficient alternative to birefringent phase-matched devices. Such devices have largely benefited from the advantages of QPM, such as, access to the highest nonlinear coefficient of the material, no spatial walk-off by using identical polarization for all the interacting waves and extended noncritical phase-matching over long interaction lengths. Additionally, the well-established periodic poling technology allows the fabrication of multiple and fanout grating [84, 85] designs, which enable phase-matching over the entire transparency range of the material. Among the QPM nonlinear materials MgO-doped periodically poled lithium niobate (MgO:PPLN) is the most widely used crystal. Besides, MgO:PPLN is now available in interaction lengths >50 mm with aperture thickness as large as 10 mm [86]. When pumped using the Nd:YAG/Yb solid-state or fiber laser at 1064 nm, MgO:PPLN has been used for development of optical parametric oscillators (OPOs) providing high output powers with wide tunability in the near-to-mid-IR region [14,15].

Although wavelength tuning can be achieved by various methods, OPOs based on QPM nonlinear crystals generally rely on slow temperature tuning, in combination with sequential or spatially varying QPM gratings to compensate for the variation of Δk due to the dispersion of the refractive indices. Figure 4.1 shows the general multiple and fanout grating designs that have been explored to realize this variation. In order to avoid walk-off, the direction of input beam is chosen along a principal axis of the crystal. Figure 4.1(a) is multiple adjacent QPM gratings scheme that place several gratings in a single crystal, typically with 0.1-0.5μm steps in period. The drawback of multigrating scheme is that it does not allow a continuous variation of the wavelength but only a discrete one due to the jump between a grating and another one. An alternative way to realize continuous tuning is to use fanout gratings. In these structures, the period is slowly ramped from one edge of the crystal to the other, presenting a continuous transversely varying period. Tuning is achieved by translating the crystal through the pump beam as depicted in Fig. 4.1(b).

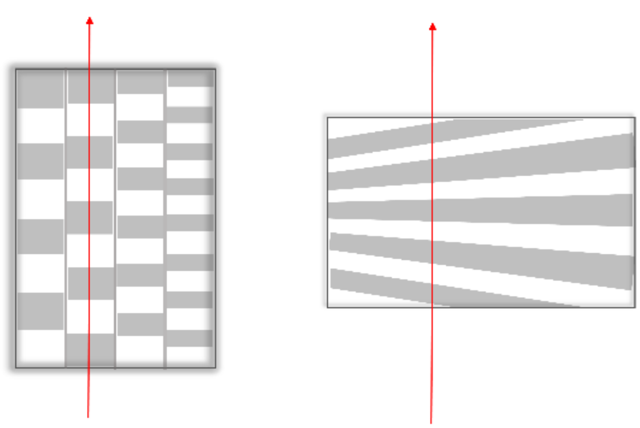

Figure 4.1: The schemes for tunable devices using QPM. (a) multi-gratings, (b) Fan-shaped gratings. The purple arrow represents the laser beam. The spectral tunability of the generated wave is obtained by translating the crystal.

The fanout design scheme enables rapid grating tuning by translation of the nonlinear crystal, while operating close to room temperature. However, the main disadvantage of fan-shaped grating is that the period varies inside the beam diameter, which will increase the spectral bandwidth.

To circumvent these disadvantages, a third scheme shown in Fig. 4.2, was proposed, where the periodically poled crystal with a single grating period Λ_0 is cut as a cylinder with the revolution axis parallel to the ferroelectric axis. Such a design allows a varying grating period by rotating the cylinder around its revolution axis, while the propagation of the beams is kept at a normal incidence for any direction.

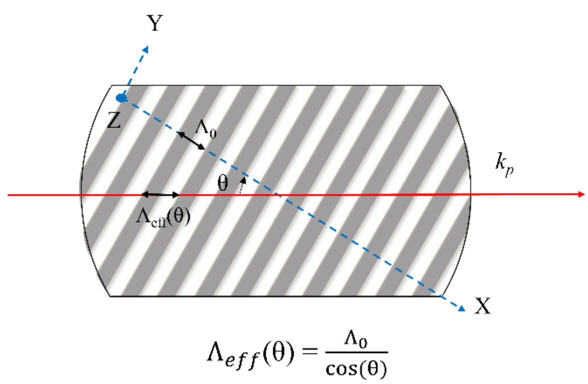

Figure 4.2: MgO:PPLN crystal cut as a partial cylinder enabling an angular interrogation with respect to the poled grating period.

To date, such angle tuned QPM OPOs include a SROs based on 50-mm-long PPLN crystal [87] and a widely tunable OPO based on 38-mm-long MgO:PPLN partial cylinder [88], both in the nanosecond regime. However, the development of an angle-tuned, picosecond OPO based on such a cylindrical geometry still remains challenging. Here we demonstrated a stable, high-power, widely tunable picosecond OPO based on a 35-mm-long MgO:PPLN partial cylinder, synchronously pumped by an Yb-fiber laser for the first time. The OPO is tunable across 1413-1900 nm in the signal together with 2418-4307 nm in the idler by angle tuning of the MgO:PPLN crystal at room temperature, providing extraction efficiencies up to ~45% in signal pulses of 15.2 ps, with good beam pointing stability. The generated signal and idler exhibit a passive power stability better than 1% rms and 0.8% rms over 15 h, measured simultaneously at 1638 nm and 3036 nm respectively in good beam quality with TEM_{00} mode profile.

4.2 Experimental configuration

The schematic of the experimental setup for the angle-tuned MgO:PPLN synchronously pumped OPO is shown in Fig. 4.3.

The fundamental pump source is a mode-locked Yb-fiber laser delivering up to 20 W of average power at 1064 nm in pulses of 20 ps duration at ~80 MHz repetition rate. The laser has a double-peaked spectrum with a full-width at half-maximum (FWHM) bandwidth of ∼1nm, resulting in a time-bandwidth product of $\Delta\upsilon\Delta\tau\sim5.3$. In addition, the output power is adjusted by using

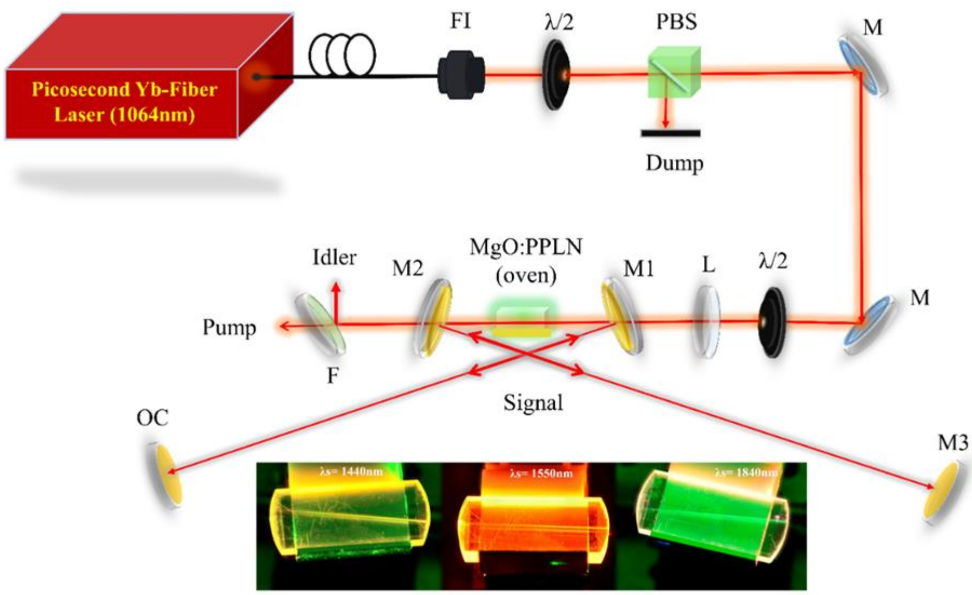

Figure 4.3: Schematic of the angle-tuned, synchronously pumped picosecond optical parametric oscillator based on MgO:PPLN. FI: Faraday isolator, λ/2: Half-wave-plate, PBS: Polarizing beam-splitter, M: Mirrors, L: Lens, OC: Output coupler. Inset: MgO:PPLN crystal tuned to three different angles during the OPO operation.

a combination of a half-wave plate and a polarizing beam-splitter cube. A second half-wave plate is used to obtain the required polarization for phase-matching in the crystals.

There are many ways to design an OPO, depending on whether it is CW, ns pulsed, or ultrafast. Here, the pump source is a picosecond Yb-fiber laser corresponding to the ultrafast regime. Due to the narrow temporal window of the pump pulses in this case to allow a sufficient number of round-trips for the build up of the parametric waves over the pump envelope, operation of this type of OPOs is attainable only under synchronous pumping conditions. In addition, taking into consideration of stability and tuning, the OPO system is finally configured in a standing-wave X-cavity with two plano-concave mirrors, M1,2 of radius of curvature, *r*=200 mm, a plane mirror, M4, and a plane output coupler, OC. Here, all mirrors, M1-3 are antireflection (AR)-coated for high transmission (*T*>90%) at 1064 nm for the pump, (*T*>80%) over 2.2-4 μm for the idler and high reflectivity (*R*>99%) over 1.3-1.9 μm for the signal, ensuring singly resonant signal oscillation. A conventional plane OC with partial transmission (*T*~10%) over 1100-1630 nm is used to extract the signal power from the OPO and a dichroic mirror, M4, separates the generated idler from the pump. The total optical length of the OPO cavity is~375 cm, corresponding to a repetition rate of 80 MHz, ensuring synchronization with the pump laser.

For the wavelengths of interest we chose MgO:PPLN as nonlinear optical crystal, because it has a large nonlinear coefficient, broad transmission range from 0.4 μm to 4.0 μm, and higher damage threshold. We now consider wavelength tuning at room temperature and under noncritical phase matching. As mentioned earlier, when working with periodically poled crystal, the best way to achieve a wide and continuous tuning is to utilize this periodically poled crystal cut as a cylinder, polished on its cylindrical side and exhibiting a single grating period, Λ_0, as shown in Fig. 4.2. In this situation, the effective grating period of the crystal is described by:

$$\Lambda_{eff}(\theta) = \Lambda_0/cos(\theta) \qquad (4.1-1)$$

Where θ is the angle between propagation direction and grating direction. According to the phase matching condition, we can obtain the following scalar equation:

$$\frac{n_3}{\lambda_3} - \frac{n_2}{\lambda_2} - \frac{n_1}{\lambda_1} - \frac{1}{\Lambda(\theta)} = 0 \qquad (4.1-2)$$

Clearly, when rotating the cylinder around its revolution axis by an angle, θ, the signal and idler wavelength can vary continuously. In our experiment we used a 35-mm-long 5% MgO:PPLN, with an aperture of 15×5 mm^2 and a grating period Λ_0=28 µm. The total angular aperture of the crystal is 45°, which is more than the required aperture of 30° for tuning the OPO. The end faces of the MgO:PPLN crystal are carefully grinded and polished, resulting in a partial cylinder, enabling a total angular interrogation of 30° with respect to the poled grating period. Further, the end faces are AR-coated for high transmission (R<4%) for the pump, (R<2%) for the signal over 1300-1900 nm. The AR coatings on the crystal for the idler wavelength range vary from R<1% at 2000 nm to as much as R<10% at 2500 nm, and slowly decrease down to R<7% at 4000 nm. This MgO:PPLN cylinder enables type-0 (e→e+e) phase-matching for 1064 nm pumping at room temperature. Hence, unlike the traditional MgO:PPLN OPOs, which are generally temperature tuned, this OPO provides similarly wide tunability, but at room temperature.

4.3 Design and optimization of the cavity

To design the OPO cavity, we have to first optimize the focusing conditions, corresponding to optimize the *focusing parameter*:

$$\xi = \frac{l}{b_p} \qquad (4.1-3)$$

Here l is the length of the crystal and b_p is the *confocal parameter* of the pump defined as:

$$b_p = k w_{op}^2 \qquad (4.1-4)$$

Where k is the pump wave vector, w_{op} is the radius of beam waist of the pump laser inside the crystal. Boyd and Ashkin [89] have considered the problem of focusing in the near-field limit. The exact analysis of Boyd and Kleinman [90] shows that in the absence of double refraction, the maximum value of parametric gain, occurs for $\xi \approx 2.83$. Considering system performance and damage issues, here the pump beam waist used in this experiments is $w_0 \sim 48$ µm at the center of the MgO:PPLN crystal positioned in between M1 and M2, corresponding to a confocal focusing parameter, $\xi \sim 1.2$. The signal spot size was adjusted by translation of the SRO cavity mirrors, M1 and M2, to yield a confocal parameter $b_p = b_s$ (b_s is the confocal parameter at signal wavelength), resulting in a waist radius of $w_{os} \sim 59$ µm.

4.4 Results and discussions

4.4.1 Angle tuning

In order to characterize the OPO, we initially performed tuning measurements. Wavelength tuning was achieved by changing the angle of the MgO:PPLN crystal. While keeping the direction of the pump beam fixed, changing the angle of the MgO:PPLN crystal from 0º to 30º with respect to the grating period, resulted in a signal wavelength tuning from 1413 nm to 1900 nm (over 487 nm) together with the idler wavelength tuning from 2418 nm to 4307 nm (over 1889 nm), corresponding to a total signal plus idler tuning range of 2376 nm, as shown in Fig. 4.4.

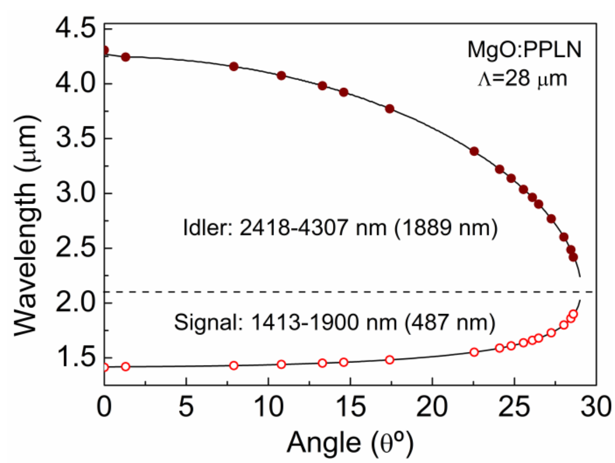

Figure 4.4: Wavelength tuning range of the Yb-fiber laser pumped, angle tuned MgO:PPLN SRO as a function of crystal angle at room temperature. Dots represent experimental data where as the line represents theoretical results.

Here, the filled and hollow circles represent the experimental data, while the solid curve represents the theoretical angle tuning curve for the MgO:PPLN crystal using the relevant Sellemier equations [78], confirming good agreement between the experimental and the theoretical data. Thus, the tuning was continuous over 1413−4307 nm, except a small gap close to degeneracy (1900−2418 nm) due to the reflectivity fall-off of OPO mirrors to prevent doubly-resonant oscillation. The limit to OPO tuning at the extremes of the signal and idler range was set by the maximum operating angle of the crystal. The signal wavelengths up to 1650 nm were directly measured using a spectrum analyzer, while wavelengths beyond 1650 nm up to the degeneracy were estimated from the non-phase-matched, parasitic second harmonic of the signal using a visible spectrometer. The idler wavelengths were then estimated from the energy conservation.

4.4.2 Temporal characterization

Further, we performed spectral and temporal characterization of the signal pulses from the angle-tuned MgO:PPLN picosecond OPO. The temporal characterization was performed using fringe-resolved intensity autocorrelation based on two-photon absorption in Si and GaAsP photo-detectors. Figure 4.5 shows the typical interferometric autocorrelation profile, indicating a Gaussian signal pulse duration of $\Delta\tau\sim15.2$ ps.

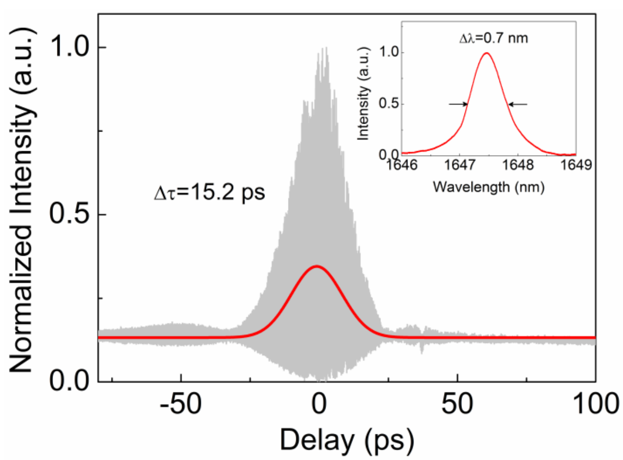

Figure 4.5: Interferometric autocorrelation of signal pulses extracted from the OPO. Inset: corresponding signal spectrum centered at 1647.5 nm.

Spectral measurements of the output signal pulses were performed using an optical spectrum analyzer. A representative signal spectrum with a FWHM bandwidth of 0.7 nm, centered at 1647.5 nm, is shown in the inset of Fig. 4.5. These measurements correspond to a time-bandwidth product $\Delta\upsilon\Delta\tau$~1.2, which is 4.5 times lower than $\Delta\upsilon\Delta\tau$~5.3 for the pump pulses, and <3 times greater than the transform limit, indicating good spectral and temporal characteristics of the OPO.

4.4.3 Power across tuning range

In Fig. 4.6, the extracted signal and idler power at different wavelengths are shown across the tuning range of the angle-tuned MgO:PPLN picosecond OPO. The high nonlinearity of MgO:PPLN and long interaction lengths enabled by QPM, in combination with the high peak power of ultrafast picosecond pulses, results in high conversion efficiency and low threshold of the OPO. However the overall extraction

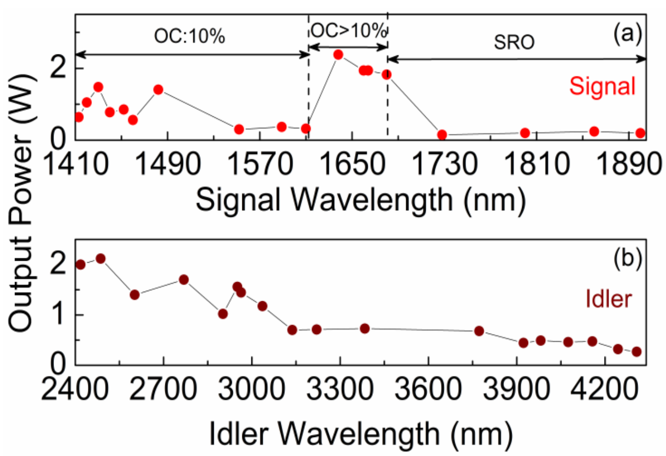

Figure 4.6: (a) Signal and (b) idler power across the tuning range of the angle tuned MgO:PPLN picosecond OPO.

efficiency of an OPO essentially depends on the amount of signal power that can be extracted from the oscillator. Hence, the choice of suitable output coupling is critical for optimum performance of the OPO. On the other hand, high-power picosecond OPOs based on MgO:PPLN can afford high output coupling losses of > 50%, providing extraction efficiencies as high as 57% [91]. Hence, due to the lack of a suitable output coupler along with the reduced AR-coating damage threshold due to the curvature on the faces of the crystal, we limited the pump power at the input to the OPO to 10 W, resulting in a maximum available pump power of ~8.5 W in the crystal. Under these conditions, we were able to extract signal powers less than 2 W in the wavelength range below 1630 nm. Since the transmission of OC increased significantly beyond 1630 nm, this resulted in a maximum signal power of 2.4 W at 1638 nm together with an idler power of 1.2 W at 3036 nm, corresponding to an overall extraction efficiency of ~42% , as shown in Fig. 4.6(a). For the signal wavelength range beyond 1700 nm, we replaced the OC with a high reflector, operating the OPO in pure singly-resonate configuration, where we were able to extract only hundreds of millwatts of signal power. The corresponding idler power is shown in Fig. 4.6(b), and varies from 1.4 W at 2418 nm down to 0.268 W at 4307 nm. The threshold of the OPO across the tuning range is less than 2 W and maximum pump depletion of >70% is recorded. It is to be noted that the data presented here are not corrected for any losses due to the AR coatings on the OPO mirrors, crystal and the separation mirror.

4.4.4 Power scaling

The power scaling results for the angle-tuned MgO:PPLN picosecond OPO are shown in Fig. 4.7. Using an OC~10%, the variation of the signal power at a wavelength of 1413 nm together with the simultaneously measured idler power at a mid-IR wavelength of 4175 nm, along with the pump depletion are shown in Fig. 4.7(a). For a maximum pump power of 8.6 W, we were able to extract up to 1.5 W of signal power together with 0.66 W of idler power, corresponding to a total power of 2.16 W at an overall extraction efficiency of ~25%, from the OPO. The signal and idler slope efficiencies are estimated to be 20% and 8%, respectively. The threshold of the OPO is ~1W, while pump depletion is recorded to be >54%. Also shown in Fig. 4.7(b) is a similar measurements at slightly longer signal wavelength of 1664 nm, resulting in an extracted signal power of 2.1 W at a slope efficiency of ~31%, together with an idler power of 1.7 W at a slope efficiency of ~25% at 2950 nm, for a maximum pump power of 8.5 W, corresponding to an overall extraction efficiency of ~45%. The threshold of the OPO in this case was ~1.3 W and a pump depletion >68% was recorded.

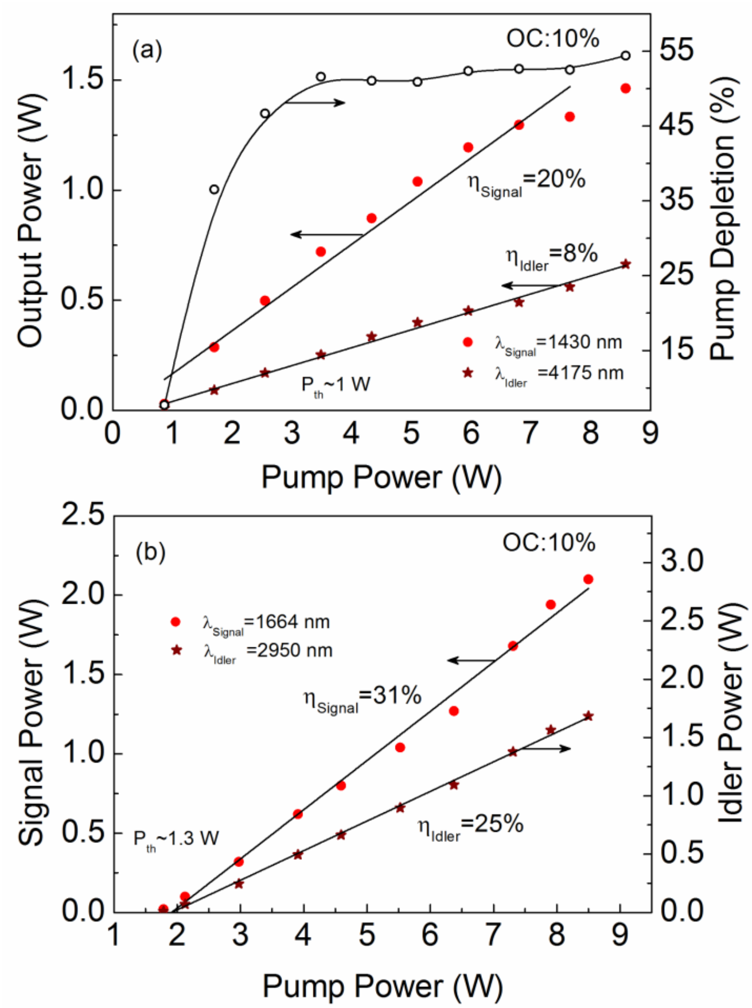

Figure 4.7: Output power scaling at a signal wavelength of (a) 1430 nm, and (b) 1664 nm using a10% output coupler.

4.4.5 Long-term power stability

The long-term power stability measurements of the extracted signal together with idler from the OPO as shown in Fig. 4. 8. Under free-running conditions and in the absence of thermal isolation, the signal power measured at a central wavelength of 1638 nm was recorded to exhibit a passive stability better than 1% rms over 15 hours. The corresponding idler power at 3036 nm exhibits a passive stability better than 0.8% rms. The slight long-term drift in the signal and idler power could be attributed to the cavity length changes over the duration of the measurements. In addition, the signal spectral stability at a central wavelength of 1644 nm was also recorded, as shown in the inset of Fig. 4.8, resulting in the standard deviation of the central frequency fluctuation of ~4.7 GHz, limited by the measurement, recorded over a period of 10 mins. The corresponding FWHM signal bandwidth varies by ±2.5% over the same measurement period.

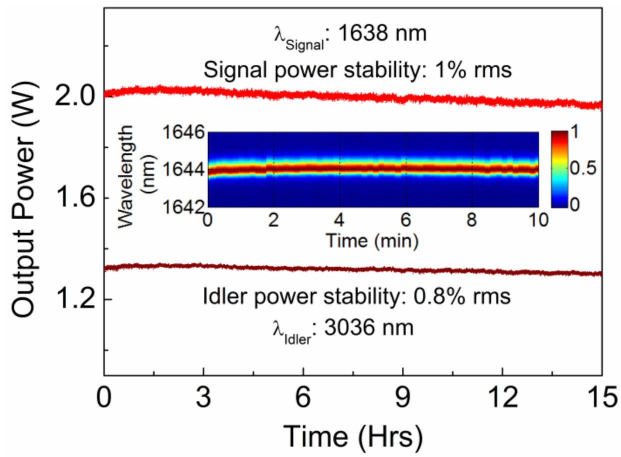

Figure 4.8: Long-term power stability of the extracted signal and idler from the angle-tuned MgO:PPLN picosecond OPO measured over 15 hours. Inset: Signal wavelength stability measured over a period of 10 minutes. The color scale in the inset represents the normalized spectral intensity.

4.4.6 Beam pointing stability

The beam pointing stability of the signal and idler from the angle-tuned MgO:PPLN picosecond OPO was also investigated. Using a scanning beam profiler and a CaF_2 lens of focal length, f=150 mm, we recorded the centroid position of the beam. As depicted in Fig. 4.9(a), the signal beam was recorded to exhibit a beam pointing stability <24 μrad in the X-direction and <30 μrad in the Y-direction at the maximum output power, while operating at a central wavelength of 1664 nm. The corresponding idler beam at 2950 nm exhibits a beam pointing stability <14 μrad in the X-direction and <8 μrad in the Y-direction, measured over a period of 1 hour.

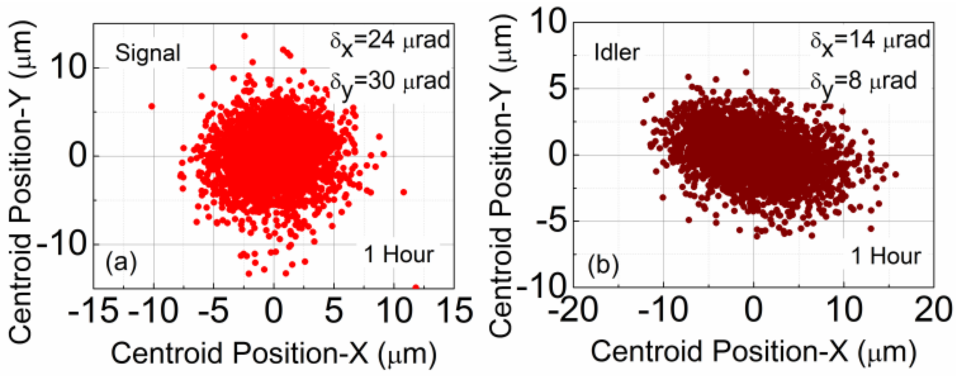

Figure 4.9: (a) Signal and (idler) beam pointing stability measured over 1 hour.

4.4.7 Far-field energy distribution

The far-field energy distribution of the signal beam measured at a wavelength of 1430 nm using a pyroelectric camera at a distance of <1 m from the OPO is shown in Fig. 4.10(a). The corresponding idler beam was collected using a CaF_2 lens, while the pyroelectric camera was scanned to have the required intensity. The idler beam profile recorded at a central wavelength of 4100 nm is shown in Fig. 4.10(b). The beam intensity profile along the two orthogonal axes appears to confirm both beams exhibit TEM_{00} mode profiles with single-peak Gaussian distribution.

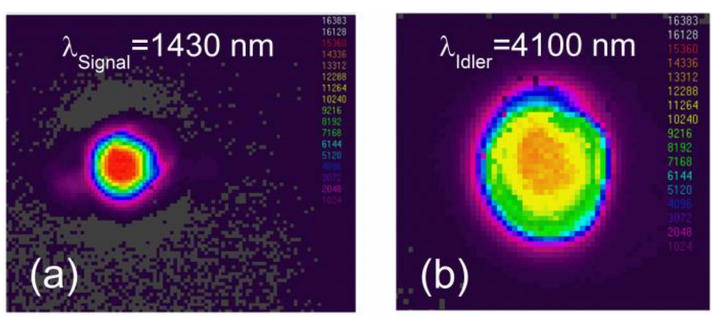

Figure 4.10: Beam profiles of the extracted (a) signal and (b) Idler from angle tuned MgO:PPLN picosecond OPO.

4.5 Conclusions

We demonstrated an angle-tuned MgO:PPLN picosecond OPO, synchronously pumped by a Yb-fiber laser, for the first time to the best of our knowledge. The OPO is tunable from 1413-1900 nm in the signal together with idler tunability from 2418-4307 nm, providing a total tunability of 2376 nm in the near-to-mid-IR region, simply by angular interrogation of the MgO:PPLN crystal at room temperature. Using a 10% output coupler, we were able to extract up to 2.4 W of signal at 1664 nm together with an idler power of 1.7 W at 2950 nm, corresponding to an overall extraction efficiency of ~45% with good beam pointing stability better than 30 μrad and 14 μrad for the signal and idler respectively. The generated signal and idler are recorded to exhibit passive power stability better than 1% rms and 0.8% rms over 15 hours at 1638 nm and 3036 nm, respectively, in good beam quality with TEM_{00} mode profile. Further, the spectral and temporal measurements performed on the signal pulses at ~1647 nm resulted in a Gaussian temporal width of 15.2 ps with a FWHM spectral bandwidth of 0.7 nm, corresponding to a time-bandwidth product $\Delta\upsilon\Delta\tau\sim1.2$. Further improvement in the AR-coatings for the signal and idler wavelength regions and optimization of the output coupling could lead to a higher extraction efficiency of the OPO. These results indicate the potential for rapid and wide tuning of high power OPOs as compared to the temperature tuned devices.

Chapter 5

Difference-Frequency-Generation in OP-GaP

This Chapter constitutes the following journal publications:

Junxiong Wei, S. Chaitanya Kumar, Hanyu Ye, Kavita Devi, Peter G. Schunemann, and M. Ebrahim-Zadeh, "Nanosecond difference-frequency generation in orientation-patterned gallium phosphide," Opt. Lett. 42, 2193-2196 (2017)

Junxiong Wei, S. Chaitanya Kumar, Hanyu Ye, P. G. Schunemann, and M. Ebrahim-Zadeh, "Performance characterization of mid-infrared difference-frequency-generation in orientation-patterned gallium phosphide," Opt. Mater. Express 8, 555-567 (2018)

5.1 Motivation

Coherent sources in the mid-infrared (mid-IR) spectral range are of great interest for a variety of scientific, industrial and medical applications [92,93]. Such applications continue to motivate the development of high-average-power mid-IR sources, particularly in the region of 2-10 μm. Numerous efforts have been directed towards the realization of such sources [94-96], with nonlinear optical techniques providing a particularly effective approach for practical generation of high-power and widely tunable mid-IR radiation. The advent of quasi-phase-matched (QPM) materials such as MgO-doped periodically-poled $LiNbO_3$ (MgO:PPLN) has heralded major breakthroughs in nonlinear frequency conversion technology. Today, optical parametric oscillators based on MgO:PPLN are firmly established as the most viable sources of widely tunable and high-power radiation in the 1-4 μm spectral range, limited by the onset of multi-phonon absorption in the material above ~4 μm [97]. Therefore, the development of nonlinear frequency conversion sources at longer wavelengths into the deep mid-IR, offering practical performance, and in simple design, has remained challenging. As a result, access to the deep-IR spectral range has been most effectively achieved by exploiting nonlinear frequency conversion techniques based on non-oxide-based nonlinear crystals of oreintation-patterened GaAs (OP-GaAs) or $ZnGeP_2$ (ZGP) offering a long-wavelength absorption edge well beyond 4 μm. On the other hand, the short-wavelength absorption edge in OP-GaAs and ZGP at ~2 μm preclude the direct deployment of well-established solid-state or Yb-fiber lasers at ~1.06 μm, thus necessitating the use of cascaded OPO pumping based on oxides in the first stage [31], direct OPO pumping using Tm/Ho-doped solid-state lasers [32], or difference-frequency-generation (DFG) between Tm-fiber laser and OPO [30]. The choice of suitable materials offering the required linear and nonlinear optical properties, in addition to the short-wavelength transparency cut-off, are clearly key factors for practical and efficient frequency conversion. The efficiency of the frequency conversion process depends critically on several material parameters, including effective nonlinear coefficient (d_{eff}), type of interaction and polarization of the incident fields, as well as temperature and spectral phase-matching properties.

Orientation-patterned gallium phosphide (OP-GaP) is the most recently developed non-oxide QPM semiconductor optical crystal, offering promising linear and nonlinear properties for deep mid-IR generation. It can potentially overcome several limitations of the established nonlinear materials, such as $ZnGeP_2$ and OP-GaAs, which require pumping at wavelengths beyond ~2 μm [98]. OP-GaP exhibits higher thermal conductivity (110 W/m-K) and a larger bandgap (below ~1 μm), thus enabling near-IR to deep-IR generation by deploying well-established pump laser technology at ~1.06 μm [99]. However, during this early stage in the development of OP-GaP, several material properties still need to be studied and optimum growth parameters are yet to be established, in order to achieve the expected performance and realize the full potential of this crystal. Hence, it is imperative to perform detailed characterization of the linear and nonlinear optical properties of this material to evaluate its viability for nonlinear frequency conversion pumped at ~1.06 μm.

Over the past two years, there have been a number of reports on nonlinear frequency conversion in OP-GaP. These include a nanosecond OPO in doubly-resonant oscillator (DRO) configuration pumped at 1.064 μm, generating 4 mW of idler at 4624 nm and 15 mW of signal at 1324 nm at 10 kHz [72], as well as a nanosecond DRO pumped at 2.09 μm operating at a fixed idler wavelength of 5100 nm and a signal wavelength of 3540 nm, providing a total signal plus idler output power of 350 mW at 20 kHz [100]. Recently, we also demonstrated a tunable DFG source based on OP-GaP operating across 2548-2781 nm by mixing the input pulses from a Q-switched nanosecond Nd:YAG pump laser at 1.064 μm with the tunable signal from a MgO:PPLN pulsed OPO in a 40-mm-long crystal, providing up to ~14 mW of average output power at 80 kHz repetition rate [74]. In another report, we demonstrated an optical parametric generator (OPG) based on OP-GaP pumped directly by a Q-switched Nd:YAG laser at 1.064 μm [101]. The OPG was temperature-tuned across 1721-1850 nm in the signal and 2504-2787 nm in the idler, providing up to ~18 mW of the total average output power at 25 kHz repetition rate, with ~5 mW of the idler power. Further, in the picosecond pulse regime, we demonstrated a single-pass DFG source by mixing the output signal of a picosecond OPO and ~20 ps pump pulses from a mode-locked Yb-fiber laser at 1.064 μm in OP-GaP, providing tunable DFG output across 3040-3132 nm with up to 57 mW of average power at 80 MHz repetition rate [102]. On the other hand, in the continuous-wave (cw) regime, single-pass DFG based on 16.5-mm-long OP-GaP crystal was reported, providing up to 150 mW of output power at a fixed wavelength of 3400 nm for an input pump power of 47 W at 1.064 μm, together with 24 W of signal power at 1550 nm [73]. Recently, using a 24.6-mm-long-OP-GaP crystal, a cw DFG power of 65 μW was generated at a fixed wavelength of 5850 nm for a pump power of 10 W at 1.064 μm and a signal power of 40 mW at 1301 nm [103].

In this work, we report a systematic performance characterization of tunable single-pass mid-IR DFG in OP-GaP, for the first time. Using a 40-mm-long OP-GaP crystal, we have investigated several important parameters including parasitic wavelength generation, mid-IR DFG tuning, power scaling, temperature as well as spectral acceptance bandwidths. We have also studied the dependence of DFG power on the polarization of the incident fields, performed transmission measurements at the pump and signal wavelength, and investigated thermal effects and damage threshold limitation of the OP-GaP sample.

5.2 Experimental setup

The schematic of the experimental setup is shown in Fig. 5.1. The DFG source basically consists of the pump and signal laser and a OP-GaP crystal. The phase-matching condition is met by controlling the temperature of the OP-GaP crystal.

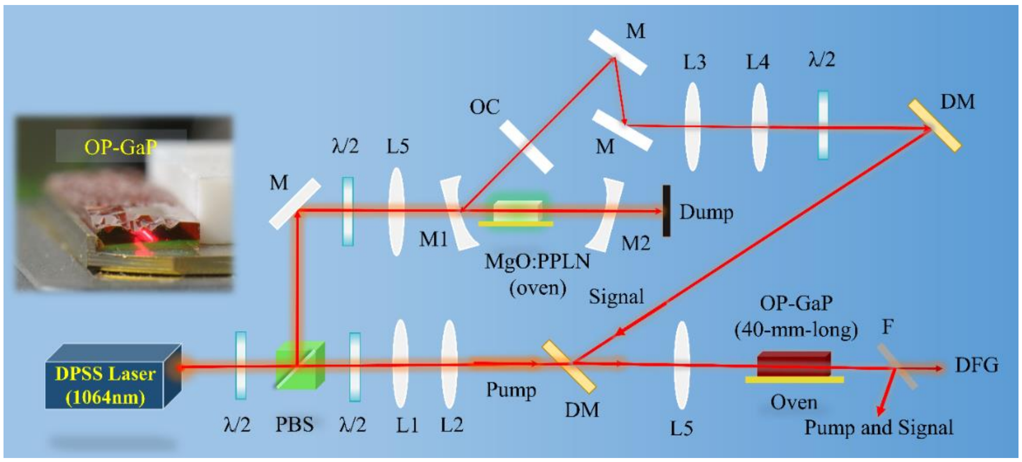

Figure 5.1: Schematic of the experimental setup. HWP: Half-wave-plate, PBS: Polarizing beam-splitter, DM: dichroic mirror, OC: Output-coupling, M: Mirrors, L: Lens, F: Germanium filter, S: signal beam, P: pump beam.

Pump and Signal Source: The input pump is a Q-switched Nd:YAG laser (Bright Solutions, Sol), delivering up to 30 W of average power at ~1064 nm in linear polarization, with a tunable repetition rate of 20-100 kHz. The output pulse duration varies from ~8 ns at 20 kHz to ~26 ns at 100 kHz repetition rate. However, for the experiments presented in this report, we used a repetition rate of 80 kHz, resulting in a FWHM pump pulse duration of ~23 ns. The instantaneous FWHM bandwidth and frequency jitter of this laser are measured to be <0.5 nm and ∼1 nm over 0.5 minutes, respectively. A major portion of the output power from the laser is used to pump a pulsed OPO, which provides the input signal beam for DFG in the OP-GaP crystal, while the remaining power is used as the pump for the DFG process.

Nonlinear Gain Medium: The nonlinear crystal for the pulsed OPO is a 38-mm-long, 1-mm-thick MgO:PPLN crystal, with five grating periods ranging from Λ_{OPO}=29.5 to 31.5 µm in steps of 0.5 µm. However, in the present experiments, we used a single grating period of Λ_{OPO}=31.5 µm. The end faces of the crystal are antireflection (AR)-coated for the pump and idler (*R*<4%), with high transmission (*R*<1%) for the signal over 1300-1900 nm. The crystal is housed in an oven, which can be adjusted from room temperature to 200 ^{o}C, with a stability of ±0.1 ^{o}C. The OPO is configured as a singly-resonant oscillator for the signal in a three-mirror cavity arrangement. In order to partially extract the signal from the OPO, we use a ~22% output coupler, while the idler is extracted in single-pass through the cavity and filtered from the pump. For the fixed grating period of Λ_{OPO}=31.5 µm, the OPO can be temperature-tuned over 1664-1928 nm in the signal and 2374-2950 nm in the idler. The signal from the OPO and the remaining pump from the laser are collimated and combined using a dichroic mirror, which is coated for high reflectivity (*R*>99%) for the signal over 1300-2000 nm and high transmission (*T*>90%) for the pump at 1064 nm. The nonlinear crystal for DFG is a 40-mm-long OP-GaP sample, which is 6-mm-wide, 1.7-mm-thick, and contains a single grating period of Λ_{DFG}=15.5 µm. The crystal end-faces are AR-coated for high transmission (R<1%) at 1064 nm and 1500-1900 nm, with >80% transmission over 2500-2800 nm.

Focusing condition: The pump and signal beams are focused to waist radius of w_{op}~65 µm and w_{os}~60 µm, respectively, at the center of the OP-GaP crystal. These focal spots correspond to focusing parameter of ξ_p~0.5 and ξ_s~1 for the pump and signal, respectively. The resulting DFG beam waist in the OP-GaP crystal is estimated to be w_{oi}~44 µm, with a corresponding focusing parameter of ξ_i~2.6. The DFG output is extracted after separation from the pump and signal using a Ge filter, and measured using a power meter.

5.3 Results and discussion

5.3.1 Parasitic processes

Orientation-patterned gallium phosphide (OP-GaP) is a relatively new nonlinear material with a nominally high nonlinearity of d_{eff}~50 pm/V. However, due to the significant optical losses at the pump, signal and DFG wavelengths, together with the non-uniformity in the OP-GaP grating period, it is challenging to establish the ideal operating point during device development. Hence, parasitic wavelengths can be used to initially to identify the frequency conversion process, which can in turn be used to optimize the device performance.

Initially, with the input pump beam incident on the OP-GaP sample, we observed weak green light generation through non-phase-matched frequency doubling of the pump light. By careful alignment of both pump and signal beams through the crystal, a parasitic output beam in the red could also be observed.

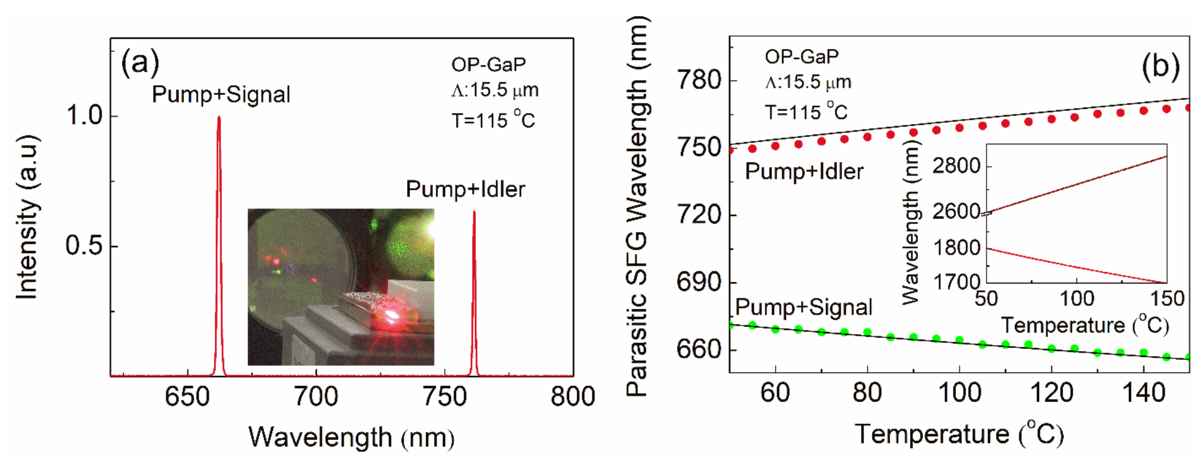

Figure 5.2: (a) Spectrum of the generated parasitic SFG at 664.6 nm (pump+signal) and at 761.4 nm (pump+DFG). Inset: 40-mm-long OP-GaP sample generating red parasitic output beam at the exit of the crystal. (b) Variation of the parasitic SFG wavelengths as a function of OP-GaP crystal temperature. Inset: Corresponding DFG temperature tuning.

A typical spectrum of the parasitic red light at 664.6 nm, measured using a visible spectrometer (Ocean Optics, HR4000), obtained at an OP-GaP crystal temperature of 115 ºC, is shown in Fig. 5.2(a). The measured spectrum corresponds to higher-order QPM sum-frequency-generation (SFG) of the pump at 1064 nm and signal at 1770 nm. We also detected another parasitic component at 761.4 nm resulting from SFG between the DFG output and the pump, as can also be seen in Fig. 5.2(a), as well as a weak frequency doubling of the signal beam at 885 nm. The total average power in the parasitic components was measured to be <1 mW, compared to the DFG output power of ~14 mW. Also shown in the inset of Fig. 5.2(a) is the parasitic SFG output in the red produced by the 40-mm-long OP-GaP crystal during the DFG process. We estimated the QPM grating periods required to generate the parasitic light using the relevant temperature-dependent Sellmeier equations [72]. The calculation resulted in a grating period of Λ_{SFG}~3.4 µm for the SFG between pump and signal, Λ_{SFG}~6.2 µm for the SFG between the pump and DFG output. The DFG tuning was achieved by simultaneously varying the OPO signal wavelength and the phase-matching temperature of the OP-GaP crystal. The corresponding parasitic wavelength tuning as a function of the OP-GaP crystal temperature is shown in Fig. 5.2 (b). For a fixed pump wavelength of 1064 nm, varying the signal wavelength across 1723-1827 nm together with OP-GaP crystal temperature over 50-150 ºC, resulted in a parasitic SFG tuning over 658-672 nm (pump+signal) and 770-753 nm (pump+DFG). The filled circles in Fig. 5.2(b) correspond to the measured parasitic SFG wavelength data. The solid lines are theoretical calculations using the relevant Sellmeier equations for OP-GaP [72]. In the calculations, the value of the OP-GaP grating period was optimized to Λ=15.56 µm, in order to obtain the best match to the experimentally measured SFG wavelengths. From the measured SFG data, we deduced an experimental DFG tuning range from 2548 to 2781 nm (233 nm), while the theoretical DFG tuning range was calculated to be from 2492 to 2782 nm (290 nm), as presented in the inset of Fig. 5.2(b). Hence, there is good agreement between the experimental tuning range deduced from the parasitic SFG tuning data and theoretical tuning range based on a grating period of Λ=15.56 µm. Across the DFG tuning range, we generated >6 mW of average output power.

5.3.2 Temperature acceptance bandwidth

In order to study the phase-matching properties of the 40-mm-long OP-GaP crystal for the DFG process, we performed temperature acceptance bandwidth measurements. We used the same focusing condition as for DFG, with w_{op}~65 µm and w_{os}~60 µm, corresponding to focusing parameter of ξ_p~0.5 and ξ_s~1 for the pump and signal, respectively, at the center of the OP-GaP crystal. For this measurement, the pump and signal powers were maintained constant at 3 W and 0.6 W, respectively. For a pump wavelength of 1064 nm and a fixed signal wavelength of 1766 nm, generating a DFG wavelength of 2676 nm, the normalized DFG power as a function of the temperature deviation about the phase-matching temperature is shown in Fig. 5.3(a). Also shown is the *sinc*^{2} fit to the experimental data, resulting in a full-width at half-maximum (FWHM) temperature acceptance bandwidth of ΔT~18 ºC, centered at ~103 ºC. The theoretically calculated temperature acceptance bandwidth for a 40-mm-long OP-GaP crystal with a grating period of Λ=15.56 µm, using the temperature-dependent Sellmeier equations [72], is shown in Fig. 5.3(b). As can be seen, the experimentally measured bandwidth is substantially larger than the theoretical FWHM value of ΔT~1 ºC.

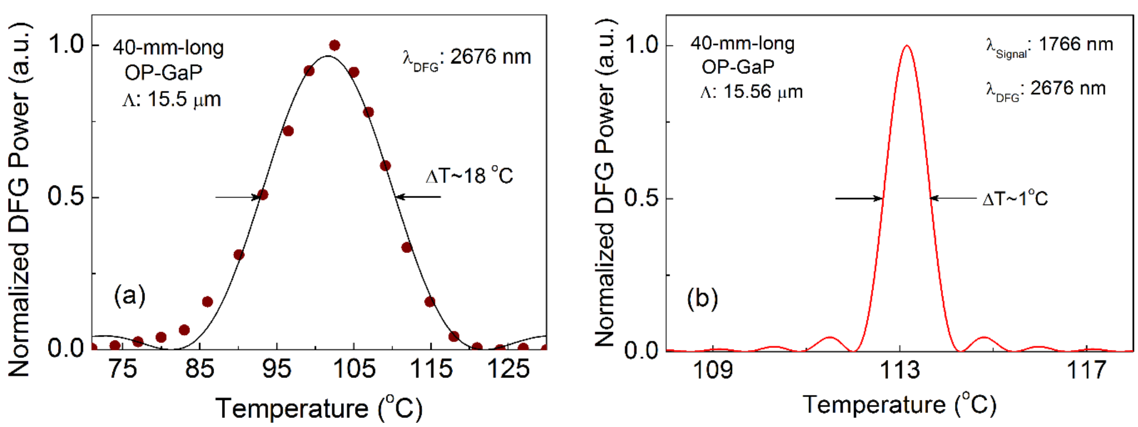

Figure 5.3: (a) Experimentally measured temperature acceptance and the corresponding *sinc*^{2} fit, and (b) theoretically calculated temperature acceptance bandwidth, for the 40-mm-long OP-GaP crystal.

It is also to be noted that the theoretically calculated phase-matching temperature of ~113.2 ºC is significantly different from the measured value of 103.3 ºC. However, it is closer to the measured experimental value than the estimated value for an OP-GaP crystal with a grating period of Λ=15.5 µm, which is calculated to be 124.4 ºC. The large discrepancy in the phase-matching temperature and acceptance bandwidth could be attributed to the uncertainty in the grating period, wide spectral bandwidth of pump and signal beams, as well as thermal effects due to absorption in the crystal. In addition, the calculation of acceptance bandwidth is based on plane-wave approximation, while the experimental measurements correspond to focused beams, which were necessary, given the restricted useful aperture of the grating region and the limited DFG efficiency due to crystal absorption (see Section 8).

5.3.3 Spectral acceptance bandwidth

We further investigated the spectral acceptance bandwidth of the 40-mm-long OP-GaP crystal. The normalized DFG power as a function of the signal wavelength, for a fixed pump wavelength, is shown in Fig. 5.4(a).

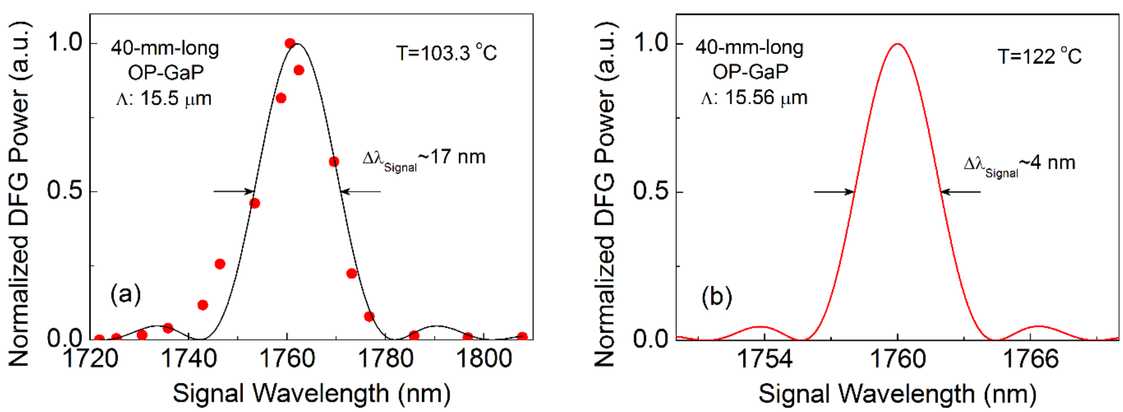

Figure 5.4: (a) Experimentally measured spectral acceptance and the corresponding sinc2 fit, and (b) theoretically calculated spectral acceptance bandwidth for the 40-mm-long OP-GaP crystal.

For this measurement, the phase-matching temperature was optimized for every signal wavelength to achieve maximum DFG power. Also shown in Fig. 5.4(a) is the *sinc*^{2} fit to the experimental data, resulting in a FWHM acceptance bandwidth of $\Delta\lambda_{signal}$ ~17 nm. This is also much wider than the theoretically estimated spectral acceptance bandwidth of $\Delta\lambda_{signal}$ ~4 nm for a 40-mm-long OP-

GaP crystal at wavelength of 1760 nm using the temperature-dependent Sellmeier equations for the material [72]. It is also to be noted that the theoretically calculated phase-matching temperature for an OP-GaP grating period of Λ=15.5 µm is ~129 ºC, which is much higher than the measured experimental value 103.3 ºC. On the other hand, the phase-matching temperature calculated for the grating period of Λ=15.56 µm is 122 ºC, as shown in Fig. 5.4(b), indicating that the difference in the phase-matching temperature is caused by the uncertainty in the grating period. Other factors contributing to the discrepancy include additional thermal effects due to crystal absorption and broad bandwidth of the input pump and signal pulses used in the DFG experiment.

5.3.4 Polarization dependence and optimization

Gallium phosphide is a cubic nonlinear material, and due to the high symmetry, birefringent phase-matching is not available, so that all nonlinear optical processes are achieved by QPM interaction through orientation-patterning [72]. As a result, several different polarization combinations can provide access to nonlinearity. As such, both linear and circularly polarized light have been used to realize nonlinear frequency conversion in OP-GaP [73]. However, in order to achieve maximum conversion efficiency in OP-GaP, the pump and signal beams should be linearly polarized. Hence, it is important to optimize the polarization of the incident input beams independently, thereby accessing the maximum nonlinear gain coefficient in the crystal. The polarization-dependent gain factor, δ^2, which is defined as the ratio of the effective nonlinear coefficient to d_{14} for linearly polarized incident beams in OP-GaP is given by [73]:

$$\delta^2 = \left(\frac{d_{eff}}{d_{14}}\right)^2 = sin^2(\psi_p + \psi_s) + sin^2\psi_p sin^2\psi_s \qquad (5.3-1)$$

Here, ψ_p and ψ_s represent the angle between the pump and signal polarization vectors relative to the [100] plane in the OP-GaP crystal, respectively.

The variation of the gain factor, δ^2, as a function of pump and signal polarizations is shown in the Fig. 5.5(a). As can be seen, for a pump polarization parallel to the [100] plane (ψ_p=0º), the gain factor varies sinusoidally as a function of signal polarization, (ψ_s), reaching maximum of δ^2=1. However, for the pump polarization perpendicular to the [100] plane (ψ_p=90º), δ^2 remains constant at unity, accessing a nonlinear coefficient of d_{14}, irrespective of the signal polarization (ψ_s). However, a maximum nonlinear coefficient of 1.3 times d_{14} can be achieved by arranging both the pump and signal polarization directions along the base diagonal (ψ_p=ψ_s=54.7º) in the first quadrant. Other ($\psi_{p,s}$) combinations resulting in maximum δ^2=1.3d_{14} also exist in the second, third, and fourth quadrant. Figure 5.5(b) further illustrates the maximum and minimum values of the gain factor that can be achieved for different pump polarizations, while scanning the signal polarization. It can be seen that frequency conversion can always be realized with a non-zero value of δ^2, for any ψ_s with ψ_p>0º.

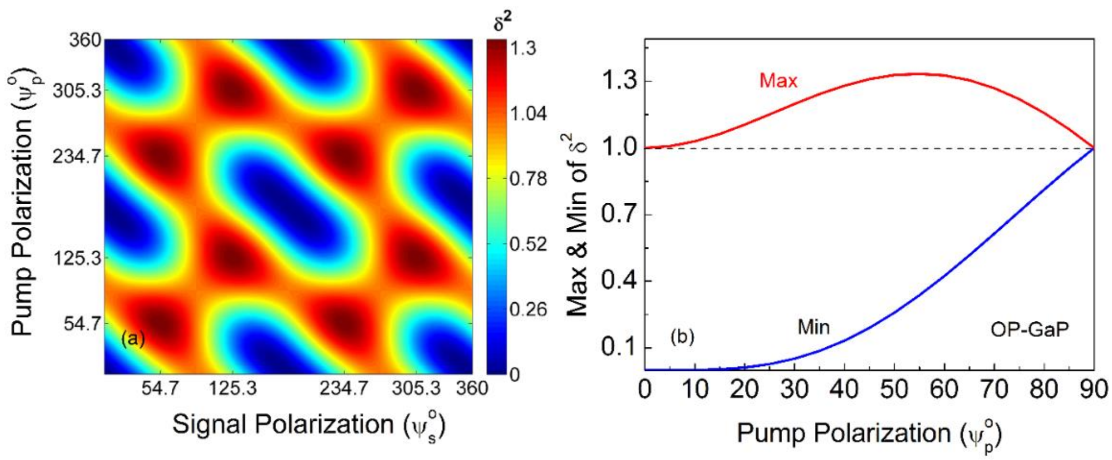

Figure 5.5: (a) Variation of the nonlinear gain factor (δ^2) as function of the pump and signal polarization in OP-GaP. (b) Variation of the maximum and minimum values of the gain factor for different pump polarizations in the first quadrant.

In order to study the dependence of the frequency conversion process on the incident beam polarizations in OP-GaP, we measured the DFG output power, which is proportional to δ^2, for three different pump polarizations, while varying the input signal polarization. The results are presented in Fig. 5.6(a-c).

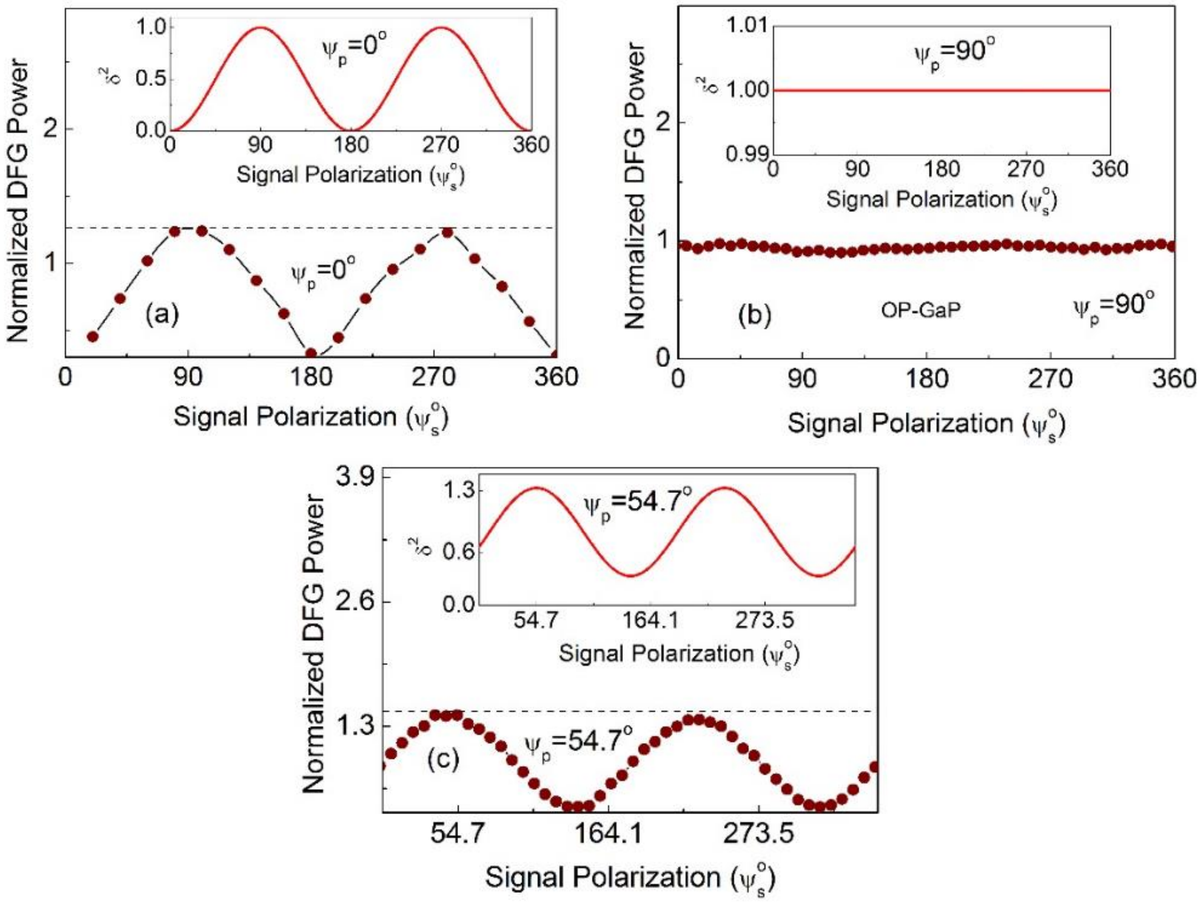

Figure 5.6: Variation of the normalized DFG output power as a function of signal polarization, ψs, for a fixed pump polarization of (a) ψ_p=0º, (b) ψ_p=90º, (c) ψ_p=54.7º. Inset: Corresponding theoretical calculations.

Two independent half-wave plates were used to vary the pump and signal polarizations and the measured DFG power was normalized with respect to that for ψ_p=90º (δ^2=1). The corresponding theoretical calculations showing the variation of δ^2 as a function of signal polarization (ψ_s) for the three different pump polarizations (ψ_p) are also presented in the insets of Fig. 5.6(a-c). For a fixed pump polarization of ψ_p=0º, with a constant power of 3 W at 1064 nm and a signal power of 0.6 W at 1748 nm, the variation of the normalized DFG power as a function of signal polarization is shown in Fig. 5.6(a). As predicted, the normalized DFG power varies sinusoidally with signal polarization, with a minimum at ψ_s=0º, while reaching a maximum of ~1.2 at ψ_s=90º, which is close to the theoretical value of 1. Similar measurements for the orthogonal pump polarization of ψ_p=90º resulted in a constant output as a function of signal polarization, as shown in Fig. 5.6(b), as expected. Moreover, as evident from Fig. 5.6(c), when the pump polarization is fixed at ψ_p~54.7º, the normalized DFG power again varies sinusoidally, reaching a maximum of ~1.4 for a signal polarization of ψ_s~54.7º. This value is again close the theoretically predicted value of 1.3.

5.3.5 Power scaling

We also performed power scaling measurements by recording the variation of DFG output power as a function of input pump power for two different pump polarization angles of ψ_p=54.7º and ψ_p=90º, with the results shown in Fig. 5.7. The signal average power was fixed at 1 W, while operating at 1748 nm, resulting in a DFG wavelength of 2719 nm. For each pump polarization, the signal polarization was optimized to achieve maximum DFG ouptut power. As evident from Fig. 5.7, the DFG power increases linearly as function of pump power, generating as much as 14 mW (ψ_p=54.7º) and 9 mW (ψ_p=90º) for a maximum pump power of 5 W, resulting in a DFG power ratio of ~1.5 for the two pump polarizations, slightly higher than the expected values of 1.3. The corresponding slope efficiencies are estimated to be 0.3% and 0.15%, respectively. The discrepancy in the attainable maximum power could be attributed to inhomogeneity in the transmission leading to absorption in our OP-GaP crystal at the pump, signal and DFG wavelengths, which are in turn dependent on polarization and temperature, as discussed in Sec. 8. While performing the power scaling measurements, the temperature of OP-GaP crystal was optimized for each pump power to achieve the maximum DFG output power. As the pump power was increased from the 0.6 W to 5 W, the phase-matching temperature of the OP-GaP had to be reduced by ~30 ºC, indicating strong thermal effects. This change in temperature is much wider than the measured temperature acceptance bandwidth of 18 ºC presented in Fig. 5.3, and can be attributed to the absorption at the pump and signal wavelengths, resulting in the temperature rise in the OP-GaP crystal, thereby necessitating the reduction of the phase-matching temperature. We measured the transmission for the pump and signal beams, while producing the maximum DFG power of 14 mW, and found them to be 28% and 18%, respectively. Taking into account the losses in the OP-GaP crystal, the generated maximum DFG power represents a pump-to-DFG conversion efficiency of ~1%, corresponding to a photon conversion efficiency of ~2.5%.

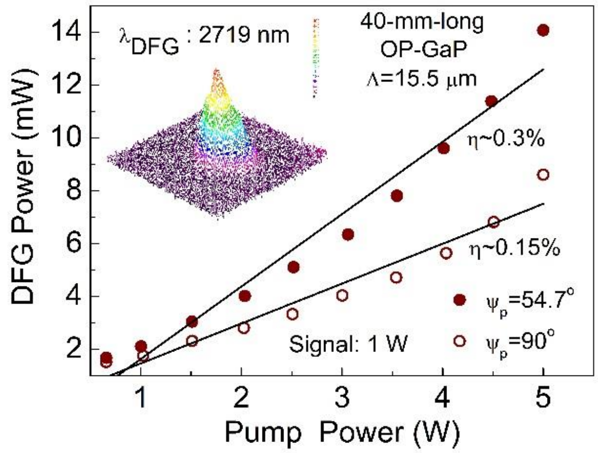

Figure 5.7: DFG power scaling as a function of the pump power at a constant signal power for two different pump polarizations of ψp=54.7º and ψp=90º. Inset: Spatial beam profile of the DFG beam at maximum power.

5.3.6 Transmission

In order to study thermal effects in the OP-GaP crystal during the DFG process, we performed transmission measurements at the pump and signal wavelengths. The results are shown in Fig. 5.8(a,b). While generating the maximum DFG power at 2719 nm, with the crystal near room temperature (T~28 ºC), we measured a transmission of 28% at the pump wavelength of 1064 nm and 18% at a signal wavelength of 1748 nm. Similar measurements at a different position in the OP-GaP crystal are presented in the inset of Fig. 5.8(a,b), showing higher transmission of 36% and 31% for the pump and signal, respectively, without significant improvement in the DFG output power. This indicates inhomogeneous transmission through the crystal and non-uniformity in the grating period. We also observed that the transmission of the crystal was dependent on the operating temperature, as reported previously [101,104].

To gain further insight, we also investigated the transmission of the OP-GaP crystal at 1064 nm under irradiation in other time-scales, by deploying a continuous-wave (CW) as well as a high-repetition-rate picosecond Yb-fiber laser at 80 MHz, in addition to the nanosecond pulses. During the systematic characterization, we ensured the use of the same position in the crystal and an identical maximum average pump power of 5 W for all the measurements. The laser beam in all three cases was also focused to a beam waist radius of w_{op}~90 µm inside the crystal.

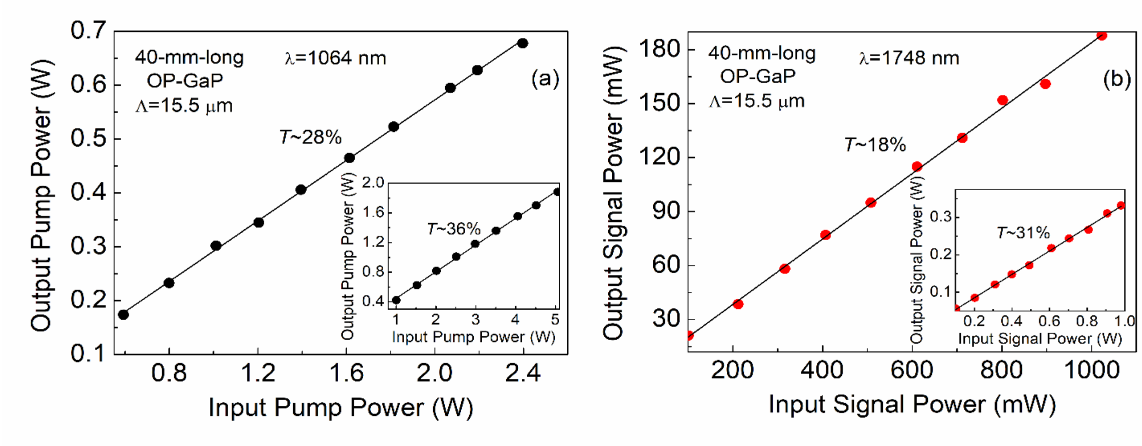

Figure 5.8: Transmission measurements of the 40-mm-long OP-GaP crystal at room temperature for (a) pump and (b) signal wavelengths, while generation a maximum DFG power at 2719 nm. Inset: Similar measurements at a different position in the crystal.

The measured transmission of the crystal as a function of temperature for the two orthogonal pump polarizations at 1064 nm is as shown in Fig. 5.9(a-c). As evident, the transmission is observed to decrease significantly with increase in temperature in the cw as well as nanosecond time-scale, while it is recorded to increase in the picosecond regime. We do not currently have an explanation for this behavior, and further studies are necessary to identify the underlying mechanisms responsible for the transmission properties of the OP-GaP crystal under irradiation in different time-scales. During these transmission measurements, we also observed a shift in the pump beam as a function of polarization, as presented in Fig. 5.10. In this case, the nanosecond pump beam was focused using a *f*=250 mm focal length lens in the OP-GaP crystal and the transmitted beam was monitored at distance of 18 cm from the exit face of the crystal using a beam profiler. As the pump beam polarization was varied from ψ_p=0 to 90º, the transmitted beam was observed to shift by ~1 mm in the vertical plane. This polarization-dependent beam walkoff could be attributed to stress-induced birefringence during the growth process of the OP-GaP crystal [105]. All these measurements indicate the poor quality of this first 40-mm-long OP-GaP crystal sample used in our experiments in terms of the transmission and grating uniformity.

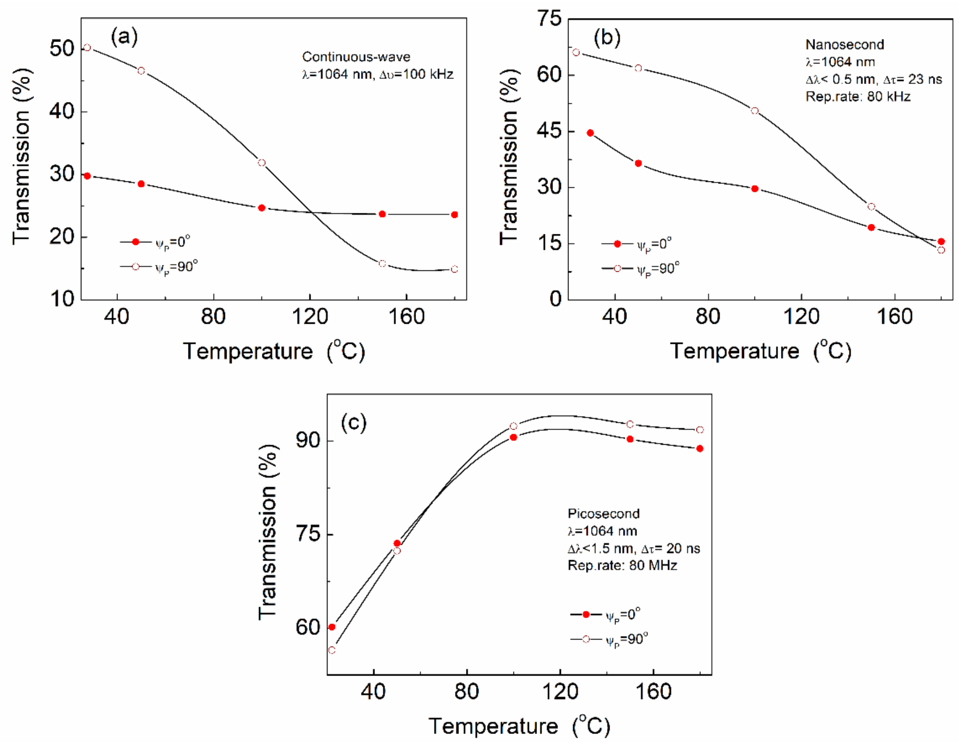

Figure 5.9: Transmission of the 40-mm-long OP-GaP crystal at 1064 nm in (a) continuous-wave, (b) nanosecond, and (c) high-repetition-rate picosecond time-scale, for the two orthogonal pump polarizations.

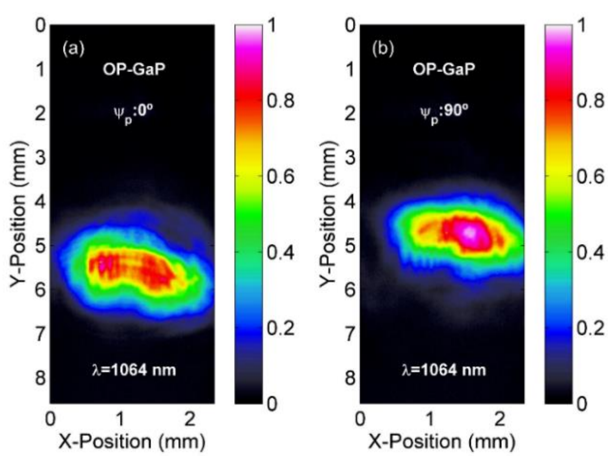

Figure 5.10: The shift in the spatial position of the pump beam at 1064 nm as function of polarization. (a) ψ_p=0º, (b) ψ_p=90º.

5.3.7 Thermal effects

The low transmission at the pump and signal wavelengths immediately suggests significant thermal effects in the OP-GaP crystal. Hence, we performed systematic measurements to estimate the temperature rise on the surface of the crystal using a point-contact thermocouple. As the pump power at the input to the OP-GaP crystal was increased to a maximum of 5 W, with no input signal, we measured a temperature rise as high as ~17 ºC. However, when the incident signal power was increased to 1 W, with no input pump, the temperature rise was recorded to be only about 4.5 ºC. On the other hand, while generating the maximum DFG power of 14 mW, with 5 W of pump and 1 W signal power at the input to the OP-GaP crystal, the temperature rise on the surface of the crystal was as high as ~20 ºC. Further, we observed that the time required to reach the maximum DFG power was longer for an incident pump power of 5 W with fixed input signal power, than that required when the pump power was fixed with an incident signal power of 1 W. When the signal power was fixed, the crystal reached a steady-state temperature, and releasing the pump power led to a large temperature rise. Hence, the crystal required longer time to reach the final steady-state phase-matching temperature. These measurements indicate that the absorption at the pump wavelength is much more significant than at the signal and DFG wavelengths.

5.3.8 Damage Limitations

The high absorption at the pump wavelength could eventually lead to damage in the OP-GaP crystal. Hence, we also attempted to characterize the OP-GaP crystal for damage at the 1064 nm. The pump beam was focused to a waist radius of w_{op}~75 µm inside the crystal. The maximum tolerable average power before the observation of bulk damage in the OP-GaP crystal, and the corresponding peak pulse intensity, as function of the pump laser repetition rate, are shown in Fig. 5.11(a). As can be seen, the maximum power before the crystal experiences damage increases linearly from 1.8 W at 20 kHz to 12 W at 80 kHz. It is to be noted that the pulse duration also varies from 8 ns at 20 kHz to 23 ns at 80 kHz, which is also accounted for in the calculated peak-intensity.

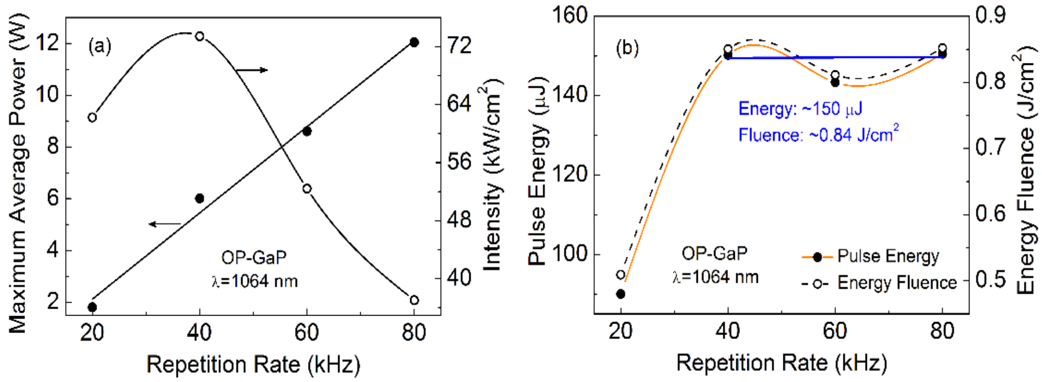

Figure 5.11: (a) Maximum tolerable average pump power before damage in the OP-GaP crystal, and the corresponding intensity, (b) pulse energy and fluence, as a function of the pump laser repetition rate at 1064 nm.

The variation of the corresponding pulse energy and the fluence is shown in Fig. 5.11(b), where it can be seen that at repetition rates >40 kHz, the pulse energy fluence is clearly the limiting factor, resulting in a damage threshold of ~0.84 J/cm^2. However, at lower repetition rates <20 kHz, the damage is observed to occur at a peak intensity of 62 kW/cm^2, corresponding to an energy fluence of 0.5 J/cm^2, due to the relatively short pulse duration. Owing to low transmission of our OP-GaP sample at the pump wavelength, this damage threshold is ~6.4 times lower than that reported in the literature for the crystal [106]. However, no surface damage was observed during these measurements.

5.4 Conclusions

In conclusion, we have reported a systematic study on the performance characteristics of tunable pulsed nanosecond DFG in the new semiconductor nonlinear material, OP-GaP. The DFG source has been realized by single-pass mixing of a Q-switched Nd:YAG laser at 1064 nm with the output signal beam from a pulsed OPO based on MgO:PPLN in OP-GaP. We have generated up to ~14 mW of DFG average power at 2719 nm at 80 kHz repetition rate, with >6 mW across the full tuning range of 2548-2781 nm, in TEM_{00} spatial profile. The temperature and spectral acceptance bandwidths for the DFG process in the 40-mm-long OP-GaP sample have been measured to be ΔT~18 ºC and $\Delta\lambda_{signal}$~17 nm, respectively. The corresponding theoretical calculations indicate some discrepancy due to the uncertainty and possible non-uniformity in the grating period, as well as thermal effects due to crystal absorption. Further, we have performed detailed characterization of the nonlinear gain for DFG and its dependence on the polarization of incident pump and signal fields. These measurements have resulted in the achievement of maximum DFG power when the incident beams are polarized along the body diagonal, in good agreement with theory. The transmission measurements of the OP-GaP crystal at the pump and signal wavelengths provide understanding about the DFG efficiency. Moreover, temperature dependence of the transmission in OP-GaP has been investigated in cw, nanosecond, as well as picosecond time-scales. The transmission is found to reduce with temperature in the cw and nanosecond time-scales, while it is found to be improved at high temperatures in the picosecond regime. Detrimental thermal effects were studied by recording the increase in the surface temperature of our OP-GaP crystal. By exploiting the repetition-rate tunability of our nanosecond pump laser, we have estimated the damage threshold of the OP-GaP sample to be ~0.84 J/cm^2. To the best of our knowledge, this work represents the first report on detailed characterization of the OP-GaP crystal for pulsed DFG. We believe further progress in the growth of OP-GaP crystals with higher transmission and improved QPM grating quality in terms of uniformity and aperture, substantial improvements in the efficiency, output power, and beam quality will be attainable, enabling OP-GaP to fully realize its potential as a viable and promising new nonlinear crystal for mid-IR frequency conversion applications.

Chapter 6

Intracavity-seeded pulsed optical parametric oscillator

This Chapter constitutes the following journal publication:

Junxiong Wei, S. Chaitanya Kumar, and M. Ebrahim-Zadeh, “Broadly tunable, intracavity seeded pulsed optical parametric oscillator," Opt. Lett, to be submit (2018)

6.1 Motivation

An all-solid-state tunable source of coherent mid-infrared (mid-IR) radiation with high power, wide tunability and narrow bandwidth is highly desirable for a number of spectroscopic and photochemical applications [107-109]. It would be especially attractive when such a source exhibiting compact foot-print with overall simplicity providing wide wavelength tunability and Fourier transform (FT) limited output pulses. Optical parametric oscillators (OPOs) are one of the most versatile devices to generate radiation in the spectral regions where lasing materials do not exist, or the operation of lasers is otherwise complicated. They can operate in various times-cales providing single-frequency output in the continuous-wave (CW) and FT limited pulses in the ultrafast femtosecond regime, enabling tailorable spectral and temporal properties. However, in the pulsed nanosecond OPO, for the pump laser at any practical margin above oscillation threshold, it tends to oscillate on more than one cavity mode, so that the output signal and idler from OPO are intrinsically multimode and broadband [110]. Although narrow-bandwidth output of a pulsed OPO can be obtained through the use of wavelength selective elements such as gratings or etalons inside the cavity, it required complex techniques to maintain single-mode operation when the system needs to be tuned [111]. An alternative approach to controlling the output wavelengths and optical bandwidth of a nanosecond-pulsed OPO is to use the technique of injection-seeding [112, 113]. In 1969, J. E. Bjorkholm and H. G. Danielmeyer [114] first reported and qualitatively explained injection-seeding of an OPO. They used pulsed single-mode laser ruby as pump for a $LiNbO_3$ OPO, and Nd:YAG laser as seed radiation, to control the spectral properties of the pulsed singly-resonant OPO. One significant advantage of this approach is that the construction of OPO is relatively simplified, as it does not require a complex oscillator cavity to limit the oscillation bandwidth. Several other studies on nanosecond-pulsed OPOs have successfully used a variety of sources for injection-seeding. The vast majority of investigations to date have been performed with fixed seed laser wavelength, focused primarily on attaining lower OPO oscillation threshold, higher efficiency, and narrower linewidth [115, 116].

On the other hand, CW OPOs have been demonstrated as promising candidates for the generation of tunable single-frequency radiation covering spectral regions from the near to mid-IR, with excellent output characteristics [14]. These properties are particularly well suited as tunable seed source for injection-seeding of pulsed OPOs. Here, we report a compact, highly efficient seeding of a pulsed OPO with wide seeding range in a novel configuration. Compared to the relatively complex conventional injection seeding method, with limited tunability [117,118], here we used a singly-resonant CW OPO as an intracavity seed laser for the nanosecond pulsed OPO. Using a 38-mm-long MgO:PPLN crystal, we have generated ~0.94 W of average power with 9.7% slope efficiency at 1677 nm with pulse duration of 29.4 ns for a pump power of 10 W at 80 kHz repetition rate, by parametrically seeding with a narrow linewidth CW OPO internal to the pulsed OPO cavity. The bandwidth of generated signal pulse with intracavity seeding is as narrow as 5.6-MHz, and the seeding operation is achieved from 1510 nm to 1677 nm by temperature tuning of the MgO:PPLN crystal with passive stability better than 1.3% rms over 10 mins in good beam-quality.

6.2 Experimental setup

The schematic of the experimental setup for the intracavity CW OPO injection-seeded nanosecond OPO is shown in Fig. 6.1

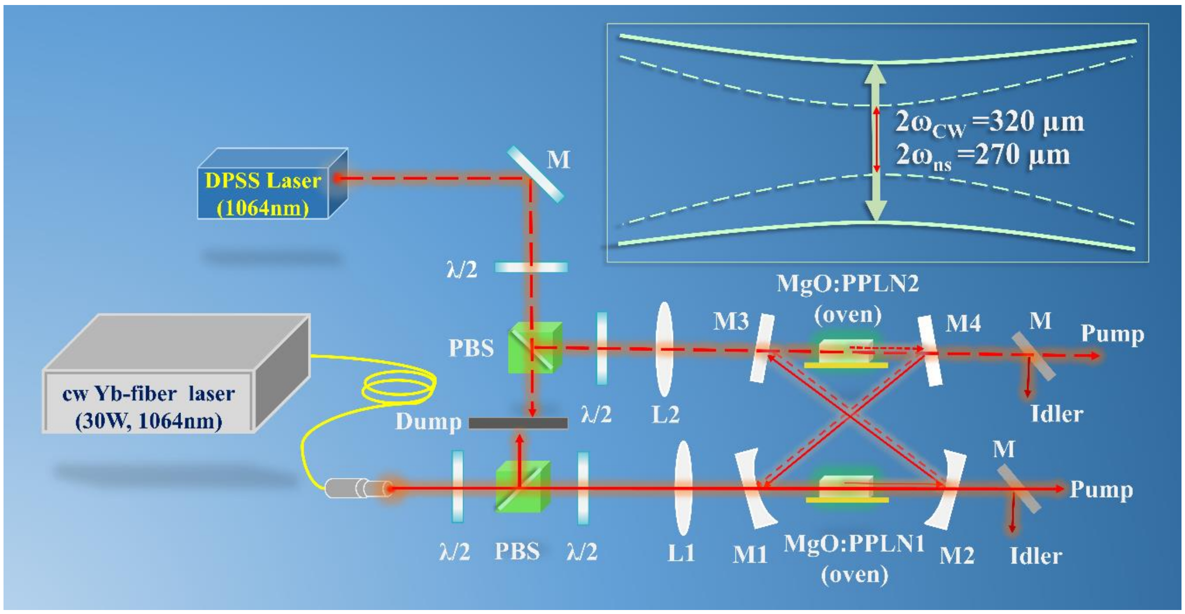

Figure 6.1: Schematic of the experimental setup. HWP: Half-wave-plate, PBS: Polarizing beam-splitter, OC: Output-coupling, M: Mirrors, L: Lens, F: Ge filter, S: signal beam, P: pump beam. Inset is theoretical calculated signal beam waist at the center of MgO:PPLN2, which is 160 µm and135 µm, respectively.

Pump Source: The OPO consists of two pump lasers. The nanosecond pump source is a compact Q-switched diode-pumped Nd: YAG laser operating at 1064 nm (Bright Solutions, Sol). The nanosecond laser provides a maximum output power of 30 W with tunable repetition rate of 20-100 kHz. For the experiments presented in this report, we used a constant repetition rate of 80 kHz, corresponding to a pump pulse duration of ~26 ns. The instantaneous bandwidth and frequency jitter of this laser, measured using an optical spectrum analyzer, is ~0.2 nm and ~1 nm over 30 seconds, respectively. For the CW OPO, the pump source is an Yb-fiber laser (IPG Photonics, YLR-30-SF), which delivers a single-frequency output power of 28 W at 1064 nm in a linearly polarized beam in TEM_{00} spatial mode with a nominal linewidth of 89 kHz. In order to maintain stable output characteristics, both the lasers are operated at maximum power and a combination of a half-wave plate and polarizing beam-splitter is used as variable power attenuator. A second half-wave plate is used to yield the correct pump polarization for phase-matching relative to the crystal orientation.

Nonlinear Gain Medium: The intracavity seeded OPO employs two nonlinear crystal sharing the same cavity. Both the nonlinear crystals are 38-mm-long, 1-mm thick, 5% MgO:PPLN, with five grating periods ranging from Λ= 29.5 - 31.5 µm in steps of 0.5 µm. Here we used MgO:PPLN1 for the cw OPO and MgO:PPLN2 for the pulsed OPO. The end faces of the crystal are AR-coated for high transmission(*R*<4%) for the pump and idler while high reflection (*R*<2%) for the signal over 1300-1900 nm. The crystals are housed in two separate ovens with a stability of ±0.1 ^{o}C, which can be adjusted from room temperature to 200 ^{o}C. Using a precision translation stage, the horizontal position of the MgO:PPLN crystals can be finely adjustable to enable the selection of different grating periods for coarse QPM tuning. Further, finely tunability is attainable by varying the temperature setting of the MgO:PPLN crystals. The pump beams are focused to a waist radius of w_{cw}~50 µm and w_{ns}~110 µm at the center of the MgO:PPLN crystals, corresponding to the focusing parameter, ξ_{cw}~1.1 and ξ_{ns}~0.32, for CW and pulses OPOs respectively. In this system, it not only easily achieve the purpose of matching the CW signal wavelength to the pulsed OPO's cavity modes by properly choosing the temperature and grating, but also the beam diameter of pulsed signal is efficiently mode-matched with the CW signal in the MgO:PPLN2. Depicted in the inset of Fig.1 is theoretical calculated signal beam waist at the center of MgO:PPLN2, with w_{cw}~160 µm and w_{ns}~135 µm, respectively. The total optical length of cavity is ~500 mm. Dichroic mirrors, M, separate the generated idler from the pump.

Cavity: Using two plano-convex lenses (L1, L2) the nanosecond and CW beams are focused at the center of the nonlinear crystal inside the OPO cavity, respectively. The OPO is designed in a ring-cavity with two plano-concave mirrors, M1,2 of radius of curvature, *r*=100 mm, two plane mirror, M3,4. All mirrors, M1-4 are antireflection (AR)-coated for high transmission (*T*>90%) at 1064 nm for the pump, (*T*>80%) over 2.2-4 µm for the idler and high reflectivity (*R*>99%) over 1.3-1.9 µm for the signal, ensuring singly resonant signal oscillation.

6.3 Results and discussions

6.3.1 Temporal profiles

For a nanosecond OPO, parametric waves start up from quantum fluctuations in the signal and idler fields, and cavity buildup time can be a substantial fraction of the pump pulse length, especially near the oscillation threshold. Figure 6.2 shows the real-time pulse profiles, as obtained with a high-speed InGaAs detector (Thorlabs DET08CFC) for the pump and a signal wavelength of 1677 nm signal under seeded and unseeded operation. The pulse width of unseeded pump (black curve) and signal (green curve) is measured to be 26 ns and 23 ns, respectively, and the buildup time of signal is ~17 ns, corresponding roughly to ~11 cavity round-trips.

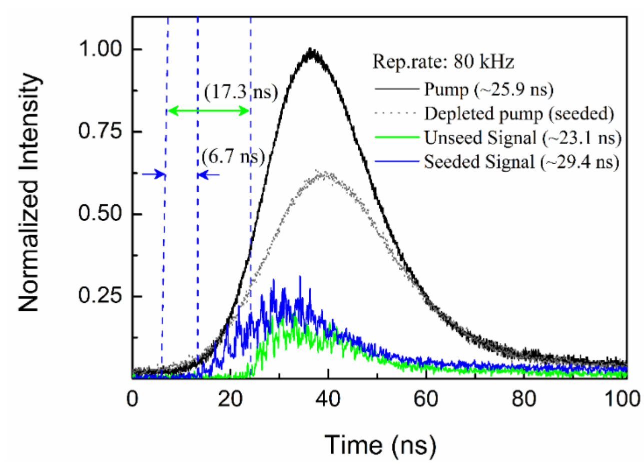

Figure 6.2: Real-time temporal profiles for the incident pump (black curve), depleted pump output (gray curve), unseeded pulsed signal (green curve), and seeded pulsed signal (blue curve). The peak height of the incident pump and signal are normalized to unit height, with the undepleted pump on the same scale.

When the pulsed OPO and CW OPO worked at same time, since the seeded radiation is significantly more intense than the parametric noise, the pulsed OPO tends to oscillate predominantly on this seeded resonant CW OPO cavity mode(s), and hence the buildup time of this seeded cavity mode(s) will be significantly reduced during seeding operation. As a comparison, Fig. 6.2 also shows the profile of seeded pulsed signal (blue solid curve). The buildup time is approximately ~7 ns, which is 10 ns shorter than the unseeded pulsed signal, and weakly dependent upon the pump laser power. Moreover, under seeding operation, it not only increases the intensity of the signal beam, but it lengthens its pulse ($\Delta\tau$~6 ns) due to the faster buildup time, which is expected to get a narrower spectrum bandwidth. The FT limit for the signal, shown in Fig. 6.2 in the ideal case of perfectly Gaussian-shaped pulses ($\Delta\upsilon\Delta\tau$~0.44), results in a bandwidth of $\Delta\upsilon$~14 MHz. In addition, Fig. 6.2 also shows clear pump depletion when the CW OPO is operated simultaneously with the pulsed OPO, indicating seeding operation enhances the conversion efficiency, and we obtain more output power compared to unseeded pulsed OPO, as discussed in the next section.

6.3.2 Spectral bandwidth

Further, we recorded the mode spectrum of the signal. Since the centre wavelength of pump laser is slightly different, as depicted in Fig. 6.3(a), thus the crystal temperature of MgO:PPLN1 and MgO:PPLN2 was optimized to be 55 ^{O}C and 46.2 ^{O}C, respectively, in order to generate identical signal wavelengths. The grating period we used was Λ=31.5 μm. Figure 6.3(b) shows an example of the mode spectrum of the CW signal at the center wavelength of 1677.5 nm, directly recorded by an optical spectrum analyzer (Yokogawa Optical Spectrum Analyzer AQ6370D). For the free-running nanosecond pulsed OPO, the full-width at half-maximum (FWHM) of signal is ~213 GHz (2 nm), as shown in Fig. 6.3(c). Seeding operation was obtained when the CW OPO was tuned to operate simultaneously with the pulsed OPO at 1677.5 nm, and the resulting bandwidth of the pulsed signal is instantaneously reduced to ∼53 MHz (0.05 nm) as compared to the simultaneously measured cw signal linewidth of 0.04 nm, limited by the resolution of the spectrum analyzer, as shown in Fig. 6.3(c). The idler power generated by the CW OPO was measured to be approximately 0.1W. In addition, in order to know the accurate bandwidth of the pulsed signal, we recorded the spectrum using a scanning confocal Fabry-Perot interferometer. The interferometer had a free spectral range (FSR) of 1 GHz and Finesse of 400, corresponding to a resolution of 2.5 MHz. Since the bandwidth of pulsed signal wave is larger than the FSR of interferometer, what is shown on the oscilloscope is detected light, illustrated in Fig. 6.4(d). A typical fringe pattern of cw SRO is shown in Fig. 6.4(a), verifying single longitudinal mode operation on the resonant signal wave.

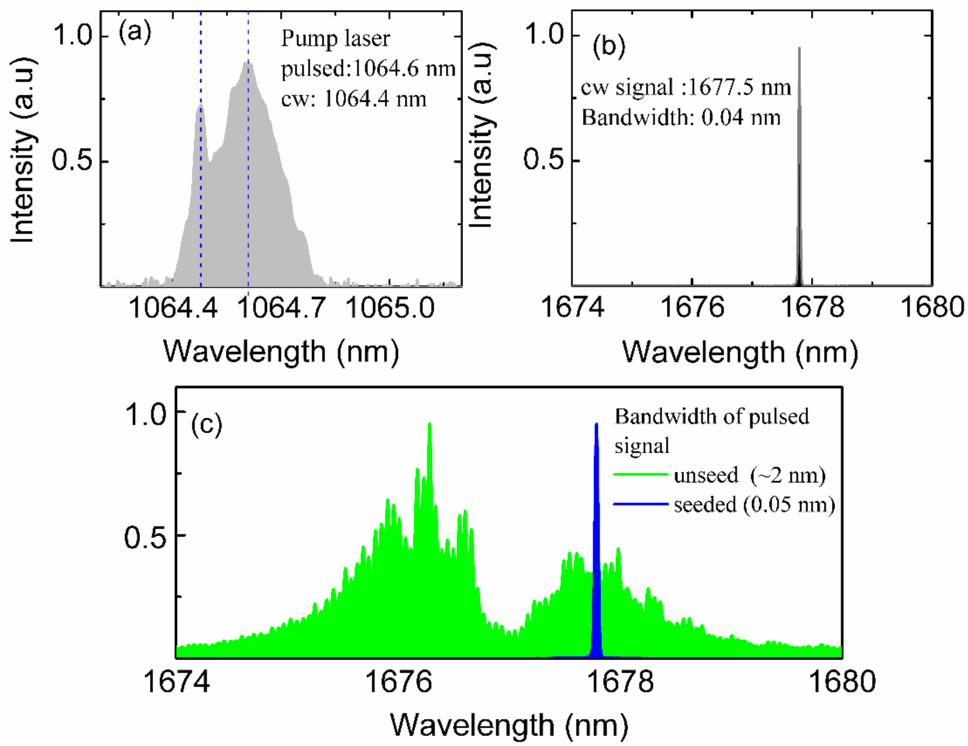

Figure 6.3: (a) The spectrum of the two pump lasers. The spectrum of signal wave at center wavelength of 1677nm. (b) cw (c) unseed and seeded signal.

The instantaneous linewidth, measured directly without accounting for the interferometer resolution, is 3.8 MHz. Once the CW OPO and pulsed OPO worked simultaneously, all unseeded modes of free running pulsed OPO are dramatically suppressed, and the seeded modes radiation is enhanced, with resulting instantaneous bandwidth of pulsed signal measured to be 5.6 MHz, as shown in Fig. 6.4(b). It should be mentioned here that the CW OPO was operated above threshold and the generated cw idler power was measured to be ~0.1 W. Further, we changed the temperature of MgO:PPLN2 from 46.2 °C to 43 °C, and hence the central wavelength of pulsed signal was shifted from 1677.5 nm to 1675.8 nm, resulting in the nanosecond OPO being actually seeded by the CW signal radiation in the wings of the gain profile, instead of to the modes with highest gain. Narrowband pulsed signal was also obtained and the measured bandwidth was recorded to be 16.4

MHz, as shown in Fig. 6.4(c). In addition, we observed the power of the seeded pulsed OPO was reduced with respect to the unseed pulsed OPO when the CW OPO was below threshold. This is because the seed radiation is coupled into the modes in the wings of the gain profile and forces the nanosecond OPO to oscillate on the modes with low gain. This is in agreement with the results of a previous investigation [110]. Figure 6.4(d) shows the spectrum of pulsed signal with CW signal under unseeded operation, which is simply the overlap of signal spectrum.

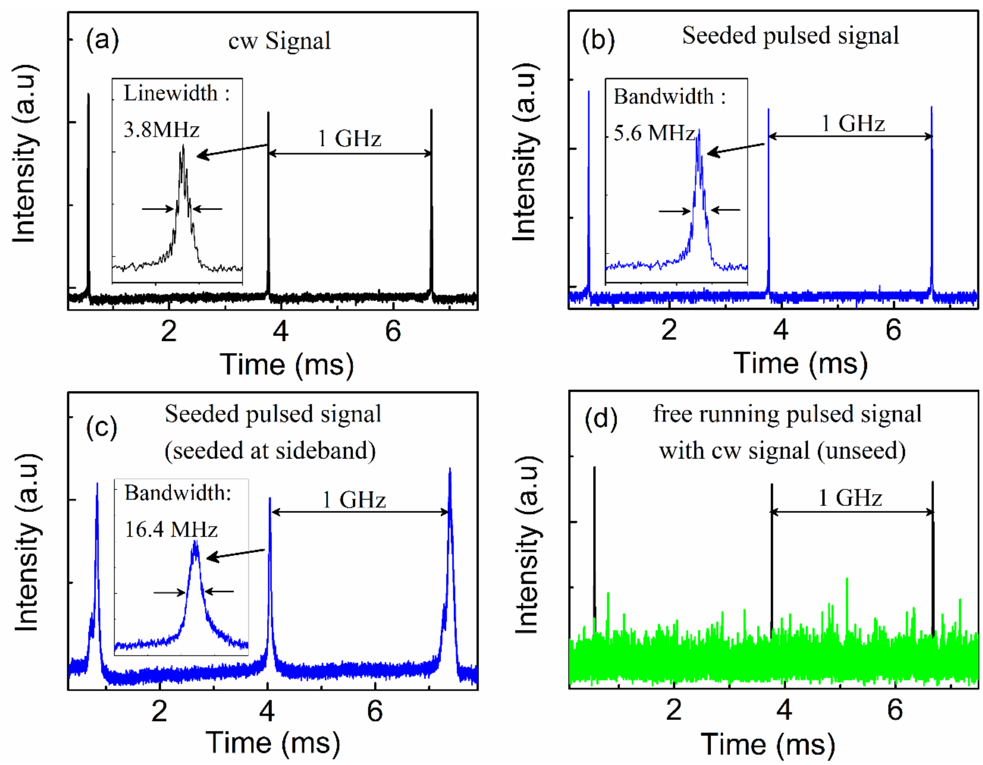

Figure 6.4: (a) Single-frequency spectrum of generated signal, recorded by a scanning Fabry-Perot interferometer, at 1677 nm from CW OPO. (b) Spectrum of signal at 1677nm of seeded pulse PPLN OPO. (c) Spectrum of seeded pulsed signal at wavelength of 1677 nm with CW signal wavelength of 1675.8 nm seed at sideband. (d) Spectrum under unseeded operation. Inset is the zoomed spectrum.

Narrowing the bandwidth of the pulsed OPO was also observed at room temperature and high temperature of 150 °C for grating period of 30 μm, with the results depicted in Fig. 6.5, respectively, corresponding to signal wavelengths of 1510.2 nm and 1535.8 nm.

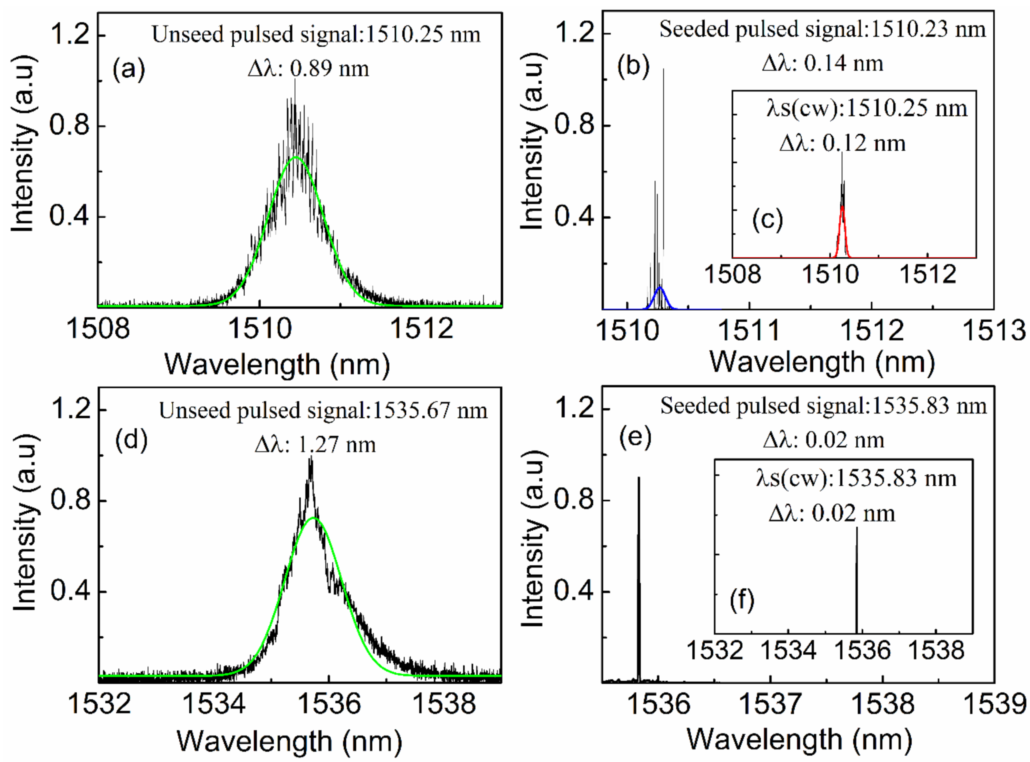

Figure 6.5: Spectrum of (a, d) unseeded pulsed signal at wavelength of 1510.2 nm and 1535.6 nm, respectively. (b, e) seeded pulsed signal at wavelength of 1510.2 nm, and 1535.6 nm, respectively. Inset is CW signal.

We notice that the bandwidth of seeded pulsed signal at 1510.2 nm is broader than that at 1535.8 nm. This is because the linewidth of the CW seed signal at 1510.2 nm is 0.12 nm larger than the linewidth at 1535.8 nm, which is 0.02 nm. However, in both cases the output bandwidth from nanometer to sub-nanometer scale, which shows that CW OPO as a tunable seed laser also works well at both room temperature and high temperature. In principle, while keeping the pump beam fixed, the tunable seeding can be simply achieved by changing the temperature or grating period of the MgO:PPLN crystals.

6.3.3 Power scaling

We also performed power scaling measurements by recording the variation of pulsed idler output power as a function of input pump power for CW OPO seeded and also under unseed operation, with the results shown in Fig. 6.6.

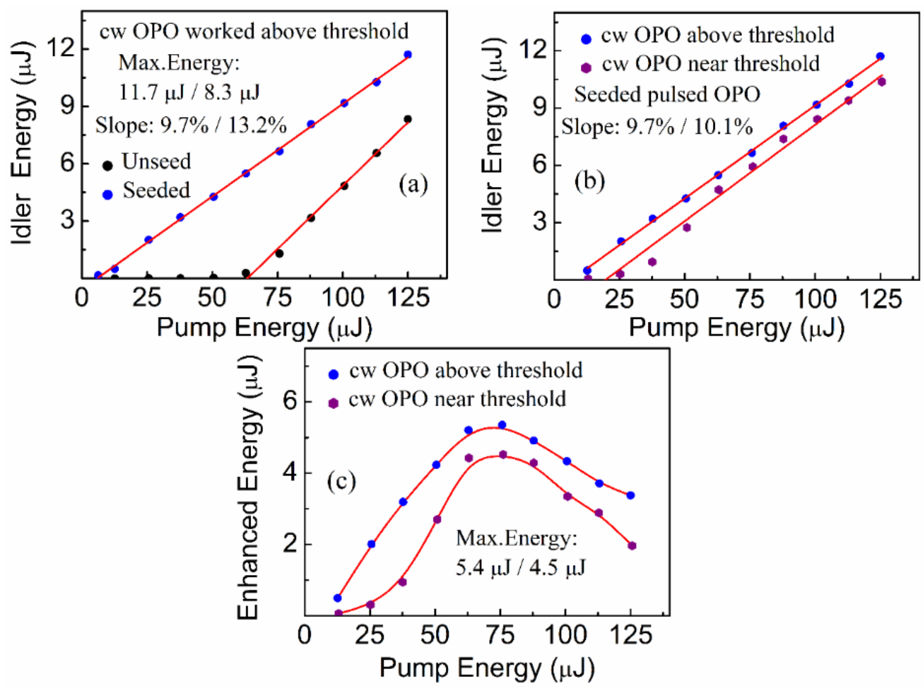

Figure 6.6: (a) Output idler energy generated from the pulsed OPO at wavelength of 1677 nm. Here, the blue dots are the experimental data of the pulsed OPO under seeding operation, and black dots are the experimental data of free-running pulsed OPO. (b) Idler energy generated by the pulsed OPO with different seed power. The blue dots correspond to CW OPO operating above threshold, and violet dots represent CW OPO operating near threshold. (c) Idler energy enhancement at different input pump level. The blue and violet dots correspond to CW OPO operating above threshold and near threshold, respectively.

As mentioned before, the pulsed pump laser is operated at 80 kHz repetition rate with pulse width of 26 ns, after the beam-splitter delivering average power of 30 W. However, in order to avoid any possible damage of crystal, we only used maximum power of 10 W, which corresponds to maximum pump energy of 125 μJ. As expected, when the CW OPO and pulsed OPO were running simultaneously, the output energy increased and the threshold of the pulsed OPO decreased, as shown in Fig. 6.6(a). Here, the CW OPO operated above threshold and near threshold, defined by the detection of CW idler power of approximately 0.1 W and less than 0.01 W, respectively. The seeded pulsed OPO threshold reduced from 5 W to less than 1 W, corresponding to pump pulse energy reducing from 62.5 μJ to 6.3 μJ when the seed laser, the CW OPO, operated above threshold. For the maximum input pump energy of 125 μJ, the free-running pulsed OPO emitted an idler energy of 8.3 μJ with a slope efficiency of 13.2%. With CW OPO operating above threshold for seeded operation, an additional 3.4 μJ of idler radiation was generated, which corresponds to an idler slope efficiency of ~9.7%. Further, we measured the pulsed energy of idler with the CW OPO operating near threshold. Although the generated energy of pulsed idler is lower with CW OPO near threshold than above threshold, the slope efficiency is almost same, as is shown in Fig. 6.6(b), which means for seeding operation there is no need for a high power seed laser. In addition, we also calculated the energy enhancement at both of case. As is shown in Fig. 6.6(c), the enhanced energy reached maximum of 5.4 μJ and 4.5 μJ with the same trend, when the CW OPO operated above threshold and near threshold, respectively.

6.3.4 Power stability and beam profile

We also recorded the long-term passive idler power stability of the nanosecond OPO under seeded operation, with the results depicted in Fig. 6.7 (a). The generated idler power at a central wavelength of 2910 nm was recorded to exhibit a passive stability better than 1.3% rms over 10 mins, as compared to the simultaneously measured pulsed pump and CW idler power stability of 0.2% and 6.7% rms measured at 1064.5 nm and 2910 nm, respectively. In addition, we measured the far-field energy distribution of the pulsed pump and signal beam at a wavelength of 1677 nm using a pyroelectric camera from the leakage of cavity, with the results shown in Fig. 6.7(b). It clearly shows the pulsed signal beam quality improved from high-order transvers mode to fundamental mode, and it could be further improved by using a better pump laser.

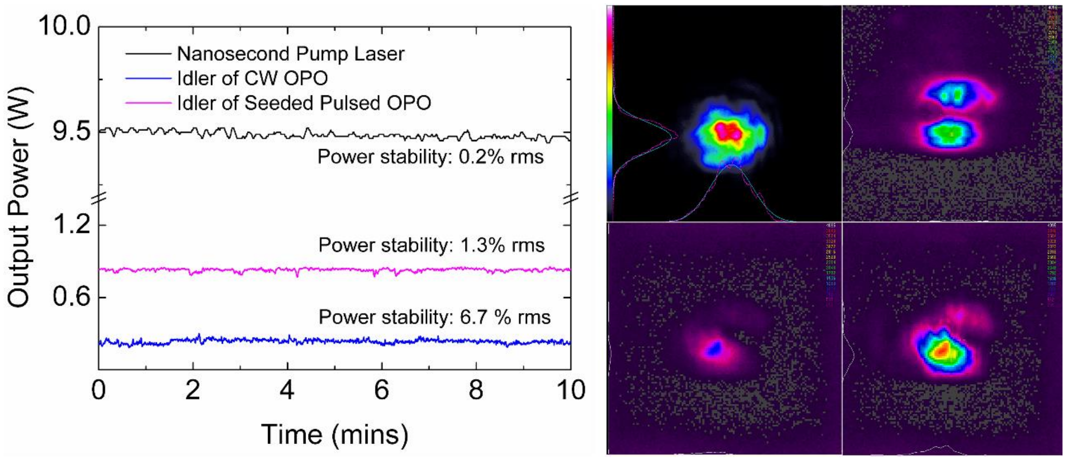

Figure 6.7: (a) Long-term power stability of the extracted idler from the MgO: PPLN OPO measured a period of 10 minutes. (b) Beam profiles of the pulsed pump and signal from nanosecond OPO.

6.4 Conclusions

In conclusion, we have introduced a novel configuration, referred as tandem OPO, for injection-seeded pulsed OPO system. This method completes the mission of realizing injection seeding in almost all tuning range of OPOs. Unique possibilities for seeding operation are offered by this system, including automatically realization of spatial modes overlap and easily attainable spectral mode-matching with large spectral range. Without using an output coupler, we were able to extract up to 0.945 W of average power at 2910 nm from 0.5 meter long cavity at an extraction efficiency of ~9.3% and power stability better than 1.3% rms for the idler. The seeded pulsed signal exhibits a shorter buildup time of 6.7 ns and broader pulsed bandwidth of 29.4 ns compared to the buildup time of 17.3 ns and bandwidth of 23.1 ns for unseeded pulsed signal. The OPO can be seeded over 1510-1677 nm in the signal, providing a total seeding range of 167 nm in the near-IR region, simply by changing the temperature or grating of the MgO:PPLN crystal, and the instantaneous bandwidth of pulsed signal is measured to be 5.6 MHz. From a more general viewpoint, the method shown here will work at other wavelength range of OPO as well, opening a new path toward injection-seeding or injection-locking of pulse OPOs across the full tuning range and outstanding emission properties.

Chapter 7

Summary and outlook

7.1 Summary

The goal of our research work was to exploit optical frequency conversion techniques in novel nonlinear materials and deploy innovative design architectures to provide tunable radiation in new and difficult spectral regions in the mid-IR, which can be applied directly in spectroscopy research or will be especially important for trace gas sensing and imaging applications.

In this thesis, we demonstrated an angle-tuned MgO:PPLN picosecond OPO, synchronously pumped by a Yb-fiber laser, for the first time to the best of our knowledge. The OPO is tunable from 1413-1900 nm in the signal along with idler tunability from 2418-4307 nm, providing a total tunability of 2376 nm in the near-to-mid-IR region, simply by angular interrogation of the MgO:PPLN crystal at room temperature. Using a 10% output coupler, we were able to extract up to 2.4 W of signal at 1664 nm along with an idler power of 1.7 W at 2950 nm corresponding to an over-all extraction efficiency of ~45% with good beam pointing stability better than 30 μrad and 14 μrad for the signal and idler, respectively. The generated signal and idler are recorded to exhibit passive power stability better than 1% rms and 0.8% rms over 15 hours at 1638 nm and 3036 nm respectively in good beam quality with TEM_{00} mode profile. Further, the spectral and temporal measurements performed on the signal pulses at ~1647 nm resulted in a Gaussian temporal width of 15.2 ps with a FWHM spectral bandwidth of 0.7 nm, corresponding to a time-bandwidth product $\Delta\upsilon\Delta\tau$~1.2. Further improvement in the AR-coatings for the signal and idler wavelength regions and optimization of the output coupling could lead to a higher extraction efficiency of the OPO. These results indicate the potential for rapid and similarly wide tunability of high power OPOs as compared to the temperature-tuned devices.

We also have demonstrated a novel configuration, referred as tandem OPO, for injection-seeded pulsed OPO system. This method completes the mission of realizing injection-seeding across the full tuning range of nanosecond OPOs. Unique possibilities for seeding operation are offered by this system, including automatical realization of spatial mode overlap and easily attainable spectral mode-matching over a broad spectral range. Without using an output coupler, we were able to extract up to 0.945 W of average power at 2910 nm from 0.5 meter long cavity with an extraction efficiency of ~9.3% and power stability better than 1.3% rms for the idler. The seeded pulsed signal exhibit a shorter buildup time of 6.7 ns and broader pulsed bandwidth of 29.4 ns compared to the buildup time of 17.3 ns and bandwidth of 23.1 ns of unseeded pulsed signal. The OPO can be seeded across 1510-1677 nm in the signal, providing a total seeding range of 167 nm in the near-IR region, simply by changing the temperature or grating period of the MgO:PPLN crystal, and the instantaneous bandwidth of pulsed signal is measured to be 5.6 MHz. From a more general viewpoint, the method shown here will work at other wavelength range of OPOs as well, opening a new path toward injection seeding or injection locking of pulse OPOs with full tuning range and outstanding emission properties.

In order to ultimately access the deep infrared range, we have reported a systematic study on the performance characteristics of tunable pulsed nanosecond DFG in the new semiconductor nonlinear material, OP-GaP. The DFG source has been realized by single-pass mixing of a Q-switched Nd:YAG laser at 1064 nm with the output signal beam from a pulsed OPO based on MgO:PPLN in OP-GaP. We have generated up to ~14 mW of DFG average power at 2719 nm at 80 kHz repetition rate, with >6 mW across the full tuning range of 2548-2781 nm, in TEM_{00} spatial profile. The temperature and spectral acceptance bandwidths for the DFG process in the 40-mm-long OP-GaP sample have been measured to be ΔT~18 ºC and $\Delta\lambda_{signal}$~17 nm, respectively. The corresponding theoretical calculations indicate some discrepancy due to the uncertainty and possible non-uniformity in the grating period, as well as thermal effects due to crystal absorption. Further, we have also performed detailed characterization of the nonlinear gain for DFG and its dependence on the polarization of incident pump and signal fields. These measurements have resulted in the achievement of maximum DFG power when the incident beams are polarized along the body diagonal, in good agreement with theory. The transmission measurements of the OP-GaP crystal at the pump and signal wavelengths provide understanding about the DFG efficiency.

Moreover, temperature dependence of the transmission in OP-GaP has been investigated in CW, nanosecond as well as picosecond time-scales. The transmission is found to reduce with temperature in the CW and nanosecond time-scales, while it is found to be improved at high temperatures in the picosecond regime. Detrimental thermal effects were studied by recording the increase in the surface temperature of the OP-GaP crystal. By exploiting the repetition-rate tunability of our nanosecond pump laser, we have estimated the damage threshold of the OP-GaP sample to be ~0.84 J/cm^2. To the best of our knowledge, this is the first report on detailed characterization of the OP-GaP crystal for pulsed DFG. We believe, with further progress in the growth of OP-GaP crystals with higher transmission and improved QPM grating quality in terms of uniformity and aperture, substantial improvements in the efficiency, output power, and beam quality will be attainable, enabling OP-GaP to fully realize its potential as a viable and promising new nonlinear crystal for mid-IR frequency conversion applications.

7.2 Outlook

Based on our achievements, the requirements for spectroscopy research, and the direction of development in the research field of nonlinear frequency conversion, we plan to make progress in the following aspects:

As a direction for the future work, the performance of the OPOs in terms of power stability can be further improved by better temperature control, isolation from mechanical vibrations, and active stabilization of cavity length. In Chapter 5, we performed detailed studies of the non-oxide crystal OP-GaP, which is a promising candidate for deep mid-IR laser generation directly pumped using well-established, widely available, and cost-effective solid-state and fiber lasers at 1064 nm. The demonstrated of DFG based on OP-GaP in the 2-3 μm can be further extended to cover the entire OP-GaP transparency range up to 12 μm using different grating periods. Thus, as a direction for the future work, we will develop an Yb-fiber-laser-pumped CW OPOs tunable in the spectral region beyond 4 μm, based on OP-GaP.

For the generation of tunable deep-mid-IR radiation by frequency conversion, another attractive nonlinear crystal candidate is $ZnGeP_2$ (ZGP) crystal. It combines a very high second-order nonlinear optical coefficient (d_{eff} =75 pm/V) and wide mid-IR transparency (0.75-12 μm) with excellent thermal conductivity (0.36 W/cm·K). It offers a large nonlinear optical figure-of-merit, and a high optical damage threshold. To date, most of research efforts on $ZnGeP_2$ OPOs are still in nanosecond regime, where ultrabroad tunability (3.8-12.4 μm) has been demonstrated. In the ultrashort picosecond regime, synchronously pumped $ZnGeP_2$ OPOs have also been reported. However, to our knowledge, CW mid-IR sources based on $ZnGeP_2$ OPOs have not been investigated. As such, the development of ZGP OPOs represents an important strategy to achieve deep mid-IR radiation in CW configuration. For pumping the ZGP OPO, radiation beyond 2 μm with good beam quality is required. An attractive and convenient way to produce such wavelength is to wavelength-double a 1.064 μm laser using a degenerate OPO. Hence, along with this research, a compact, stable, efficient degenerate OPO operating in the 2.1-μm region will be developed. The first OPO will generate 2.1-μm radiation, which will in turn be used to pump the ZGP OPO to provide 4-10 μm radiation.

Bibliography

[1] M. Ebrahim-Zadeh and I. T. Sorokina, "Mid-infrared Coherent Sources and Applications," Springer (2008).

[2] C. Calabrese, A. M. Stingel, L. Shen, and P. B. Petersen, "Ultrafast continuum mid-infrared spectroscopy: probing the entire vibrational spectrum in a single laser shot with femtosecond time resolution," Opt. Lett. 37, 2265-2267 (2012)

[3] J. C. Nicolas, A. N. Baranov, Y. Cuminal, Y. Rouillard, C. Alibert, "Tunable diode laser absorption spectroscopy of carbon monoxide around 2.35 µm," Appl. Opt. 37, 7906-7911 (1998)

[4] D. Halmer, S. Thelen, P. Hering, and M. Mürtz, "Online monitoring of ethane traces in exhaled breath with a difference frequency generation spectrometer," Appl. Phys. B: Lasers Opt. 85, 437-443 (2006).

[5] J. Hodgkinson and R. P. Tatam, "Optical gas sensing: a review," Meas. Sci. Technol. 24, 012004 (2013).

[6] M. G. Hansen, E. Magoulakis, Q. Chen, I. Ernsting, and S. Schiller, "Quantum cascade laser-based mid-IR frequency metrology system with ultra-narrow linewidth and 1×10^{-13}-level frequency instability," Opt. Lett. 40, 2289-2292 (2015).

[7] M. N. Petrovich, F. Poletti, J. P. Wooler, A. M. Heidt, N. K. Baddela, Z. Li, D. R. Gray, R. Slavík, F. Parmigiani, N. V. Wheeler, J. R. Hayes, E. Numkam, L. Grűner-Nielsen, B. Pálsdóttir, R. Phelan, B. Kelly, J. O'Carroll, M. Becker, N. MacSuibhne, J. Zhao, F. C. Garcia Gunning, A. D. Ellis, P. Petropoulos, S. U. Alam, and D. J. Richardson, "Demonstration of amplified data transmission at 2 µm in a low-loss wide bandwidth hollow core photonic bandgap fiber," Opt. Exp. 21, 28559-28569 (2013)

[8] J. G. Fujimoto, C. Pitris, S. Boppart, and M. Brezinski, "Optical Coherence Tomography: An Emerging Technology for Biomedical Imaging and Optical Biopsy," Neoplasia. 2, 9 (2000).

[9] J. G. Fujimoto, "Optical coherence tomography for ultrahigh resolution in vivo imaging," Nat Biotechnol. 21, 1361-7 (2003).

[10] F. K. Tittel and R. Lewicki, "Tunable mid-infrared laser absorption spectroscopy," in Semiconductor Lasers, Woodhead, 579-630 (2013)

[11] M. Ebrahim-Zadeh, "Mid-infrared ultrafast and continuous-wave optical parametric oscillators," Springer, 179-218 (2003).

[12] M. Ebrahim-Zadeh, S. Chaitanya Kumar, A. Esteban-Martin, and G. K. Samanta, "Breakthroughs in photonics 2012: breakthroughs in optical parametric oscillators," IEEE Photon. J. 5, 0700105 (2013).

[13] D. Richter, A. Fried, and P. Weibring, "Difference frequency generation laser based spectrometers," Laser & Photon. Rev. 3, 343-354 (2009)

[14] M. Ebrahim-Zadeh, S. Chaitanya Kumar, and K. Devi, "Yb-Fiber-Laser-Pumped Continuous-Wave. Frequency Conversion Sources from the. Mid-Infrared to the Ultraviolet," IEEE J. Sel. Top. Quantum Electron. 20, 350 (2014).

[15] M. Ebrahim-Zadeh and S. Chaitanya Kumar, "Yb-Fiber-Laser-Pumped Ultrafast Frequency Conversion Sources From the Mid-Infrared to the Ultraviolet," IEEE J. Sel. Top. Quantum Electron. 20, 624 (2014).

[16] J. A. Giordmaine and R. C. Miller, "Tunable Coherent Parametric Oscillation in $LiNbO_3$ at Optical Frequencies," Phys. Rev. Lett. 14, 973 (1965).

[17] C. Chen, B. Wu, A. Jiang, G. You, "A new type ultraviolet SHG crystal β-BaB_2O_4," Sci. Sin., Ser. B. 28, 235 (1985)

[18] C. Chen, Y. Wu, A. Jiang, B. Wu, G. You, R. Li, S. Lin, "New nonlinear-optical crystal:LiB_3O_5, " J. Opt. Soc. Am. B. 6, 616-621 (1989).

[19] F. C. Zumsteg, J. D. Bierlein, and T. E. Gier, "$K_xRb_{1-x}TiOPO_4$: a new nonlinear optical material," J. Appl. Phys. 47, 4980 (1976).

[20] S. T. Yang, R. C. Eckardt, and R. L. Byer, "Continuous-wave singly resonant optical parametric oscillator pumped by a single-frequency resonantly doubled Nd:YAG laser," Opt. Lett. 18, 971-973 (1993).

[21] M. Yamada, N. Nada, M. Saitoh, and K. Watanabe, "First order quasi-phase matched $LiNbO_3$ waveguide periodically poled by applying an external field for efficient blue second harmonic generation," Appl. Phys. Lett. 62, 435-436 (1993)

[22] S. N. Zhu, Y. Y. Zhu, Z. Y. Zhang, H. Shu, H. F. Wang, J. F. Hong, C. Z. Ge, and N. B. Ming, “$LiTaO_3$ crystal periodically poled by applying an external pulsed field,” J. Appl. Phys.77, 5481-5483 (1995).

[23] W. R. Bosenberg, A. Drobshoff, J. I. Alexander, L. E. Myers and R. L. Byer, “93%-pump depletion, 3.5-W continuous-wave, singly resonant optical parametric oscillator, ” Opt. Lett. 21, 1336-1338 (1996).

[24] V. Petrov, “Frequency down-conversion of solid-state laser sources to the mid-infrared spectral range using non-oxide nonlinear crystals,” Prog. Quantum Electron. 42, 1-106 (2015).

[25] J. R. Schwesyg, M. C. C. Kajiyama, M. Falk, D. H. Jundt, K. Buse, M. M. Fejer, “Light absorption in undoped congruent and magnesium doped lithium niobate crystals in the visible wavelength range,” Appl. Phys. B: Lasers Opt. 100, 109 (2010)

[26] J. Reid and K. Siemsen, “New CO_2 laser bands in the 9-11-μm wavelength region,” Appl. Phys. Lett. 29, 250-251 (1976).

[27] W. J. Witteman, “The CO_2 laser,” Springer-Verlag (1987)

[28] S. Jung, A. Jiang, Y. Jiang, K. Vijayraghavan, X. Wang, M. Troccoli, and M. A. Belkin, “Broadly tunable monolithic room-temperature terahertz quantum cascade laser sources,” Nat. Commun. 5, 4267 (2014)

[29] N. Bandyopadhyay, Y. Bai, S. Slivken, and M. Razeghi, “High power operation of λ~5.2-11μm strain balanced quantum cascade lasers based on the same material composition,” Appl. Phys. Lett. 105, 071106 (2014)

[30] K. Devi, P. G. Schunemann, and M. Ebrahim-Zadeh, “Continuous-wave, multimilliwatt, mid-infrared source tunable across 6.4-7.5 μm based on orientation-patterned GaAs,” Opt. Lett. 39, 6751-6754 (2014).

[31] R. K. Feaver, R. D. Peterson, and P. E. Powers, “Longwave-IR optical parametric oscillator in orientation-patterned GaAs pumped by a 2 μm Tm, Ho:YLF laser,” Opt. Exp. 21, 16104-16110 (2013).

[32] M. Henriksson, M. Tiihonen, V. Pasiskevicius, and F. Laurell, “Mid-infrared ZGP OPO pumped by near-degenerate narrowband type-I PPKTP parametric oscillator,” Appl. Phys. B: Lasers Opt. 88, 37-41 (2007).

[33] R. L. Sutherland, “Handbook of Nonlinear Optics,” Marcel Dekker (2003).

[34] R. W. Boyd, "Nonlinear Optics," Academic Press (2007).

[35] M. Ebrahim-Zadeh, M. H. Dunn, "Optical Parametric Oscillators," Handbook of Optics, Vol. 4, (McGraw-Hill, New York 2000).

[36] P. A. Franken, A. E. Hill, C. W. Peters, and G. Weinreich, "Generation of optical harmonics," Phys. Rev. Lett. 7, 118-119 (1961).

[37] M. Bass, P. A. Franken, J. F. Ward, and G. Weinreich, "Optical Rectification," Phys. Rev. Lett. 9, 446 (1962).

[38] W. H. Louisell, A. Yariv, and A. E. Siegman, "Quantum Fluctuations and Noise in Parametric Processes. I," Phys. Rev. 124, 1645 (1961).

[39] J. P. Gordon, W. H. Louisell, and L. R. Walker, "Quantum Fluctuations and Noise in Parametric Processes. II," Phys. Rev. 129, 481 (1963).

[40] W. G. Wagner, R. W. Hellwarth, "Quantum Noise in a Parametric Amplifier with Lossy Modes," Phys. Rev. 133, A915 (1964).

[41] D. A. Kleinman. "Nonlinear Dielectric Polarization in Optical Media," Phys. Rev.126, 1977 (1962).

[42] J. A. Armstrong, N. Bloembergen, J. Ducuing, and P. S. Pershan, "Interactions between Light Waves in a Nonlinear Dielectric," Phys. Rev. 127, 1918-1939 (1962).

[43] J. Q. Yao and T. S. Fahlen, "Calculations of Optimum Phase Match Parameters for the Biaxial Crystal $KTiOPO_4$," J. Appl. Phys. 55, 65-68 (1984).

[44] W. Koechner, "Solid-state laser engineering," Springer, Berlin5th ed. 639 (1999).

[45] B. Boulanger and J. Zyss, International Tables for Crystallography, Springer, 178-219 (2006).

[46] G. D. Boyd and C. K. N. Patel, "Enhancement of Optical Second-harmonic Generation (SHG) by Reflection Phase Matching in ZnS and GaAs," Appl. Phys. Lett. 8, 313-315 (1966).

[47] H. Hellwig, J. Liebertz, and L. Bohaty, "Linear optical properties of the monoclinic bismuth borate BiB_3O_6," J. Appl. Phys. 88, 240-244 (2000)

[48] V. G. Dmitriev, G. G. Gurzadyan, D. N. Nikogosyan, Handbook of Nonlinear Optical Crystals, Springer (1999).

[49] D. N. Nikogosyan, "Nonlinear Optical Crystals: A Complete Survey," Springer (2005).

[50] H. Kouta, "Wavelength dependence of repetitive-pulse laser-induced damage threshold in β-BaB_2O_4," Appl. Opt. 38, 545-547 (1999).

[51] H. Nakatani, W. R. Bosenberg, L. K. Cheng, C. L. Tang, "Laser-induced damage in beta barium metaborate," Appl. Phys. Lett. 53, 2587-2589 (1988).

[52] R. M. Wood, R. T. Taylor, R. L. Rouse, "Laser damage in optical materials at 1.06μm," Opt. Laser Technol. 6, 105-111 (1975).

[53] J. E. Swain, S. E. Stokowski, D. Milam, G. C. Kennedy, "The effect of baking and pulsed laser irradiation on the bulk laser damage threshold of potassium dihydrogen phosphate crystals," Appl. Phys. Lett. 41, 12-14 (1982).

[54] S. E. Moody, J. M. Eggleston, J. F. Seamans, "Long-pulse second-harmonic generation in KTP," IEEE J. Quant. Electr. QE. 23, 335-340 (1987).

[55] F. Ahmed, "Laser damage threshold of $KTiOPO_4$," Appl. Opt. 28, 119-122 (1989).

[56] S. Favre, T. C. Sidler, R. P. Salathe, "High-power long-pulse second harmonic generation and optical damage with free-running Nd:YAG laser," IEEE J. Quant. Electr. 39, 733-740 (2003).

[57] C. Chen, Y. Wu, A. Jiang, B. Wu, G. You, R. Li, S. Lin, "New nonlinear-optical crystal: LiB_3O_5," J. Opt. Soc. Am. B. 6, 616-621 (1989).

[58] F. Xie, B. Wu, G. You, C. Chen, "Characterization of LiB_3O_5 crystal for second-harmonic generation," Opt. Lett. 16, 1237-1239 (1991).

[59] M. J. Soileau, "Mechanism of laser-induced failure in antireflection-coated $LiNbO_3$ crystals," Appl. Opt. 20, 1030-1033 (1981).

[60] M. Bass, "Nd:YAG laser-irradiation-induced damage to $LiNbO_3$ and KDP," IEEE J. Quant. Electr. QE. 7, 350-359 (1971).

[61] L. E. Myers, G. D. Miller, R. C. Eckardt, M. M. Fejer, R. L. Byer, W. R. Bosenberg, "Quasi phase- matched 1.064-μm-pumped optical parametric oscillator in bulk periodically poled $LiNbO_3$," Opt. Lett. 20, 52-54 (1995).

[62] P. E. Britton, D. Taverner, K. Puech, D. J. Richardson, P. G. R. Smith, G. W. Ross, D. C. Hanna, "Optical parametric oscillation in periodically poled lithium niobate driven by a diode-pumped Q-switched erbium fiber laser," Opt. Lett. 23, 582-584 (1998).

[63] R. D. Peterson, K. L. Schepler, J. L. Brown, P. G. Schunemann, "Damage properties of $ZnGeP_2$ at 2 μm," J. Opt. Soc. Am. B. 12, 2142-2146 (1995).

[64] T. H. Allik, S. Chandra, D. M. Rines, P. G. Schunemann, J. A. Hutchinson, R. Utano, "Tunable 7-12-μm optical parametric oscillator using a Cr,Er:YSGG laser to pump CdSe and $ZnGeP_2$ crystals," Opt. Lett. 22, 597-599 (1997).

[65] N. P. Andreeva, S. A. Andreev, I. N. Matveev, S. M. Pshenichnikov, N. D. Ustinov, "Parametric conversion of infrared radiation in zinc-germanium diphosphide," Sov. J. Quantum Electron. 9, 208-210 (1979).

[66] K. T. Zawilski, P. G. Schunemann, T. M. Pollak, D. E. Zelmon, N. C. Fernelius, and F. K. Hopkins, "Growth and characterization of large $CdSiP_2$ single crystals," J. Cryst. Growth. 312, 1127-1132 (2010).

[67] S. Chaitanya Kumar, P. G. Schunemann, K. T. Zawilski, and M. Ebrahim-Zadeh, "Advances in ultrafast optical parametric sources for the mid-infrared based on $CdSiP_2$," J. Opt. Soc. Am. B 33, D44-D56 (2016)

[68] A. Dhollande, C. Kieleck, G. Marchev, P. G. Schunemann, K. T. Zawilski, V. Petrov, and M. Eichhorn,"Laser-Induced Damage Study at 1.064 and 2.09 μm of High Optical Quality $CdSiP_2$ Crystal," in Advanced Solid State Lasers, paper AM2A.8, (2015).

[69] A. Hildenbrand, C. Kieleck, A. Tyazhev, G. Marchev, G. Stöppler, M. Eichhorn, P. G. Schunemann, V. Petrov, "Laser damage studies of $CdSiP_2$ and $ZnGeP_2$ nonlinear crystals with nanosecond pulses at 1064 and 2090 nm," Proc. of SPIE, 896417 (2014)

[70] T. Skauli, K. L. Vodopyanov, T. J. Pinguet, A. Schober, O. Levi, L. A. Eyres, M. M. Fejer, J. S. Harris, B. Gerard, L. Becouarn, E. Lallier, and G. Arisholm, "Measurement of the nonlinear coefficient of orientation patterned GaAs and demonstration of highly efficient second-harmonic generation," Opt. Lett. 27, 628-630 (2002).

[71] T. J. Pinguet, O. Levi, T. Skauli, L. A. Eyres, L. Scaccabarozzi, M. M. Fejer, J. S. Harris, T. J. Kulp, S. Bisson, B. Gerard, L. Becouarn, and E. Lallier, "Characterization of 0.5 mm thick films of orientation-patterned GaAs for nonlinear optical applications," Conference on Lasers and Electro-Optics, OSA Trends in Optics and Photonics, Vol. 56, 138 (2001)

[72] P. G. Schunemann, L. A. Pomeranz, and D. J. Magarrell, "Optical parametric oscillation in quasi-phase-matched GaP," Proc. of SPIE, 93470J-1 (2015).

[73] S. Guha, J. O. Barnes, P. G. Schunemann, "Mid-wave infrared generation by difference frequency mixing of continuous wave lasers in orientation-patterned gallium phosphide," Opt. Mater. Express. 5, 2911-2923 (2015)

[74] J. Wei, S. Chaitanya Kumar, H. Ye, K. Devi, P. G. Schunemann, and M. Ebrahim-Zadeh, "Nanosecond difference-frequency generation in orientation-patterned gallium phosphide," Opt. Lett. 42, 2193-2196 (2017)

[75] G. D. Boyd, A. Ashkin, "Theory of parametric oscillator threshold with single mode optical masers and observation of amplification in $LiNbO_3$," Phys. Rev. A. 146, 187-198 (1966)

[76] S. J. Brosnan and R. L. Byer, "Optical parametric oscillator threshold and linewidth studies," IEEE J. Quantum Electron. QE. 15, 415-431 (1979).

[77] S. Chaitanya Kumar, R. Das, G. K. Samanta, and M. Ebrahim-Zadeh, "Optimally-output-coupled, 17.5 W, fiber-laser-pumped continuous-wave optical parametric oscillator," Appl. Phys. B: Lasers Opt. 102, 31-35 (2011).

[78] O. Paul, A. Quosig, T. Bauer, M. Nittmann, J. Bartschke, G. Anstett and J. A. L'Huillier, "Temperature-dependent Sellmeier equation in the MIR for the extraordinary refractive index of 5% MgO doped congruent $LiNbO_3$," Appl. Phys. B: Lasers Opt. 86, 111-115 (2007).

[79] O. Svelto, "Principles of Lasers," Springer (2010).

[80] D. S. Hum and M. M. Fejer, "Quasi-phase matching," C. R. Phys. 8, 180-198 (2007).

[81]. I. Ricciardi, M. De Rosa, A. Rocco, P. Ferraro, A. Vannucci, P. Spano, and P. De Natale, "Sum-frequency generation of cw ultraviolet radiation in periodically poled $LiTaO_3$" Opt. Lett. 39, 1348-1350 (2009).

[82] C. Zhang, Y. Avetisyan, A. Glosser, I. Kawayama, H. Murakami, and M. Tonouchi, "Bandwidth tunable THz wave generation in large-area periodically poled lithium niobate," Opt. Exp. 20, 8784-8790 (2012).

[83] S. Chaitanya Kumar, A. Esteban-Martin, T. Ideguchi, M. Yan, S. Holzner, T. W. Hänsch, N. Picqué and M. Ebrahim-Zadeh, "Few-cycle, broadband, mid-infrared optical parametric oscillator pumped by a 20-fs Ti:sapphire laser," Laser & Photon. Rev. 8, L86-L91 (2014).

[84] K. Devi, S. Chaitanya Kumar, and M. Ebrahim-Zadeh, "High-power, continuous-wave, single-frequency, all-periodically-poled, near-infrared source," Opt. Lett. 37, 5049-5051 (2012).

[85] A. Aadhi, A. Chaitanya N, M. V. Jabir, R. P. Singh, and G. K. Samanta, "All-periodically poled, high-power, continuous-wave, single-frequency tunable UV source," Opt. Lett. 40, 33-36 (2015).

[86] H. Ishizuki and T. Taira, "Half-joule output optical-parametric oscillation by using 10-mm-thick periodically poled Mg-doped congruent $LiNbO_3$," Opt. Exp. 20, 20002-20010 (2012)

[87] B. Zhang, J. Yao, H. Zhang, D. Xu, P. Wang, X. Li, and X. Ding, "Angle-tuned Signal-resonated Optical Parametric Oscillator based on Periodically Poled Lithium Niobate," Chin. Opt. Lett. 1, 346-349 (2003).

[88] V. Kemlin, D. Jegouso, J. Debray, P. Segonds, B. Boulanger, B. Menaert, H. Ishizuki, and T. Taira, "Widely tunable optical parametric oscillator in a 5 mm thick 5% MgO:PPLN partial cylinder," Opt. Lett. 38, 860-862 (2013).

[89] D. A. Kleinman, A. Ashkin, and G. D. Boyd, "Second-harmonic generation of light by focused laser beams," Phys. Rev. 145, 338-379 (1966).

[90] G. D. Boyd and D. A. Kleinman, "Parametric interaction of focused Gaussian light beams," J. Appl. Phys. 39, 3596-3639 (1968).

[91] S. Chaitanya Kumar, A. Esteban-Martin, and M. Ebrahim-Zadeh, "Interferometric output coupling of ring optical oscillators," Opt. Lett. 36, 1068-1070 (2011).

[92] M. W. Sigrist, " Mid-infrared laser-spectroscopic sensing of chemical species," J. Adv. Res. 6(3), 529-533 (2015)

[93] V. A. Serebryakov, É. V. Boĭko, N. N. Petrishchev, and A. V. Yan, "Medical applications of mid-IR lasers. Problems and prospects," J. Opt. Technol. 77(1), 6-17 (2010).

[94] M. Ebrahim-Zadeh and K. Vodopyanov, "Mid-infrared coherent sources and applications: introduction," J. Opt. Soc. Am. B 33, MIC1-MIC1 (2016)

[95] S. D. Jackson, "Towards high-power mid-infrared emission from a fibre laser," Nat. Photonics 6, 423-431 (2012)

[96] Y. Yao, A. J. Hoffman, and C. Gmachl, "Mid-infrared quantum cascade lasers," Nat. Photonics 6, 432-439 (2012).

[97] R. Bhatt, I. Bhaumik , S. Ganesamoorthy , R. Bright , M. Soharab , A. K. Karnal , and P. K. Gupta, " Control of intrinsic defects in lithium niobate single crystals for optoelectronic applications," Crystals. 7, 23 (2017).

[98] V. Petrov, "Parametric down-conversion devices: The coverage of the mid-infrared spectral range by solid-state laser sources," Opt. Mater. 34, 536-554 (2012).

[99] P. G. Schunemann, K. T. Zawilski, L. A. Pomeranz, D. J. Creeden, and P. A. Budni, "Advances in nonlinear optical crystals for mid-infrared coherent sources," J. Opt. Soc. Am. B. 33, D36-D43 (2016).

[100] P. G. Schunemann, L. A. Pomeranz, and D. J. Magarrell, "First OPO based on orientation-patterned gallium phosphide (OP-GaP)," CLEO: Science and Innovations, paper SW3O-1 (2015)

[101] H. Ye, S. Chaitanya Kumar, J. Wei, P. G. Schunemann, M. Ebrahim-Zadeh, "Optical parametric generation in orientation-patterned gallium phosphide," Opt. Lett. 42, 3694-3697 (2017).

[102] J. C. Casals, S. Parsa, S. Chaitanya Kumar, K. Devi, P. G. Schunemann, and M. Ebrahim-Zadeh, "Picosecond difference-frequency-generation in orientation-patterned gallium phosphide," Opt. Exp. 25, 19595-19602 (2017)

[103] G. Insero, C. Clivati, D. D'Ambrosio, P. De Natale, G. Santambrogio, P. G. Schunemann, J. J. Zondy, and S. Borri, "Difference frequency generation in the mid-infrared with orientation-patterned gallium phosphide crystals," Opt. Lett. 41, 5114-5117 (2016)

[104] M. R. Lorenz, G. D. Pettit, and R. C. Taylor, "Band gap of gallium phosphide from 0 to 900°K and light emission from diodes at high temperatures," Phys. Rev. 171, 876-881 (1968).

[105] A. L. Bajor "Investigation of stress-induced birefringence in large semiconductor wafers by imaging polarimetry," Proc. of SPIE 2265, 431-442 (1994).

[106] Y. Li, F. Liu, Y. Li, L. Chai, Q. Xing, M. Hu and C. Wang, "Experimental study on GaP surface damage threshold induced by a high repetition rate femtosecond laser," Appl. Opt. 50, 1958-1962 (2011).

[107] D. D. Arslanov, M. Spunei, A. K. Y. Ngai, S. M. Cristescu, I. D. Lindsay, S. T. Persijn, K. J. Boller, and F. J. M. Harren, "Continuous-wave optical parametric oscillator based infrared spectroscopy for sensitive molecular gas sensing," Laser & Photon. Rev. 7, 188-206 (2013).

[108] J. Courtois, R. Bouchendira, M. Cadoret, I. Ricciardi, S. Mosca, M. De Rosa, P. De Natale, and J. J. Zondy "High-speed multi-THz-range mode-hop-free tunable mid-IR laser spectrometer," Opt. Lett. 38, 1972-1974 (2013).

[109] G. W. Baxter, M. A. Payne, B. D. W. Austin, C. A. Halloway, J. G. Haub, Y. He, A. P. Milce, J. F. Nibler, B. J. Orr, "Spectroscopic diagnostics of chemical processes: applications of tunable optical parametric oscillators," Appl. Phys. B: Lasers Opt. 71, 651 (2000).

[110] A. Fix and R. Wallenstein, "Spectral properties of pulsed nanosecond optical parametric oscillators: experimental investigation and numerical analysis," J. Opt. Soc. Am. B 13, 2484-2497 (1996)

[111] S. J. Brosnan and R. L. Byer, "Optical Parametric Oscillator Threshold and Linewidth Studies," IEEE.J. Quantum Electron. QE. 15, 415-431 (1979)

[112] W. D. Kulatilaka, T. N. Anderson, T. L. Bougher, and R. P. Lucht, "Development of injection-seeded, pulsed optical parametric generator/oscillator systems for high-resolution spectroscopy," Appl. Phys. B: Lasers Opt. 80, 669-680 (2005).

[113] M. J. T. Milton, T. D. Gardiner, G. Chourdakis, and P. T. Woods, "Injection seeding of an infrared optical parametric oscillator with a tunable diode laser," Opt. Lett. 19, 281-283 (1994).

[114] J. E. Bjorkholm and H. G. Danielmeyer, "Frequency control of a pulsed optical parametric oscillator by radiation injection," Appl. Phys. Lett. 15, 171-173 (1969).

[115] B. J. Orr, M. J. Johnson, and J. G. Haub, "Spectroscopic applications of pulsed tunable optical parametric oscillators," Tunable Laser Applications, Chapter 2, 11-82 (1995).

[116] G. W. Baxter, M. A. Payne, B. D. W. Austin, C. A. Halloway, J. G. Haub, Y. He, A. P. Milce, J. W. Nibler, and B. J. Orr, "Spectroscopic diagnostics of chemical processes: applications of optical parametric oscillators," Appl. Phys. B: Lasers Opt. 71, 651-663 (2000).

[117] G. W. Baxter, H. D. Barth, B. J. Orr, "Laser spectroscopy with a pulsed, narrowband infrared optical parametric oscillator system: a practical, modular approach," Appl. Phys. B: Lasers Opt. 66, 653-657 (1998).

[118] D. J. Armstrong and A. V. Smith, "90% pump depletion and good beam quality in a pulse-injection-seeded nanosecond optical parametric oscillator," Opt. Lett. 31, 380-382 (2006).